



HAL
open science

Multi-Parameters Miniature Sensor for Water Network Management

Ferdous Jahan Shaun

► **To cite this version:**

Ferdous Jahan Shaun. Multi-Parameters Miniature Sensor for Water Network Management. Reactive fluid environment. Université Paris-Est, 2018. English. NNT : 2018PESC1138 . tel-02148245

HAL Id: tel-02148245

<https://theses.hal.science/tel-02148245v1>

Submitted on 5 Jun 2019

HAL is a multi-disciplinary open access archive for the deposit and dissemination of scientific research documents, whether they are published or not. The documents may come from teaching and research institutions in France or abroad, or from public or private research centers.

L'archive ouverte pluridisciplinaire **HAL**, est destinée au dépôt et à la diffusion de documents scientifiques de niveau recherche, publiés ou non, émanant des établissements d'enseignement et de recherche français ou étrangers, des laboratoires publics ou privés.



Ecole Doctorale

Mathématiques, Sciences de l'Information et de la Communication (MSTIC)

THÈSE

pour obtenir le grade de

Docteur de l'Université Paris-Est

Spécialité : Electronique, Optronique et Systèmes

Présentée et soutenue publiquement par

Ferdous Jahan Shaun

Le 07 Novembre 2018

Miniature Multi-parameter Sensor for Water Network Monitoring

Capteur multi-paramétrique miniature pour la gestion des réseaux d'eau

Directeurs de thèse

Tarik Bourouina

Jury

Pascal Nouet, Professeur, LIRMM, Université Montpellier II, Rapporteur

João Pedro Oliveira, Professeur, Université Nova de Lisbonne, Rapporteur

Bérengère Lebental, Directeur de Recherche, LPICM, Ecole Polytechnique, Examineur

Jérémy Drévilion, Maître de Conférences, Université de Poitiers, Examineur

Elyes Nefzaoui, Professeur Assistant, ESYCOM, ESIEE Paris, Co-encadrant

Tarik Bourouina, Professeur, ESYCOM, ESIEE Paris, Directeur de thèse

Acknowledgement

First of all, I would like to express my heartfelt gratitude and reverence to my PhD supervisor Prof. Tarik Bourouina and co-supervisor Prof. Elyes Nefzaoui for giving me the wonderful opportunity to work under their supervision. It was an excellent scope to enrich myself in the horizon of academic research. Their invaluable instructions and constructive suggestions succour to broaden my outlook in academia and thereby moulded a scientific researcher in me. Further, their sincere guidance and abundant help throughout the period of thesis work aided me to reach my ultimate goal.

Besides my supervisors, I would like to thank the distinguished jury members Prof. João Pedro Oliveira and Prof. Pascal Nouet for their valuable and insightful comments on my work. My sincere thanks also go to honourable thesis committee members Dr. Bérengère Lebental and Dr. Jérémie Drévillon.

My boundless thankfulness to Dr. William Cesar for his valuable contribution at the very initial stage of the thesis. His introductory diverse attempt helped me to proceed in the right direction during the whole period of my thesis study. I also would like to mention a few more names of intern students in different periods of my thesis whose important contribution alleviated stress and helped me to handle specified complexity. Thanks to Mr. Massimo Pellegrino, whose offering in conductivity sensor was significantly conducive to develop the initial prototype and Ms. Kruthiga Gopalan for helping me by conducting experiments during my hard time. Especial thanks to Mr. Zhifie Xu for his fruitful simulation work in order to finalize the geometry of the pressure sensor for fabrication.

I would like to thank Prof. Philippe Basset and Prof. Xiaofeng Guo for their assistance and advice from time to time during my thesis. A special thanks to Monsieur Frederic Marty senior research engineer in ESIEE cleanroom, has made a significant contribution to my PhD work. I would not be able to conduct my research work without his punctual support by providing the fabricated device. Thanks to Prof. Patrick Poulichet, Dr. Martine Capo-chichi and Prof. Yamin Leprince for helping me with their valuable suggestions in different phases of my doctoral study.

I want to thank the European Union and the people from the project consortium who were deeply involved in taking the initiative for conducting such a momentous project PROTEUS, whose outcome will significantly contribute to human well-being. I am very optimistic about the impact of PROTEUS and am sure that it will remarkably bestow a fruitful service in the respective field. I am lucky to become a part of such a wonderful project.

Special thanks to my all colleagues for their kind support during my stay here. I was fortunate enough to have some supportive people around me. Their counsel and motivation helped me to move forward.

Especially, Yuval, Ali, Imad, Mazen, Yingxian, Sreyash, Lan, Hemin, Hatem, Amin and Amar; who were there for me in every step of the way. In fact, I am indebted to numerous people and though I have not mentioned their names, they have had a significant hand during the entire duration of my doctoral study.

Last but not least in any way, I would like to thank my parents and my wife. The selfless sacrifices and unbound love that my parents have showered upon me help to reach this stage. I would like to express my ineluctable appreciation to my wife, with my utmost affection for her absolute support and encouragement.

Abstract

Water is a vital element for every living being on the earth. Like many other dwindling natural resources, clean water faces a strong pressure because of human activity and the rapid growth of global population. The situation is so critical that clean water has been identified as one of the seventeenth sustainable development goals of the United Nations. Under these conditions, a sustainable management of water resources is necessary. For this purpose, a smart solution for water networks monitoring can be very helpful. However, commercially available solutions lack compactness, self-powering capabilities cost competitiveness, necessary to enable the large rollout over water networks.

The present thesis takes place in the framework of a European research project, PROTEUS, which addresses these different problems by designing and fabricating a multi-parameter sensor chip (MPSC) for water resources monitoring. The MPSC enables the measurement of 9 physical and chemical parameters, is reconfigurable and self-powered. The present thesis addresses more precisely physical sensors, their design, optimization and co-integration on the MPSC. The developed device exhibits state of the art or larger performances with regard to its redundancy, turn-down ratio and power consumption.

The present manuscript is split into two main parts: Part-I and Part-II. Part-I deals with non-thermal aspects of the MPSC, the pressure and conductivity sensor for instance, as well as the fabrication process of the whole device (Chapter 1 and 2). The background of environmental monitoring is presented in Chapter 1 along with the State of Art review. Chapter 2 describes fabrication methods of the MPSC. Preliminary characterization results of non-thermal sensors are also reported in this chapter. Chapter 3 and 4, included in Part-II, deal with thermal sensors (temperature and flow-rate). Chapter 3 describes the many possible uses of electric resistances for sensing applications. Finally, in chapter four, we focus on flowrate sensors before concluding and making a few suggestions for future works.

Résumé

L'eau est une ressource vitale, indispensable à la vie sur terre. A l'instar de nombreuses autres ressources naturelles, l'eau propre à la consommation est soumise à une forte pression à cause de l'impact de l'activité humaine d'une part et de l'augmentation continue de la population mondiale d'autre part. Une pression tellement forte que l'eau propre représente l'un des 17 objectifs de développement durable des Nations Unies. Dans ce contexte, une gestion rationnelle et durable de la ressource s'avère indispensable. Dans ce but, un système intelligent de supervision des réseaux d'eau potable peut s'avérer très utile. Les systèmes existants sont toutefois peu intégrés et compacts, nécessitent souvent une alimentation externe, et restent relativement chers pour un déploiement massif sur les réseaux.

La présente thèse s'inscrit dans le cadre d'un projet de recherche européen, PROTEUS, visant à pallier ces différents problèmes en mettant au point un système de mesure pour la supervision de la ressource en eau permettant la mesure de 9 paramètres physico-chimiques, reconfigurable, et énergétiquement autonome. La contribution de la présente thèse à ce projet porte sur la conception et l'optimisation des différents capteurs physiques (conductivité électrique, pression, température et débit) ainsi qu'à leur co-intégration sur une même puce. Le système proposé montre des performances au moins égales à celle de l'état de l'art en ce qui concerne la robustesse, assurée par la redondance de nombreux éléments sensibles, le domaine de sensibilité et la consommation énergétique.

Le présent manuscrit est par conséquent construit comme suit : le premier chapitre est une introduction générale à la supervision de grandeurs environnementales et à la puce multi-capteurs. Le second chapitre décrit la structure de la puce multi-capteurs ainsi que les méthodes de fabrication utilisées, avec une attention particulière accordée aux capteurs de pression et de conductivité électrique. Le troisième chapitre porte sur l'utilisation de résistances électriques pour la mesure de diverses grandeurs physiques, notamment la température. Le dernier chapitre s'attarde plus particulièrement sur l'utilisation de ce type de résistances pour la mesure de débit avant de conclure et de proposer des perspectives pour des travaux futurs.

Table of Contents

| | | |
|----|---|----|
| I. | Introduction | 1 |
| | The need for environment monitoring..... | 1 |
| | Motivation | 1 |
| | Outline of the thesis..... | 4 |
| 1 | Chapter 1: Background on environmental monitoring (Air & Water) and related measurement tools.. | 9 |
| | 1.1 Fundamental natural resources for life and the necessity for environmental monitoring | 9 |
| | 1.2 Air Quality Monitoring | 9 |
| | 1.3 Water Quality Monitoring..... | 13 |
| | 1.3.1 Analytical Chemistry for multi-parameter sensing of chemical pollutants of water | 14 |
| | 1.3.2 Multi-parameter sensing probes for water network monitoring | 15 |
| | 1.3.3 Particulate and microbiological pollutants..... | 16 |
| 2 | Chapter 2: Co-integration of Multi-Parameter Sensor Chip (MPSC) for Water Network Monitoring. | 19 |
| | 2.1 Introduction..... | 19 |
| | 2.2 Choice of Resistive Readout | 19 |
| | 2.3 Fabrication | 20 |
| | 2.3.1 Metal on Glass and co-integration challenge | 20 |
| | 2.3.2 Metal on a silicon substrate and first full co-integration of the whole sensors..... | 22 |
| | 2.3.3 Silicon substrate with front-side etching: attenuation of the negative effect of the high thermal conductivity of the silicon substrate | 25 |
| | 2.3.4 Flow-rate sensor on a silicon substrate with suspended heater..... | 26 |
| | 2.4 Packaging of the MPSC into a Printed Circuit Board (PCB)..... | 27 |
| | 2.5 First Phase of the Characterization: Non-Thermal Aspects | 28 |
| | 2.6 Pressure sensor design and characterization | 28 |
| | 2.6.1 Experimental setup | 30 |
| | 2.6.2 Results and Discussion | 32 |
| | 2.7 Conductivity sensor design and characterization..... | 33 |

| | | |
|-------|--|----|
| 2.7.1 | Conductivity..... | 33 |
| 2.7.2 | Introduction of the conductivity sensor and its working principle | 35 |
| 2.7.3 | Experimental setup | 39 |
| 2.7.4 | Results and Discussion | 40 |
| 2.7.5 | Evaluation of Antifouling Properties of Al ₂ O ₃ / TiO ₂ ALD-coatings..... | 45 |
| 2.8 | Conclusion | 49 |
| 3 | Chapter 3: Electrical resistance as a key building block for measurement of temperature and related water parameters..... | 51 |
| 3.1 | Introduction..... | 51 |
| 3.2 | Water temperature variations and its impacts | 52 |
| 3.2.1 | Natural and anthropogenic factors impacting water temperature | 52 |
| 3.2.2 | The impact of water temperature on other parameters governing water quality | 53 |
| 3.3 | Fundamentals on temperature and its measurement | 55 |
| 3.3.1 | Basics on temperature | 55 |
| 3.3.2 | Brief history of temperature measurement..... | 56 |
| 3.3.3 | Electrical Resistance Devices | 57 |
| 3.3.4 | Resistance Temperature Device (RTD) | 60 |
| 3.4 | RTD-based Temperature Sensor..... | 61 |
| 3.4.1 | Design of the temperature sensor..... | 62 |
| 3.4.2 | Characterization | 64 |
| 3.4.3 | Joule Self-Heating..... | 66 |
| 3.5 | Evaluation of fabrication process uniformity in terms of resistance variations and TCR at wafer-level..... | 69 |
| 3.6 | The electrical resistance as a temperature sensor and multi-purpose building block for sensors based on Heat transfer..... | 73 |
| 3.6.1 | Application of RTD as Flow-rate sensor | 73 |
| 3.6.2 | Application of RTD as Thermal Conductivity Detector (TCD) | 74 |
| 3.7 | RTD Transient Behavior..... | 74 |

| | | |
|-------|--|-----|
| 3.7.1 | Simulation of RTD transient behavior..... | 75 |
| 3.7.2 | Experimental measurement of RTD transient response..... | 79 |
| 3.8 | Conclusion | 81 |
| 4 | Chapter 4: Flow-Rate Sensor Co-integration | 83 |
| 4.1 | Background and State of Art..... | 83 |
| 4.1.1 | Flow-rate measurement..... | 83 |
| 4.1.2 | Commercial flow-rate sensors | 84 |
| 4.1.3 | Micro flow-rate sensors | 86 |
| 4.1.4 | Thermal Flow-rate sensors..... | 91 |
| (i) | Anemometric operation principle | 92 |
| (ii) | Calorimetric operation principle..... | 94 |
| (iii) | Time-of-flight (TOF) operation principle..... | 95 |
| 4.2 | Materials and Methods..... | 96 |
| 4.2.1 | Design summary of thermal Flow-rate sensors with co-integration constraints..... | 97 |
| 4.2.2 | Numerical simulation method..... | 98 |
| 4.2.3 | Experimental Setup for calibration of the Flow-Rate Micro-sensors | 99 |
| 4.3 | Numerical Results and Discussion..... | 103 |
| 4.3.1 | Glass substrate based flow-rate sensor | 103 |
| 4.3.2 | Silicon substrate based flow-rate sensor | 107 |
| 4.3.3 | Silicon membrane based flow-rate sensor | 110 |
| 4.3.4 | Pillar structure flow-rate sensor | 112 |
| 4.3.5 | Reverse Flow | 117 |
| 4.3.6 | Numerical results comparison..... | 122 |
| 4.4 | Experimental Results | 123 |
| 4.4.1 | Joule self-heating and Power consumption..... | 123 |
| 4.4.2 | Sensor's response to the velocity | 125 |
| 4.4.3 | Comparison between numerical and experimental results..... | 126 |

| | |
|---|-----|
| 4.5 Conclusion | 127 |
| 5 Conclusion and Prospects..... | 129 |
| 5.1 General conclusion..... | 129 |
| 5.2 Perspectives of future developments of the MPSC..... | 130 |
| 1 Appendix for Chapter 2..... | 133 |
| 1.1 Annex 1- Pressure sensor behavioral simulation | 133 |
| 1.2 Annex 2- Conductivity Sensor- Part A: Electrical Modelling | 134 |
| 1.2.1 The electronic model of the sensor for numerical analysis..... | 134 |
| 1.2.2 Frequency response..... | 135 |
| 1.3 Annex 3- Conductivity sensor- Part B: details of the experimental setup | 136 |
| 1.3.1 Data acquisition | 136 |
| 1.3.2 Tools used for Anti-fouling test:..... | 137 |
| References | 139 |
| List of publications | 149 |

List of Figures

| | |
|---|----|
| Figure i-1: Schematic representation of water distribution monitoring network | 2 |
| Figure i-2: PROTEUS multi-parameter sensor chip for water network monitoring- (a) sensor chip co-integrated 4 MEMS physical sensors along with 5 chemical sensors, (b) capsule board with the sensor and CMOS chip with electronics and (c) sensor head. | 3 |
| Figure 1-1: WSNS based IAQ monitoring device | 11 |
| Figure 1-2: The Mobile sensor node | 12 |
| Figure 1-3: Experimental design of Multi-sensor module for indoor climate monitoring..... | 12 |
| Figure 1-4: s::can multi-parameter water quality monitoring device based on UV-VIS spectroscopy | 15 |
| Figure 1-5: Commercially available multi-parameter sensing probes from- (a) Intellitect, (b) Six Sense and (C) Endetec. | 16 |
| Figure 1-6: Laser-based water particle monitoring system BioSentry ²⁷ | 17 |
| Figure 1-7: Detection Micro-biological water contamination alert systems, based on optofluidic technologies. (a) Parasitometer from Water Optics Technologies and (b) E-Alert system from FLUIDION | 17 |
| Figure 2-1: (a) Cross-section view of the multi-parameter sensor chip based on a glass substrate and (b) fabricated multi-parameter sensor chip on a glass substrate | 21 |
| Figure 2-2: Different fabrication phases of the silicon-based MPSC. (a) Front side patterning of the device-pressure sensor fabrication together with the other sensors, (b) hard mask patterning on the back side and back-side DRIE for creating the membrane, (c) removal of the hard mask for silicon-glass anodic bonding and (d) micrograph of a co-integrated multiple sensing elements on silicon at the chip scale, after wafer dicing. | 23 |
| Figure 2-3: Cross-section view of the membrane-based flow-rate sensor | 24 |
| Figure 2-4: Fabrication sequences of the pillar structure flow-rate sensor. (a) Patterning of the front-side cavity and etching of the front side deposited layers, (b) front-side DRIE, (c) SEM photo of the resulting pillar flow-rate sensor | 25 |
| Figure 2-5: 2D cross-section view of the bridge structure flow-rate sensor | 26 |
| Figure 2-6: The PCB for connecting the sensors with an electronic circuit. (a) The whole PCB labelled with dimensions, (b) the zoomed image of the chip containing part, where the connection pads are wire bonded | |

(dotted orange circle) to the PCB and protected hermetically with glue against the water. The other part of the chip is not connected to the PCB. 28

Figure 2-7: Typical layout of the MEMS pressure sensor. Different versions were considered in order to investigate the sensitivity with respect to the pressure. 30

Figure 2-8: Experimental setup of the pressure sensor. (a) The sensor is inserted into the glass bottle and the surroundings of the insertion whole glued in order to make it leakage proof. A transparent plastic pipe is used to transmit the hydrostatic air pressure from the Fluigent SA to the glass bottle. (b) A schematic diagram which replicates the experimental setup of the pressure sensor..... 31

Figure 2-9: Schematic diagram of the data reading circuit. Here, the Wheatstone bridge consists of four resistors R_1 , R_2 , R_3 and R_4 represent the four piezoresistors of the pressure sensor. 31

Figure 2-10: Measured responses of the (a) rectangular and (b) square shaped membrane pressure sensor. Excellent linearity is observed in both the cases with a coefficient of determination 0.998. 32

Figure 2-11: Schematic illustration of ions migration in a solution due to the electricity 36

Figure 2-12: Current and voltage electrodes of the conductivity sensor..... 36

Figure 2-13: Different versions of the conductivity sensor 37

Figure 2-14: Different parts of the conductivity sensor electrodes labelled with nomenclature 38

Figure 2-15: Conductivity sensor experimental setup. The sensor is submerged under a solution. There are five beakers with different conductivity solutions. The input-output of the sensor is connected to the NI DAQ board for supplying the power and reading the measured data. 39

Figure 2-16: Responses of the three sensors in frequency sweep analysis (a) sensor 1, (b) sensor 2 and (c) sensor 3 under the frequency range $\sim 500 \mu\text{S}/\text{cm}$ to $\sim 2500 \mu\text{S}/\text{cm}$ 41

Figure 2-17: The response of the S1, S2 and S3 sensors under the considered five conductivity solutions at 5 kHz, 10 kHz and 15 kHz supply frequencies. Error bars are added in the plots, but not visible due to the small uncertainties. 42

Figure 2-18: Conductivity sensor response at 5 kHz with and without coating layer made of Al_2O_3 43

Figure 2-19: (a) The measured response of the S2 sensor with TiO_2 ALD layer at 5 kHz, 10 kHz and 15 kHz and (b) comparison among the measured response of the same sensor with TiO_2 , Al_2O_3 ALD layer and without ALD layer. 44

Figure 2-20: (a) Two prepared PVC tubes for the test where the sensor chips are mounted on their head, after oven dried at 65°C , each tube contains four chip denoted by A, B, C and D. No ALD coating on-chip

A, chip B is coated by Al_2O_3 with 10 nm thickness and chip C and D are coated by TiO_2 with 10 and 30 nm layer thicknesses respectively. (b) The prepared prototype for the field test..... 46

Figure 3-1: Main water quality parameters that are affected by the water temperature (TDS: Total Dissolved Solids, ORP: Oxidation Reduction Potential)..... 53

Figure 3-2: (a) Mask Layout of the temperature sensor; 1, 2, 3 and 4 represent the connection wires where 1 and 4 are used for power supply and 2 and 3 to read data, (b) physical dimensions of sensing resistor of the temperature sensor and (c) real temperature sensor. 62

Figure 3-3: Experimental setup for the temperature sensor Calibration. 64

Figure 3-4: Temperature sensor response at different water temperature under 0.5 mA current supply.... 65

Figure 3-5: Illustration of Joule self-heating phenomenon. Depending on the current magnitude injected into a resistor, the local temperature is more or less affected, leading to 2 regimes: (i) low current, typically for operation of the resistor temperature sensor..... 66

Figure 3-6: Theoretical Joule self-heating on the same resistor as the one considered for the experimental result shown in Fig. 3-5. Both first order model (equation 3-11) and second order model (equation 3-16) have been used. 69

Figure 3-7: Wafer-level mapping of resistance values recorded for temperature sensors and flow-rate sensors recorded at 3 temperatures: 20°C, 60°C and 100°C..... 71

Figure 3-8: Wafer-level mapping of the values of TCRs (Temperature-Coefficient of Resistance) of temperature sensors and flow-rate sensors derived from the data presented in Table 1..... 72

Figure 3-9: Wafer-level mapping of Resistance values recorded at 20°C and 100°C for pressure sensors 72

Figure 3-10: Wafer-level mapping of TCR values (Temperature-Coefficient of Resistance) for pressure sensors..... 73

Figure 3-11: Sketch of 3 different models accounting for heat exchange phenomena on a heated resistor. (a) heat transfer only within the resistor’s material, (b) additional heat exchanges with the substrate material and surrounding fluid medium and (c) heat transfer through convection due to the fluid velocity. 77

Figure 3-12: Numerical simulations of the transient temperature response, considering different substrate materials (Silicon versus Glass) and surrounding fluid media (Air versus Water)..... 78

Figure 3-13: Numerical simulations of the transient temperature response of a heated resistor, considering the effect of velocity (in this case substrate material is Glass and surrounding fluid is Air)..... 79

| | |
|---|-----|
| Figure 3-14: Experimental measurement of the transient temperature response of 3 different resistor designs based on silicon substrate, operated under 3 different water velocities. | 80 |
| Figure 4-1: Flowmeters manufactured by OMEGA company..... | 85 |
| Figure 4-2: Different Ultrasonic Flowmeters of LONGRUN company | 86 |
| Figure 4-3: Fluigent flow-rate platform, (a) adjustable pressure generator (b) flow units connected to the flow board..... | 87 |
| Figure 4-4: Cross-section view of a micro-machined flow-rate sensor ¹⁰⁹ | 87 |
| Figure 4-5: A microchannel flow-rate sensor, where the channel is fabricated on (a) the substrate and (b) in suspended configuration ¹¹⁰ | 88 |
| Figure 4-6: Fabricated flow-rate sensor (a) microchannel fabricated on the substrate and (b) a suspended microchannel ¹¹⁰ | 88 |
| Figure 4-7: Schematic representation of single hair cell biomimetic flow-rate sensor ¹¹¹ | 89 |
| Figure 4-8: Schematic illustration of Hot-wire anemometer flow-rate sensor ⁸² | 93 |
| Figure 4-9: Schematic representation of calorimetric operation mode of a thermal flow-rate sensor ⁸² | 94 |
| Figure 4-10: Schematic representation of Time-of-Flight operation principle of a thermal flow-rate sensor ⁸² | 95 |
| Figure 4-11: The 4 different configurations of the flow-rate sensor- (a) glass substrate, (b) bulk silicon, (c) silicon membrane and (d) pillar structure | 97 |
| Figure 4-12: (a) Schematic diagram and (b) labelled picture of the experimental setup. | 100 |
| Figure 4-13: Schematic of the constant current circuit source..... | 102 |
| Figure 4-14: Geometry of (a) the whole simulation domain, (b) the sensor chip and (c) the platinum sensing element on top of a glass substrate..... | 104 |
| Figure 4-15: The picture of (a) velocity profile and (b) temperature profile of the glass-based flow-rate sensor exported from COMSOL | 106 |
| Figure 4-16: Normalized temperature of the glass based sensor versus fluid velocity..... | 107 |
| Figure 4-17: (a) Geometry of silicon substrate flow-rate sensor, and a (b) zoom picture of the platinum resistor and SiO ₂ insulation layer..... | 108 |
| Figure 4-18: Temperature profile of the silicon based flow-rate sensor at $v = 0$ m/s. | 109 |

| | |
|---|-----|
| Figure 4-19: Silicon substrate flow-rate sensor's response versus the water velocity. | 109 |
| Figure 4-20: Membrane structure flow-rate sensor..... | 110 |
| Figure 4-21: Temperature field around the membrane flow-rate sensor for a fluid velocity of 0.001 m/s. | 111 |
| Figure 4-22: Membrane-based flow-rate sensor response with respect to the velocity | 111 |
| Figure 4-23: The pillar based flow-rate sensor geometric configuration..... | 112 |
| Figure 4-24: The temperature field of the pillar flow-rate sensor at 10 mW power supply at a velocity of 0.04 m/s. In this case, the cavity dimension is 150 x 100 μm and the resistor width is 5 μm | 113 |
| Figure 4-25: Pillar structure flow-rate sensor response with respect to the velocity | 114 |
| Figure 4-26: The pillar device sensitivity to the velocity at different resistor width | 115 |
| Figure 4-27: Pillar structure flow-rate sensor response as a function of fluid velocity for different cavity depths. Numbers between parentheses in the legend indicate the pillar height (equal to the cavity depth) and width then the cavity width, respectively..... | 116 |
| Figure 4-28: Pillar flow-rate sensor response as a function of velocity for different cavity depths. | 116 |
| Figure 4-29: (a) Normal velocity profile for different fluid velocities, (b) reverse flow at the resistor vicinity causing the anomalous thermal behaviour within the velocity range highlighted by black circles in Figure 4-16 and Figure 4-25, (c) normal temperature profile and (d) the effect of reverse flow on the sensor temperature profile (flow direction is from left to right). | 118 |
| Figure 4-30: (a) The schematic diagram of the sensor node with dimensions and (b) photo of the real sensor node embedding the MPSC. | 119 |
| Figure 4-31: (a) The picture of the round-edged sensor node tilted at 15° with respect to the normal and inserted into a water pipe, (b) the sensor node head chamfered with a 0.5 mm radius and (c) 1 mm radius. | 119 |
| Figure 4-32: Illustration of the sensor node head and the region that was considered for extracting the velocity field in X-coordinate. Parallel red lines (2-D cut line) represent the extent of the region and they have uniform distance (0.5 mm) between them. | 120 |
| Figure 4-33: Velocity field distribution along X-axis direction (for an inlet velocity of 0.1 m/s) around the sensor node at different distances, (a) initial sensor node and (b) modified sensor node with round edged and the chamfered notch of the sensor chip location with 1 mm radius. | 121 |

Figure 4-34: Simulation results of glass, pillar, membrane and bulk silicon flow-rate sensor response to the main flow velocity. 122

Figure 4-35: (a) Joule self-heating temperature of the heating resistors at different supply current in non-flowing fluid, and (b) power consumption of the four corresponding sensors. 124

Figure 4-36: Glass, pillar, silicon membrane and bulk silicon flow-rate sensor measured response as a function of velocity at 30 mA current supply. 126

Figure 4-37: Numerically calculated response of the pillar and glass devices in the velocity range from 0 m/s to 1 m/s. 127

I. Introduction

The need for environment monitoring

With the growth of the global industrialization and the population, the environment on earth is being dilapidated day by day. The main natural resources, namely air, water and soil are increasingly polluted by human activities either deliberately or accidentally. As a consequence, living organisms are mortally affected leading to less biodiversity, climate change as well as numerous severe health concerns. Pollution in its various forms and climate change are now becoming a global concern which led the United Nations, among other international organizations, to establish a policy of *Sustainable Development* called *#Envision2030*, which translates into *17 Goals to transform our world*¹. A healthy environment relies on the limpidity of its basic elements. There are numerous research activities going on to this horizon to maintain the natural ecological balance for improving the present condition and future unexpected environmental antagonism. All the elements of the environment are reciprocally kindred and unitedly they form an organic complex. If one of the elements is changed or contaminated within this chain, the whole system decisively faces a rough change which brings an imbalance in the usual ecological condition. For example, the purity of the soil is interconnected with the groundwater purity and in some perspective; it affects the air quality as well. Hence, excessive use of chemical fertilizer and insects killer (pesticides, herbicides) for cultivation or the presence of heavy metals and arsenic in the soil damages the natural characteristics of the soil^{1,2} and it is also liable for the water pollution as well. The detrimental chemical substances get mixed with the natural sources' water due to the rain and the close contact of subterranean water with the soil which is admixed with harmful metal cause water pollution. As a consequence, in order to protect the environment and enable actions to be taken, there is a need to monitor through measurements all it's the basic elements from the accidental and deliberate pollution. This kind of measurement of a diverse number of parameters over very large domains requires the development of new tools capable of *ubiquitous sensing*. In other words, there is a need to measure almost everything almost everywhere.

Motivation

In the context of monitoring natural resources and related need of developing new measurement tools, the focus of this thesis is on water. The need is to develop ubiquitous sensors towards their wide-scale deployment for the measurement of a wide variety of parameters. It is obvious that wide-scale deployment will require low-cost solutions and hence, the use of miniaturization seems unavoidable. A vast majority of the commercially available devices for measurement in water are not miniaturized and their functionality

¹ <https://www.un.org/development/desa/disabilities/envision2030.html>

does not cover both the physical and chemical aspects of the water. A few exceptions were reported of multi-parameter sensors based on the heterogeneous assembly of several micro-sensors, but those solutions lead to high costs in the order of 10.000 € unit price, which makes it not compatible with large deployment through water networks.

In order to respond to this need, the H2020 European project PROTEUS is aimed at to produce a monolithic multi-parameter sensing module which can measure 4 physical and 5 chemical parameters of the water. This project is funded by European Commission under H2020 programme for research. The goal of this project is to deliver a smart water monitoring system which is enabled to perform real-time analysis along with wireless data transmission option. In addition, this is a self-powered device; an energy harvester is joined with the sensor node which can generate power from the water flow. The proposed device is 10 times smaller and cost-effective to compare with the state of the art. A schematic diagram of the proposed water distribution monitoring network using PROTEUS multi-parameter sensor chip is presented in Figure I-1, where all the other associated equipment is also sketched. This system includes the wastewater and rainwater under the same monitoring network as well.

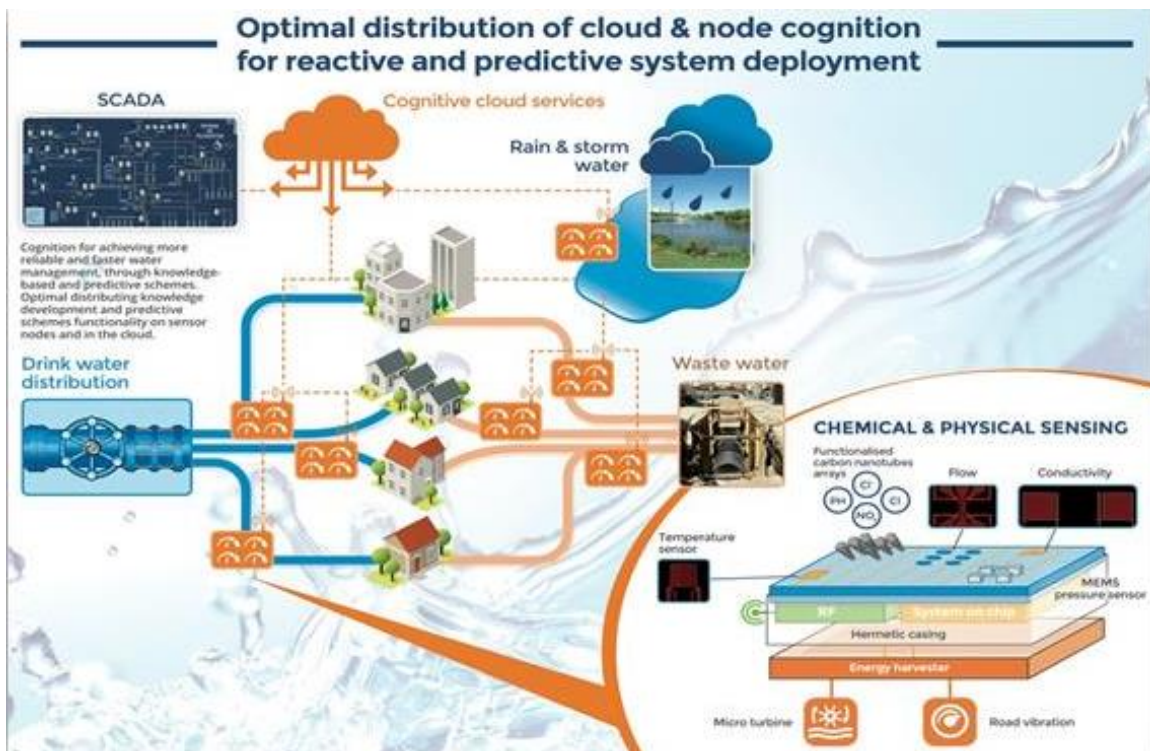


Figure I-1: Schematic representation of water distribution monitoring network

The multi-parameter sensor chip (MPSC) is demonstrated in Figure I-2. Figure I-2(a) shows the multi-sensor chip which contains all the MEMS physical and chemical sensors. The prototype model (Figure I-2(b)) contains the silicon-based multi-parameter sensing chip –developed in the frame of this thesis- on a PCB along with the CMOS chip developed by UNINOVA, a partner in this project from University of Lisbon, Portugal. The black substance at the two edges of the sensor chip and around the CMOS chip is protective glue, which protects the electrical connection between the chips and the PCB. Figure I-2(c) reports the sensor node that will be implemented in the water distribution network for measuring the parameters. All the subsidiary electronics are adjoined inside this sensor node, also developed by UNINOVA.

In total, there are 9 different sensing elements to determine several physical and chemical parameters of the water. Among them, only the four physical MEMS sensors are reported here in this thesis study, while the chemical sensors required post-processing of the chip using ink-jet printing of functionalized carbon nanotubes, which has been developed by IFSTTAR in the frame of their joint team with LPICM Laboratory (CNRS-Ecole Polytechnique). These four sensors can measure the conductivity, pressure, flow-rate and temperature of the water. Different versions of the MPSC have been fabricated in order to study different phenomena *i.e.*, the impact of the substrate material on the sensors' performance, power consumption, the thermal efficiency of the thermo-resistive sensor.

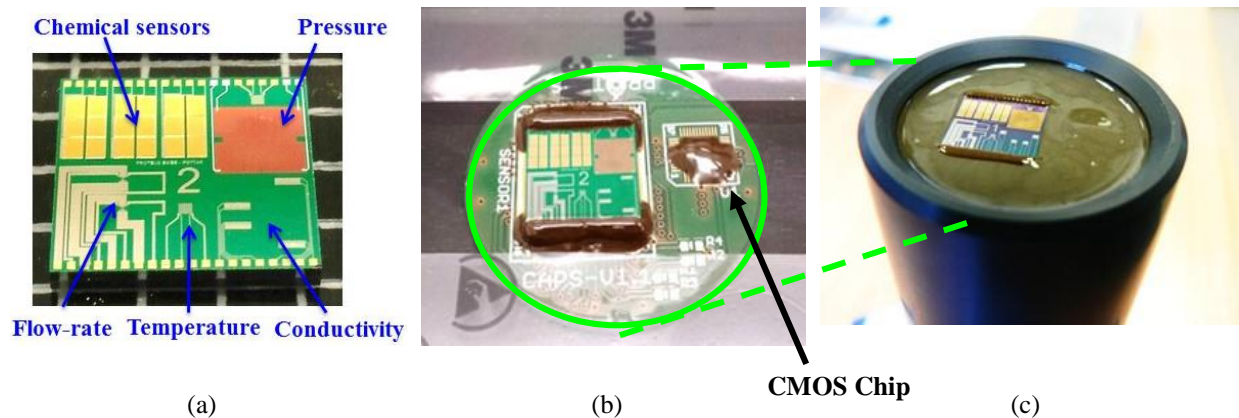


Figure I-2: PROTEUS multi-parameter sensor chip for water network monitoring- (a) sensor chip co-integrated 4 MEMS physical sensors along with 5 chemical sensors, (b) capsule board with the sensor and CMOS chip with electronics and (c) sensor head.

Although, all the sensors are based on resistive read-out but they are distinct in terms of their working principle, physical structure. Therefore, each of the sensors has independent specifications in order to ensure

their functionality at the desired level. For instance, the conductivity sensor measures the electrical conductivity of the water and it works with an AC current supply. It's a four-probe conductivity sensor, whose sensitivity depends strongly on the shape of the electrodes and the supply current frequency. The fundamental principles are somehow similar for the flow-rate and the temperature sensor. Both of them are a similar form of thin-film platinum RTD with the typical working principle, where the functionality of these two sensors relies on the heat transfer. As a consequence, low thermal conductive substrate and proper thermal insulation are required for the effectiveness of those sensors. On the other hand, the pressure sensing element of the MPSC is a piezo-resistive pressure sensor. The essential part of this pressure sensor is a membrane where four piezo-resistors placed at the edges of this membrane. Hence, this sensor requires a material compatible with membrane micro-fabrication. The usual material is silicon that is the most suitable for this purpose when dealing with MEMS technologies. The membrane of the considered pressure sensor is made by single crystal silicon while the piezo-resistors are made from a polysilicon thin film. Therefore, silicon is mandatory in order to create the pressure sensor. So, it is obvious that co-integration of all the above-mentioned sensors on the same chip will face some constraints in different perspectives. The challenge regarding the co-integration process and how it was overcome will be explained in Chapter 2 along with the MPSC fabrication details.

Outline of the thesis

This thesis is organized into 4 main chapters and is split into two Parts. Part I (Chapter 1 and Chapter 2) deals with the Multi-Parameter Sensing Chip (MPSC) for Water Network Monitoring. We will elaborate on how we managed most of the co-integration constraints in order to eventually come out with the realization of a monolithic MPSC, embedding four different physical sensors and ready to host additional chemical sensors through further post-processing of this chip. We will also present in this Part I, the results obtained on two sensors among the four sensors; the pressure sensor and the conductivity sensor.

The two other sensors will be described in much more detail in Part II (Chapter 3 and Chapter 4), which is fully dedicated to sensors involving thermal effects: temperature sensor and flow-rate sensors. In this part, we will discuss how proper and innovative designs allowed us to achieve full co-integration of a flow-rate sensor, despite the constraint of operation with a silicon substrate, which is not favourable in terms of thermal conductivity.

In Chapter 1, the general background of environmental monitoring and its necessity is highlighted. The monitoring importance of the two most crucial environment elements air and water are discussed elaborately. Some of the existing devices that have been used to monitor these elements are also presented.

An introductory discussion regarding the multi-parameter sensor chip which has been developed under the frame of this thesis work presented here in this chapter as well.

Chapter 2 deals with the co-integration effort that was required to achieve a Multi-Parameter Sensing Chip (MPSC) for Water Network Monitoring. The design strategy and fabrication steps from the very initial version to the final prototype are discussed in a consecutive manner. The first prototype of the multi-sensing device was based on a glass substrate and in the subsequent versions; silicon was used as a substrate material in order to enable the co-integration. Hence, the co-integration of different sensors on the same chip and the appeared challenge regarding the co-integration step also stated in Chapter 2. The conductivity and pressure sensor are included in this chapter as well. Their physical structure and fundamental working principles stated along with the experimental data. Particularly, the pressure sensor introduces the constraint regarding the co-integration process in the perspective of the substrate material. Common substrate material that allows the co-integration causes performance degradation of thermal sensing element like a flow-rate sensor of the MPSC. The detailed strategy of the successful co-integration is presented in this chapter. Experimental results are also given for the assessment of the first sensor's performance and dispersion of their characteristics.

Chapter 3 gives an elaborate discussion on thermometry and multi-functionality of a resistor. It illustrates the different methods of thermometry and its history. The major three methods of the temperature measurement: *invasive*, *semi-invasive* and *non-invasive* and their sub-categories are briefly explained in the chapter. Afterwards, the diverse applications of a resistor are explored where it is demonstrated that a resistor can be used for different applications based on a similar operation principle. The functionality of a thin-film RTD can be defined as a thermo-resistive flow-rate sensor or temperature sensor with a simple modification in the operation mode. The flow-rate and temperature sensor of the MPSC is also a thin-film RTD. The difference between these two sensors lies in their physical structure and operation mode. Hence, the detailed mechanism behind the different application of an identical resistor is explained at the end of this chapter. The designed temperature sensor is also illustrated in this chapter. The importance of water temperature measurement is highlighted since several physical and chemical parameters depend on water temperature. The relationship between the temperature and the other parameters of the water is provided. In the end, the discussion about the experimental results is reported.

Chapter 4 includes a comprehensive study of the flow-rate sensor. The considered flow-rate sensor is a thermo-resistive water flow measuring sensor, which senses the water flow by transferring the heat from the resistor to the operation medium (water). Different operation methods have been developed so far for the thermal flow-rate sensor. The three conventional operation principles: *Anemometric (Hot-wire)*,

Calorimetric and *Time-of-flight (TOF)* are stated in this chapter. The flow sensing device of the MPSC is operated under anemometric operation mode. The primary prototype of the flow-rate sensor was fabricated on a glass substrate and the subsequent devices on the silicon with further important and crucial physical modifications. All the numerical and experimental results related to the different versions are discussed. A comparative study of the different models of the sensor is reported at the end of this chapter so as to provide a better understanding of the effectiveness of the proposed approaches and routes towards optimization.

Finally, this thesis dissertation is ended up with a general conclusion about the four physical MEMS sensors of the MPSC and few suggestions regarding the future works are also stated.

Part I: Multi-Parameter Sensing Chip

Non thermal sensors

1 Chapter 1: Background on environmental monitoring (Air & Water) and related measurement tools

1.1 Fundamental natural resources for life and the necessity for environmental monitoring

For decades, there were numerous attempts to invent an efficient technological solution to monitor the environment and at the same time, to provide early warning about the pollution. At the very early stage, the monitoring techniques rely on classical offline analysis system. This requires collecting a sample and performing the analysis in a laboratory, but this process needs a long operational time and costly resources to get the necessary data. Therefore, the traditional laboratory-based procedure appears non-resilient as it may lead to substantial risk for the environment and human health simultaneously. With the evolution of the technology, the trend is to build an intelligent and real-time multi-parameter monitoring system. Rather than creating a parted monitoring device for the different parameters; it is more pointful to design a monolithic multi-parameter sensing device. Thanks to the proven advantages of microfabrication technologies, a miniaturized modular format for such multi-parameter sensing device saves money and allows large-scale implementation in the plausible media. At present, there are several techniques and devices developed with the combination of smart electronic and computer interface in respond to this demand. Some devices are focused on measuring some specific parameters where the others are designed for measuring different parameters simultaneously.

Majority of the environmental monitoring systems are designed for monitoring one of the two most crucial elements of the environment which are *air* and *water*. Since these two elements are directly related to the human being health and their effects become visible very rapidly. Contaminated air and water cause both the short term and long term fatal diseases. An average estimation shows that a person spends around 90% of his life at indoor³ and water is an essential ingredient for a person to complete his daily life activities. Therefore, the purity and cleanness must be ensured of these two essential elements in order to lead a sound and healthy life.

1.2 Air Quality Monitoring

The monitoring of indoor air quality (IAQ) and outdoor air quality (OAQ) both are important for the human well-being. Normally, it is comprehended that the IAQ is better than the OAQ, but evidence illustrates that the presence of the pollutants in the indoor air may be two or five times greater than the

outdoor air³. As a consequence, the air quality monitoring concern is shifted from outdoor to indoor in the last ten years⁴. There are several environmental risks for public health, which are traced out by the experts and the indoor air quality is always ranked in the top five³. Some serious health issues like heart and chronic respiratory diseases, lung cancer as well as short time sicknesses like fatigue and nausea are caused by poor air quality³. Several factors are responsible to degrade the air quality such as- biological factors, physical and chemical factors and sometimes their combination⁴. Daily activities of mankind also produce some harmful substances which increase the number of the air pollutants. Particularly, the indoor air gets polluted by a Volatile Organic chemical Compounds (VOCs) from manufactured construction materials and adhesives, paints, dust particles from carpets, treated wood and particles board⁵. Household cleaning chemical products and redundant use of air freshener in a closed environment are also reducing the IAQ.

IAQ can be determined by measuring the concentration of different pollutants in the indoor air. Carbon dioxide (CO₂), carbon monoxide (CO), ozone (O₃), sulfur dioxide (SO₂), nitrogen dioxide (NO₂), temperature, relative humidity (RH) and Volatile Organic Compounds (VOCs) are the main parameters which indicate the cleanness of the indoor air^{4,6}. The threshold level of CO, SO₂, NO₂ and O₃ in an indoor environment is already specified by EEA (European Environment Agency) which is 10 µg/m³, 350 µg/m³, 40 µg/m³ and 120 µg/m³ respectively⁷. All the mentioned compounds are individually responsible for different diseases in the human body. Staying for a long period of time in an excessive CO₂ concentration environment causes perspire, long time faint, blurred vision and headache⁸. Huge variation of temperature during different seasons is representing skin and inner limbs diseases. During winter the old aged people and the children are suffering from respiratory and cardiovascular diseases⁹. Excessive heat leads to heat stroke for the people those who are working under sunburn for a long time and causes heat rashes as well¹⁰. If the percentage of the RH in the air is less than or surpass the standard value, then it creates some adverse effects on the health. Low RH enhances to spread the airborne disease and cause eyes irritation. It is harmful to the respiratory system as well as mucous membranes are produced inside the respiratory system due to the low RH¹¹. Besides, high RH leads to allergies, respiratory infection, dysphonia and wheeze¹². The suggested moderate value of RH in the air to avoid the negative health effects is 40%-60%¹¹. Overmuch VOCs quantity present in the air is determined as one of the possible reason for sick building syndrome (SBS)¹³.

Nowadays there are plenty of devices and measurement methods are developed by the researchers to determine the IAQ. The classical measurement methods are building an air quality monitoring station, but this sort of measurement system is costly and provides low resolution sensing data¹⁴. Moreover, this type of monitoring station is not autonomous always and there is a need for an operator. Another short come is accumulating different sensing devices on the same system. Therefore, the traditional measurement method

does not allow for large-scale implementation and multi-parameter measurement simultaneously. The recent technologies are more focused on to develop miniature multi-parameter measurement system based on real-time analysis and remote access to extracted data. The existing devices are based on different working principle like- chemical analysis, using metal oxide sensor array, using optics, etc. ^{4,15,16}. Some of them are using manufactured sensing elements, where some of them fabricate their own sensing elements. *Sherin Abraham and Xinrong Li* develop a Wireless Sensor Network System (WSNS) indoor air quality monitoring system using Arduino, XBee modules and the sensing elements are micro gas sensors ³. The device is presented in Figure 1-1.

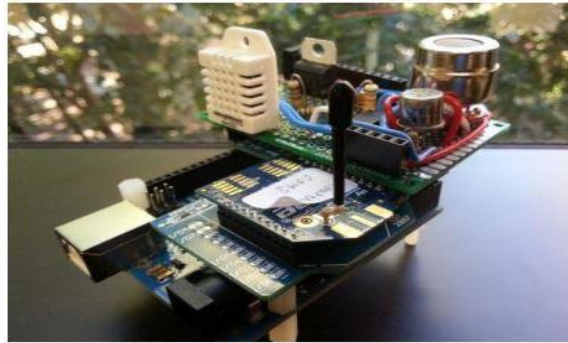


Figure 1-1: WSNS based IAQ monitoring device

The Arduino board is the data processing unit and for wireless communication established by using XBee module. *Péter Volgyesi et al.* develop a mobile air quality monitoring system, where the sensor node is mounted on a car for measuring the different pollutants in the outdoor air ¹⁷. The sensor prototype is demonstrated in Figure 1-2. The data sampling rate differs when the car is moving and when it is parked. During stationary mode, the samples are taken few times an hour and when the car is in motion the sensors are sampled every minute and the data are stored with the location and time stamp using onboard global positioning system.



Figure 1-2: The Mobile sensor node

The measured data are uploaded to the server periodically and after processing the measured data they are published on the SensorMap portal. Another multi-sensor gas module device is proposed for smart home automation by *B. Ivanov et al.*, which is an automated decentralize indoor climate or air quality monitoring system¹⁸. It can detect the relative humidity and the temperature of the air along with some harmful gases like- CO, CO₂, O₃, H₂ and H₂S and flammable gases as well.

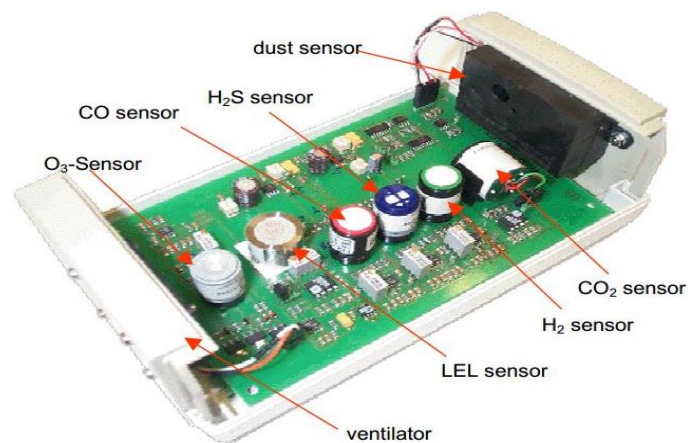


Figure 1-3: Experimental design of Multi-sensor module for indoor climate monitoring

Figure 1-3 illustrates the experimental design of the multi-sensor module for indoor climate monitoring. The whole prototype consists of other two devices which are wireless wearable device and BGA Micro-sensor. The wireless wearable device is designed for the thermal comfort of the user. It measures the most relevant parameter of the air surrounding to the user and turns on the appropriate HVAC (Heating, Ventilation and Air-conditioning) system to create the desire comfortable environment for the user. Besides,

the BGA Micro-sensor is sensing module where all the sensing elements of the desired parameter are co-integrated on the small footprint in order to achieve easy installation and reduce power consumption.

1.3 Water Quality Monitoring

The necessity of water monitoring is no way less significant than air quality monitoring. Both of them are equally essential for the human being to survive on this planet. Monitoring is needed at a different level in the case of water. Due to the rapid urbanization all the natural and unnatural sources of water such as a river, lake, catchments, underground water, etc. are getting polluted and without chemical or physical treatment the water directly from the source cannot be used for drinking or doing any household work. Therefore, the monitoring is important to avoid contamination at the source level as well as during the treatment operation. Moreover, there is a water distribution network by which the water is carried from the source or water plant to the user end. Monitoring is more crucial for the distribution network since poor maintenance or any accidental leakages in the distribution network cause huge water loss and unaware contamination, which increase both the health risk and economic loss. Water quality monitoring is related to the determination of physical, chemical, biological and to some extent microbiological characteristics of the water. The extracted data from water monitoring are used to take any decision regarding health and environmental issues.

Nowadays, four methods of water monitoring are available- **a)** sampling with a potable water quality monitoring device and following lab analysis, **b)** Continuous monitoring of water environment by an autonomous monitoring system, **c)** Water quality monitoring using remote sensing technology **d)** Ascertainment the presence of a poisonous substance in the water using the sensitivity of aquatic organism¹⁹. Although significant advances are achieved recently in the water quality monitoring technology but yet there is still a need to build an online efficient monitoring system which can measure multi-parameter simultaneously in a cost-effective way.

The idyllic miniature microsensor arrays are cost-effective which allows large-scale implementation and easy installation. The convenience of using microsensors for the water network monitoring is that it is suitable to monitor complex distribution infrastructure. Some smart sensing system can provide an early stage warning about the contamination which is really helpful to avoid possible health risk due to the polluted water. Generally, an early warning system consists of instrumentation technology monitoring system along with data analysis and interpreting in real time²⁰. The recently available devices which are manufactured by different companies for water quality monitoring, the mode of operation of those devices are based on different physics.

The water quality and water network monitoring can be addressed by investigating some key parameters like- pH level, chlorine, temperature, pressure, flow-rate, conductivity, turbidity, heavy metals, phosphates, nitrates, dissolved oxygen^{19,21,22}. There are numerous sensors capable of measuring one of the above-mentioned parameters. We will not elaborate on those individual sensors here as there is a very rich variety of these. Some of them are even based on micro-fabrication technologies, which lead to a reasonably low-cost. However, the global emphasis is on an autonomous on-line multi-parameter microsensor based water quality monitoring system, which is capable of measuring several parameters using the same device. In order to reach this objective, there are at least 3 approaches:

(i) – Sensor array or electronic tongue. Somehow similar to the electronic nose concept, this approach is based on taking advantage of the different responses of several sensors on different chemical species, so as to build a correspondence table or implement machine learning algorithms. Even though it is very promising, the Technology Readiness Level (TRL) of this approach is still very low, still far from commercialization. We will not elaborate on it in what will follow.

(ii) – Multi-parameter sensing based on Analytical Chemistry, which includes optical spectroscopy, chromatography techniques as well as mass spectrometry. Some of those techniques can lead to ultra-compact miniaturization.

(iii) – Multi-parameter sensing measurement devices, based on co-integration of several sensors onto the same device. This co-integration is mostly based on the heterogeneous integration of sensors outsourced from different providers, leading to high cost (a few k€ up to 10 k€), mainly due to the need for assembly of those sensors and related low fabrication yield. This is the approach chosen in our work, targeting full monolithic co-integration on a single chip.

1.3.1 Analytical Chemistry for multi-parameter sensing of chemical pollutants of water

A submersible multiple water quality measurement device which can measure the total organic carbon (TOC) equivalent, biochemical oxygen demand (BOD), turbidity, an aromatic compound, nitrate and nitrite in the water. This device is manufactured by spectro::lyser^{TM23} named s::can whose working principle relies on ultraviolet-visible spectroscopy. The device is shown in Figure 1-4.



Figure 1-4: s::can multi-parameter water quality monitoring device based on UV-VIS spectroscopy

The company ONDAVIA Inc²⁴ uses Raman Spectroscopy for the quantitative detection of chemical micro-pollutants down to the sub-ppb concentration level. The measurements require water sampling. A droplet of water is then fed into a disposable microfluidic chip, embedding gold nanoparticle for plasmonic signal amplification (SERS: Surface Enhanced Raman Spectroscopy). Those disposable chips are also chemically functionalized so as to fit with a specific chemical target. Although very sensitive and very selective, this approach is not compatible with continuous online monitoring.

In addition, besides spectroscopy, there are other analytical chemistry instrumentation techniques that are used in several multiple parameter monitoring devices by different companies to trace the organic micro-pollutants like- gas chromatography-mass spectrometry (GC-MS), liquid chromatography-mass spectrometry (LC-MS) etc. ²².

1.3.2 Multi-parameter sensing probes for water network monitoring

Within the category of multi-parameter sensing probes presented above, the most comprehensive is probably the Intellisonde system provided by the Intellitect company. It is based on heterogeneous co-integration and is. However, it is worth mentioning that there are already a few commercial multi-parameter probes, which are based on co-integration of different sensors on the same sensor chip [the KAPTA 3000 from ENDETEC²⁵ and the SIX-SENSE from CENSAR²⁶. However, our solution developed in the frame of the PROTEUS project is expected to out-perform those solutions in many aspects:

- Increased measurement capabilities: 7 up to 9 different parameters will be accessible.
- Reconfigurability of some sensors (flow-rate and conductivity) is expected to allow addressing different measurement ranges and hence, different needs using the same probe.

- Redundancy allows better addressing reliability issues as well as improved possibilities regarding temperature compensation schemes.
- Improved anti-biofouling is targeted, which is expected to provide longer lifetime and/or significant reduction of maintenance needs.

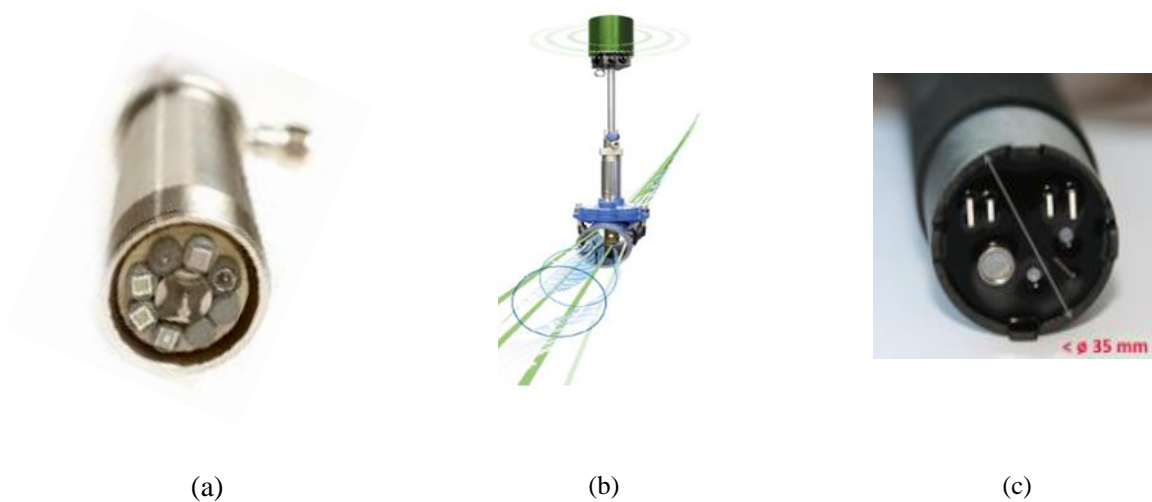


Figure 1-5: Commercially available multi-parameter sensing probes from- (a) Intellitect, (b) Six Sense and (C) Endetec.

1.3.3 Particulate and microbiological pollutants

It is also worth mentioning that besides the chemical pollutants, discussed before, there are two additional types of pollutants: particulate pollutants and biological pollutants; several commercial products are available for detecting this kind of pollutants. For instance, the company JMar BioSentry™ developed a device which can monitor the particles in the water²⁷. The device works based on laser technology and on-line measurement system. Figure 1-6 shows the water particle monitoring system.



Figure 1-6: Laser-based water particle monitoring system BioSentry ²⁷.

Regarding pollution by biological micro-organisms, one can cite the commercial product of two startup companies: FLUIDION ²⁸ and Parasitometer from WATER OPTICS TECHNOLOGIES ²⁹. These companies developed an effective warning detection system for bacteria and total coliforms, on one hand, and cryptosporidium, on the other hand, respectively. Both systems rely on advanced optofluidic technologies but they remain bulky and rather expensive, which makes them not suitable for large-scale deployment.



(a)



(b)

Figure 1-7: Detection Micro-biological water contamination alert systems, based on optofluidic technologies. (a) Parasitometer from Water Optics Technologies and (b) E-Alert system from FLUIDION

2 Chapter 2: Co-integration of Multi-Parameter Sensor Chip (MPSC) for Water Network Monitoring.

2.1 Introduction

The considered MPSC has different versions and the fabrication processes differ with respect to the physical structure of the corresponding versions which came out sequentially through the project with increasing sophistication as well as increased capabilities in terms of co-integration of various kinds of sensors and related performance. The chip versions vary from each other according to their substrate material, sensing elements arrangement and distinct sensors' configuration and even their topography. It is challenging to obtain fully functional manifold parameters sensing elements on a small foot-print. Therefore, in order to facilitate the fabrication, integration and measured responses readability, a homogenous transduction principle is adopted for all the sensors, which is the resistive read-out. This means that all the sensors' responses to the corresponding different parameters of interest will be expressed in terms of a resistance variation. The reason and the benefit of selecting resistive sensing elements for the multi-parameter will be illustrated in the next section. In this chapter, the evolution of the different MPSC versions and their fabrication details will be introduced.

2.2 Choice of Resistive Readout

The data reading procedure based on resistive readout is the process of measuring a specific parameter by the means of resistance variation of the sensing element of a sensor device. Both the chemical and physical sensing elements of the MPSC are operating based on this principle. Each of the chemical sensors changes their resistance level according to the presence of the selective chemical substance in the water. Likewise, the physical MEMS sensors also provide an indication varying their resistance value as they are introduced to the corresponding different physical parameters of the water. In such case, each sensor has to be designed so that it is selectively sensitive to a given parameter solely –or mainly. There are many advantages of using resistive readout for all sensors of the sensing system. Resistive sensing is one of the simplest transduction manners which allow easy electronic readout in comparison with the capacitive sensing for instance³⁰. Furthermore, when comparing resistive and capacitive transduction schemes, it appears that capacitive transducers exhibit high impedance, which makes them behave such as antennas, in a sense that they are very sensitive to surrounding electromagnetic radiations, which can lead to parasitic signal at the sensor's output. On the contrary, resistive transducers have low impedance; they are therefore ideal for immunity to electromagnetic interference. This is of particular importance when considering

multiple sensors on the same chip that may interfere with each other. From this point-of-view resistive readout is expected to minimize crosstalk between neighbour sensors. Besides the sophisticated micro-fabrication technology, constructing resistive sensing elements are simple as well, which involve mainly patterning of thin-film materials. Moreover, the resistive sensing system allows fabricating multiple sensors on a small footprint since the resistance value is scalable by controlling the ratio of length over width. For instance, the pressure sensor of the MPSC is made of polysilicon strain gauges, which measure the mechanical tensile and compressive stress levels on a thin membrane-based on the piezo-resistive effect, which involves a resistance variation. This kind of piezo-resistive pressure sensor has high gauge factors and it can sense very small strain. On the other hand, the realized temperature and flow-rate sensor are based on a thin-film RTD (Resistance Temperature Device) made of platinum that exhibits a significant variation of the resistance value due to a small variation in temperature. The high sensitivity and linearity of such resistive devices makes them extremely useful for this kind of applications.³¹

2.3 Fabrication

As it was mentioned above, several versions of the MPSC were fabricated and tested in order to find out the suitable form of the MPSC through successive improvements. The primary version of the MPSC was fabricated on a glass substrate and the subsequent versions are on silicon. The substrate material was switched from glass to silicon so as to enable co-integration of the pressure sensor with the remaining sensors on the same chip. In the primary version, all the physical sensors –except the pressure sensor, were successfully co-integrated on the glass substrate using a simple process involving only metal micro-patterning. The co-integration issue will be discussed in the following sub-section. Based on the substrate material and fabrication process, the whole fabrication sequence can be divided into some sub-categories such as: (i) *metal on a substrate –either glass or silicon*, (ii) *silicon substrate with back-side etching*, (iii) *silicon substrate with front-side etching*, (iv) *silicon substrate with both the front and back-side etching*.

2.3.1 Metal on Glass and co-integration challenge

The primary prototype of the MPSC was fabricated on a glass substrate. This version has the allocated space for the chemical sensors and three physical sensors: water conductivity, temperature and flow-rate, which were successfully co-integrated on that version. The three physical sensors were realized by easy metal micro-patterning following conventional Lift-off process. Completion of the chemical sensors required post-processing of the chip. This post-processing was done at LPICM (Ecole Polytechnique/CNRS) by ink-jet deposition of functionalized carbon nanotubes (CNT). The cross-section view and the photo of the real fabricated sensor chip are reported in Figure 2-1 below.

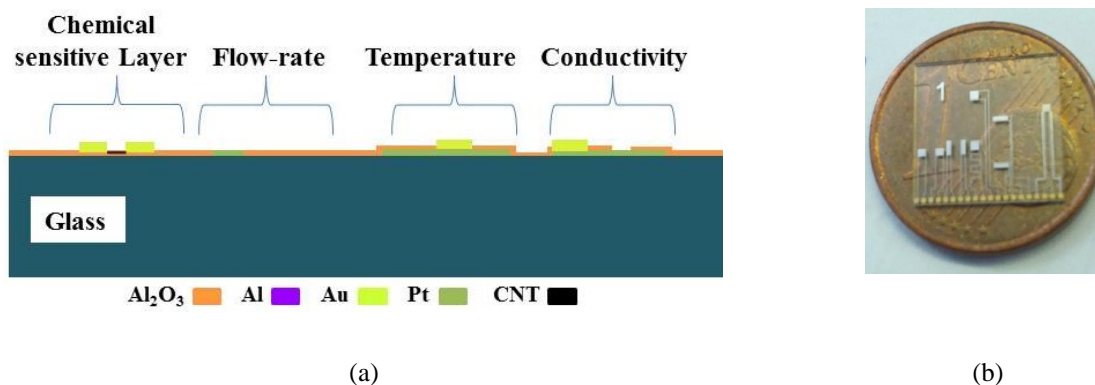


Figure 2-1: (a) Cross-section view of the multi-parameter sensor chip based on a glass substrate and (b) fabricated multi-parameter sensor chip on a glass substrate

At first, the platinum (Pt) was deposited on a 500 μm thick glass substrate by metal sputtering. The Lift-off process was used to create the metallic pattern of the sensing elements. In some trials, there was an additional thin surface coating layer (10 nm) made of Al₂O₃ erected by the Atomic Layer Deposition (ALD) technique. The aim of this coating layer is to protect the sensor chip against the biofouling under the water environment. A similar coating layer also created using TiO₂ in some versions in order to identify the most efficient protective layer without degrading the sensitivity of the sensor; particularly in the case of the conductivity sensor, whose metallic electrodes are directly exposed to water.

Hence, the first version contains all the sensors except the pressure sensor. The pressure sensor cannot be fabricated in this version together with the others due to the substrate material constraint. The ascertained pressure sensor is a piezo-resistive sensor whose working principle depends on the deflection of a thin membrane on the top of which strain gauges can sense the corresponding mechanical strain. Therefore, a thin membrane is an indispensable part of the pressure sensor. Using silicon is the conventional method to create such membrane together with strain gauges so as to realize such pressure sensor³². In conclusion, the silicon substrate is mandatory for the MPSC as a substrate material for accumulating all the sensors on the same chip.

As a consequence, a co-integration issue arises regarding the pressure sensor with others from the perspective of the substrate material. In the following section, the challenges involved in the co-integration process and its impacts on the sensor performance will be addressed comprehensively.

2.3.2 *Metal on a silicon substrate and first full co-integration of the whole sensors*

Here, in this version silicon was used as the substrate instead of glass and another glass wafer was used as a support under the silicon so as to obtain a sealed vacuum cavity. The pressure sensor membrane was created using single-crystal silicon layer of an SOI substrate while polysilicon was used to achieve the strain gauges on top of this membrane. The fabrication procedure starts with a pressure sensor, henceforth the others. After the initial cleaning of the wafer, the process starts with a thermal oxidation. The resulting silicon dioxide (SiO_2) layer is necessary to reduce the conduction heat loss since there is some Joule heating due to the thermo-resistive sensors, like flow-rate and temperature sensors. Indeed those sensors require such thermal insulation because the thermal conductivity of the silicon is quite high. Especially, the importance of thermal insulation layer is somewhat more critical in the case of the flow-rate sensor. Such an insulation layer was not required with glass substrate since glass has inherent high thermal insulation property. The thickness of the SiO_2 insulation layer on top of silicon is about 450 nm. Afterwards, a 400 nm thick polysilicon layer was deposited on the top of the oxidation layer in order to create the strain gauge. The latter step was the hard mask patterning of back-side and subsequent backside etching of the silicon substrate. The etching was performed using the DRIE method. Hence, the last step is to remove the hard mask for enabling the silicon-glass anodic bonding at the wafer level. The schematics of the main fabrication phases are presented sequentially in Figure 2-2 along with the photo of silicon-based MPSC. It is worth mentioning that at this stage only physical sensors are finalized. Further post-processing (by CNT printing at LPICM) is required to implement the chemical sensors on top of the dedicated array of electrode pairs.

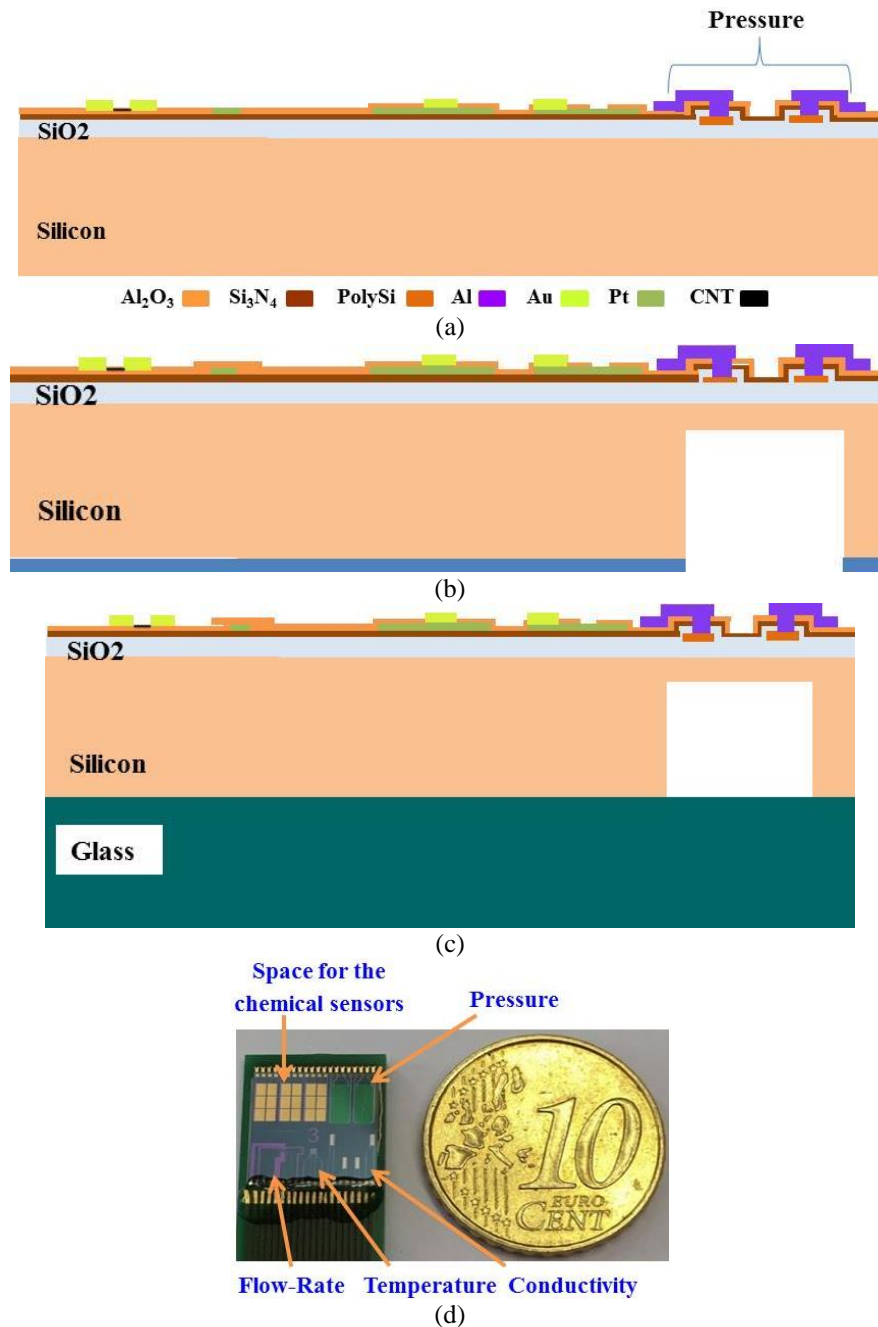


Figure 2-2: Different fabrication phases of the silicon-based MPSC. (a) Front side patterning of the device- pressure sensor fabrication together with the other sensors, (b) hard mask patterning on the back side and back-side DRIE for creating the membrane, (c) removal of the hard mask for silicon-glass anodic bonding and (d) micrograph of a co-integrated multiple sensing elements on silicon at the chip scale, after wafer dicing.

All the proposed sensors are co-integrated on the same chip successfully using silicon as the substrate material. Hence, this success could not lead to the conclusion due to the negative side effect of the silicon substrate on the flow-rate sensor performance. Indeed, the optimal heating condition is essential for a

thermal flow-rate sensor for its proper transduction. Therefore, an efficient thermal insulation is requisite between the heater resistor and the substrate material. Due to the high thermal conductivity of the silicon, the heating element of the flow-rate sensor losses heats at the substrate through the conduction process. As a consequence, the sensitivity of the flow-rate sensor degraded significantly with respect to the water flow. The related experimental results are presented in Chapter 4.

Hence, the rather high conductivity of the silicon substrate material and its negative consequence on the flow-rate sensor performance arise a critical situation. No alternative can be considered other than the silicon to fabricate the pressure sensor and using silicon will debase the flow-rate sensor's sensitivity. The further increment of the insulation layer thickness is not possible due to the fabrication limitation on thermal oxidation. So, to overcome this problem, geometric and topographic optimization appeared as the only options. The physical configuration of the flow-rate sensor had to be modified to reduce the conduction heat loss. In the beginning, a membrane was introduced under the flow-rate sensor which was created according to the similar manner as like the pressure sensor to minimize the heat loss. The schematic cross-section view of the membrane-based flow-rate sensor is provided in Figure 2-3.

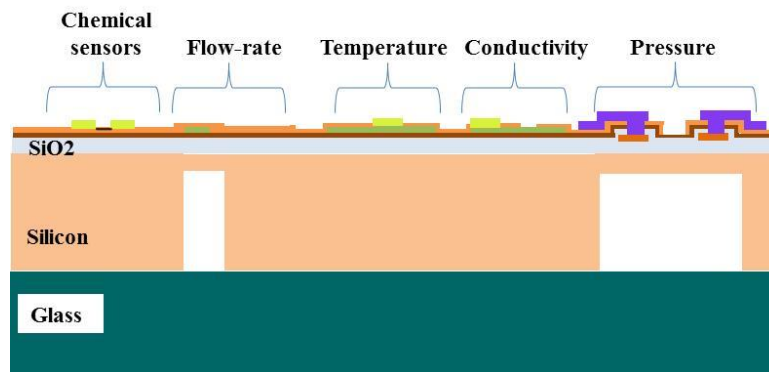


Figure 2-3: Cross-section view of the membrane-based flow-rate sensor

The inner medium of the membrane is a vacuum, so it is expected to improve the insulation level. The obtained measurement of the membrane-based flow-rate sensor exhibits insufficient improvement. Therefore, further optimization was required for diminishing the heat conduction.

The ensuing structure of the flow-rate sensor is a pillar-like structure, where the heating resistor is fabricated on a silicon pillar. The detail of this configuration is presented in the section below.

2.3.3 Silicon substrate with front-side etching: attenuation of the negative effect of the high thermal conductivity of the silicon substrate

The pillar structure flow-rate sensor is obtained by front-side DRIE etching. Several numerical parametric studies were conducted in order to extract the appropriate design parameters such as aspect ratio of the pillar and the cavity. The obtained numerical results express that the silicon pillar configuration exhibits higher sensitivity than the glass-based flow-rate device within the velocity range of interest. The extracted experimental responses showed a good agreement with the numerical one. It was observed from the numerical study that there is an inverse relationship between the pillar widths, hence the resistor widths and the sensor's sensitivity. Therefore, different versions of the pillar structure device were fabricated with different pillar widths and heights in order to study their impact on the sensor's sensitivity.

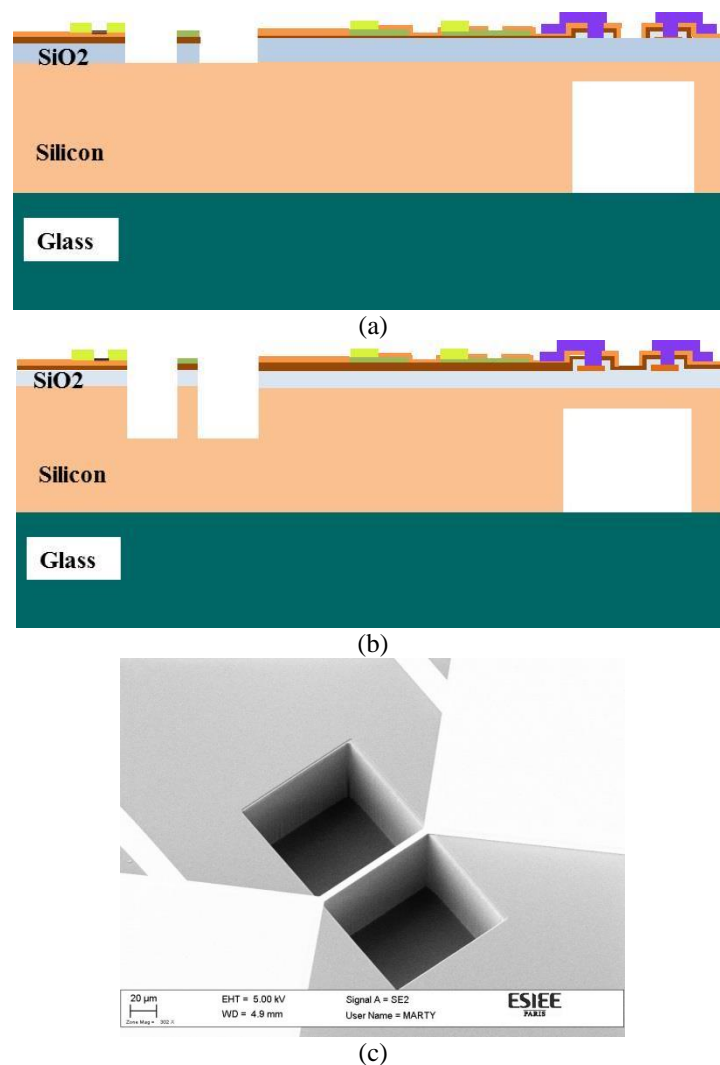


Figure 2-4: Fabrication sequences of the pillar structure flow-rate sensor. (a) Patterning of the front-side cavity and etching of the front side deposited layers, (b) front-side DRIE, (c) SEM photo of the resulting pillar flow-rate sensor

Figure 2-4 illustrates the fabrication sequences of the pillar structure flow-rate sensor, where Figure 2-4(a) shows the patterning of the cavity and etching the front side materials for creating the cavity and Figure 2-4(b) reports the fully etched cavity by DRIE with the silicon pillar.

This pillar structure flow-rate sensor solves the concern about the dual complexity- substrate material and the sensor performance regarding the co-integration process.

2.3.4 Flow-rate sensor on a silicon substrate with suspended heater

Flow-rate sensor with the suspended heater is a successive version of the pillar structure flow-rate sensor intended to achieve further improvement of the thermal insulation and hence on the sensor's sensitivity. The pillar structure flow-rate device evinces optimal sensitivity that is sufficient for the real application. Hence, the suspended configuration was proposed for further investigation about the diminution of the thermal conductivity in terms of geometric optimization. This suspended structure can be considered as a bridge, where the heater resistor of the flow-rate device is fully suspended from the substrate and the two ends are connected. Several versions were fabricated with different cavity depth and resistor's width. This device was fabricated very recently and due to the time constraint; the experimental measurement study could not be conducted. As a consequence, the results on this bridge structure flow-rate sensor are not included in Chapter 4. The 2D cross-section view of the bridge structure flow-rate sensor is shown in Figure 2-5.

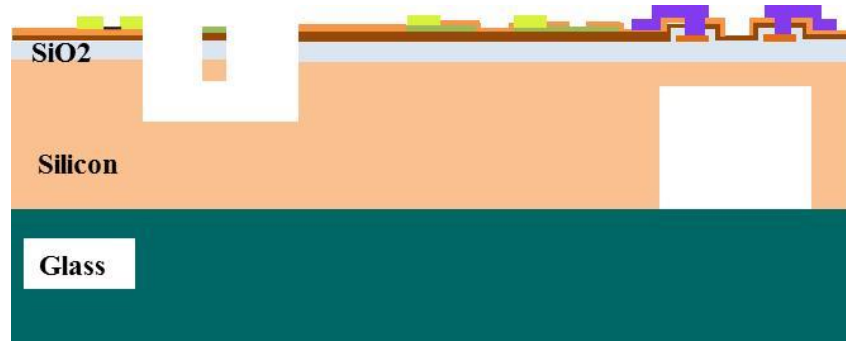


Figure 2-5: 2D cross-section view of the bridge structure flow-rate sensor

The fabrication process of the bridge configuration is quite similar to the pillar structure flow-rate sensor. The pillar pattern was obtained by an etching sequence including anisotropic etching and passivation followed by anisotropic etching step to release the bridge.

According to the fabrication details, it appears that the pressure sensor has a strong relation in terms of the substrate material choice and different versions of the MPSC. The evolution of different MPSC versions is largely influenced by the pressure sensor co-integration with the remaining sensors. Therefore, it is pertinent to present the pressure sensor here in this chapter. The conductivity sensor will be presented here

after the pressure sensor as well. The reason for the inclusion of the pressure and conductivity sensor in this chapter is due to their easy comprehensible physical structure and functionality with no intrinsic novelty. Only co-integration constraints are the main issues to deal with during the design phase and the corresponding elaboration on the fabrication process compatibility, allowing full integration of those sensors with all other sensors.

Before presenting more details on these two sensors, it is reasonable to discuss first how the sensor chip was electrically connected in order to measure their responses. Different electronic circuits and software interfaces were used to conduct the experiments for different sensors. Besides, a single PCB was used to connect the multi-sensor chip to the electronic circuits. The PCB was designed especially for the MPSC, which provides the option to connect the sensors separately. The detail of the PCB is presented in the section below.

2.4 Packaging of the MPSC into a Printed Circuit Board (PCB)

The physical shape of the PCB is like the English alphabet ‘T’. The PCB along with the sensor chip is presented in Figure 2-6. The aim of this particular design of the PCB is to make it compatible with the different experimental setups since the MPSC contains several sensing elements and the test setup is differing for each sensor. The height of this T-shaped PCB including the base is 7.2 cm and the width of the body part is 1.18 cm. The base is 0.89 cm in height and 3.82 cm in width. There are two sets of connection holes in the base of the PCB for connecting the sensors and each set contains 24 holes. The upper set is dedicated to connecting the lower part’s sensors of the MPSC and the beneath holes are for connecting the sensors which are fabricated on the top part of the chip. On the top part of the PCB, a square-shaped space is created to place the sensor chip on the PCB and the dimension of this space is 1 x 1 cm. An adhesive is used to glue the chip on the PCB. The electrical connection between the chip’s connection pads and the PCB’s wire is done by gold wire bonding and a UV-cured epoxy is used to protect the wire bonding connection against water.

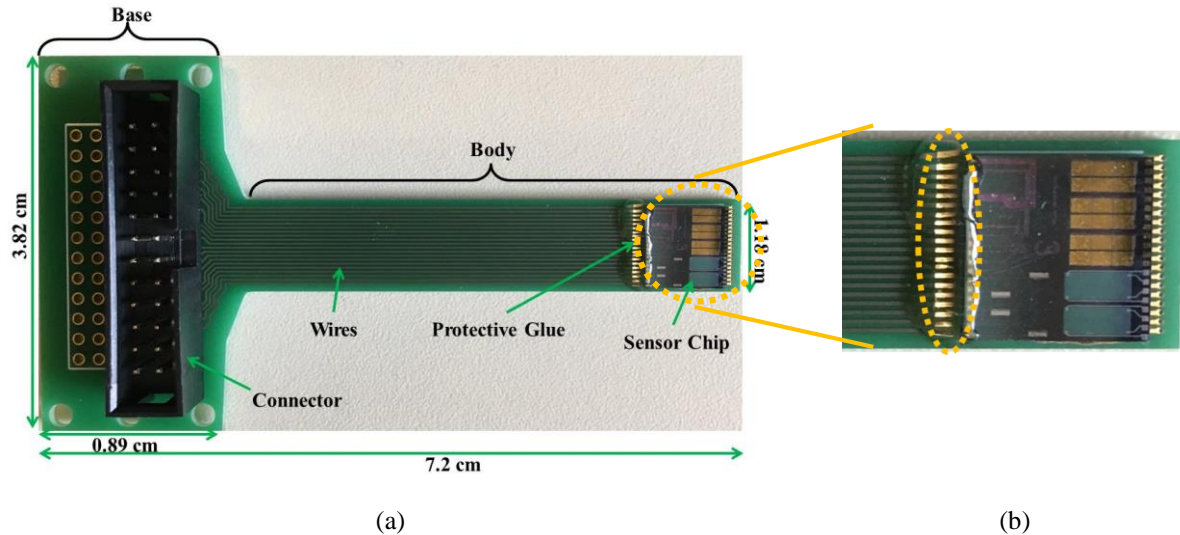


Figure 2-6: The PCB for connecting the sensors with an electronic circuit. (a) The whole PCB labelled with dimensions, (b) the zoomed image of the chip containing part, where the connection pads are wire bonded (dotted orange circle) to the PCB and protected hermetically with glue against the water. The other part of the chip is not connected to the PCB.

2.5 First Phase of the Characterization: Non-Thermal Aspects

Regarding the design details and characterization results of each type of sensor that we integrated on the MPSC platform, we have chosen to present in what follows, first, those sensors in which thermal aspects are neither fundamental nor critical for their operation principle, although the temperature may affect their response. These sensors are the pressure sensor and the water conductivity sensor. Later, another class of sensors will be considered, where thermal aspects are fundamental and require in-depth elaboration. Those are the temperature sensor, presented in Chapter 3 and the flow-rate sensor, presented in Chapter 4.

2.6 Pressure sensor design and characterization

The pressure sensor is well known in the MEMS area. It has diverse use in different fields for different applications i.e., automobile, aeronautics and industrial process control in the high-pressure industrial environment; besides in the field of bio-medicals under low-pressure environment^{33,34}. Other than the aforesaid applications, it has another promising suitability to monitor the water distribution network for reducing the non-revenue water lossⁱⁱ. Water loss due to the distribution network defect is a paramount issue for the respective authority in order to reduce the operational cost and saving the precious natural resource. According to the Energy and Water Department of the World Bank, the expenditure of the water

ⁱⁱ Non-revenue water (NRW) means the amount of water that does not generate any revenue. It is defined by the difference between the amount of the water supply to the distribution network and the amount of the water for that the consumers pay the bill³⁵.

adaptabilities due to the NRW is around fourteen billion dollars all over the world; one-third of that cost take place in the developing countries³⁶.

The water wastage due to the leakages in the distribution network and overflow from the reservoir can be minimized significantly by proper pressure management hence, monitoring the water pressure. The conventional technique of tracing the leakages in the distribution system is replacing the pipe or repairing. Due to the long period (a few weeks or a month) of such process completion causes significant amount water loss³⁷. Therefore, to avoid such unwanted losses proper pressure monitoring in the water distribution system is the most fruitful solution.

Numerous techniques and measurement devices have been developed for regulating the pressure management in the water distribution network. Among the existing devices and techniques, micro-machined devices are popularized due to their low-cost production and large-scale positioning. Different transduction principles are followed by the micro pressure sensing devices *i.e.*, capacitive, resonance, optical etc.³³. Piezo-resistive sensors are the smart choice among the prior mentioned micro-sensors for this specific application because of their convenient operation mode and moderate sensitivity to a wide pressure range with high resolution³⁴.

The realized pressure sensor of the MPSC is a piezo-resistive pressure sensor, based on silicon thin membrane. On the top of the membrane, there are four piezo-resistive strain gauges which placement is according to the Wheatstone bridge. The functionality of the membrane is involved in transforming the hydrostatic pressure into mechanical stress on the piezo-resistors. The thin-film membrane was created using the single-crystalline silicon of the upper layer of an SOI wafer. Strain gauges/resistors were made of thin-film polycrystalline silicon deposited by LPCVD on top of this membrane. In this case, the resistors were fabricated using polysilicon instead of the usual material because of their higher piezo-resistive sensitivity³⁸. The layout of the considered pressure sensor is illustrated in Figure 2-7.

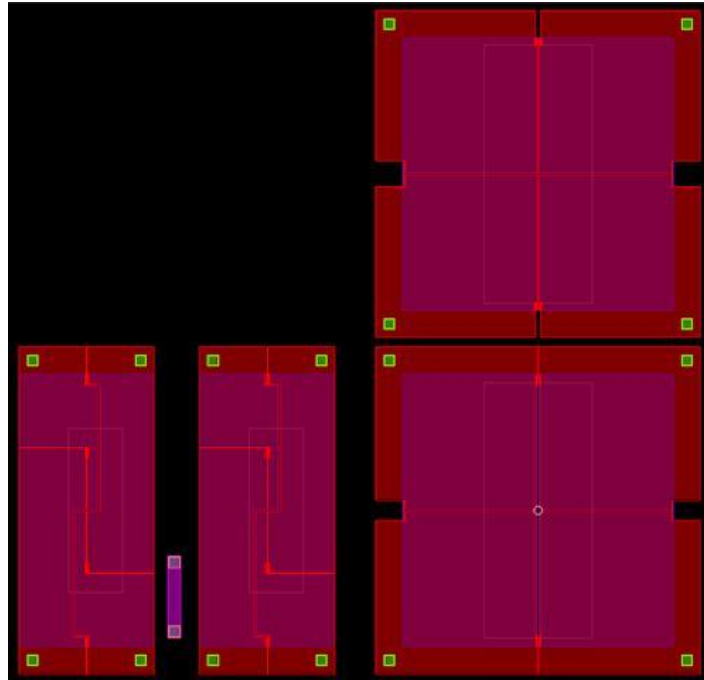


Figure 2-7: Typical layout of the MEMS pressure sensor. Different versions were considered in order to investigate the sensitivity with respect to the pressure.

Two different configurations of the considered pressure sensor have been realized where the membranes are in square and rectangular shape with different resistors arrangements. It has been observed from the numerical study that the V_{out} of the Wheatstone bridge depends on the membrane thickness and the resistors arrangement. As a consequence, two different structures were fabricated to investigate this phenomenon. The related results of the numerical study are reported in Annex 1.

2.6.1 Experimental setup

In the experiment, the sensors' responses were extracted as a function of the air pressure. The sensor was inserted into a glass bottle and the variable hydrostatic pressure was generated inside the bottle with the Fluigent SA device. The Fluigent SA can produce a pressure level up to 7 bars. The experiments were conducted until 3 bars maximum for the safety issue. The principal aim of the experiment is to inspect the initial response of the fabricated sensor. The measurements were obtained under hydrostatic air pressure; hence it is more reasonable to conduct the measurement underwater environment. Evaluation under the water can be performed using an intermediate water reservoir. The air pressure will be generated in the closed water reservoir, therefore the sensor' response will be measured. The photo of the test setup is demonstrated in Figure 2-8.

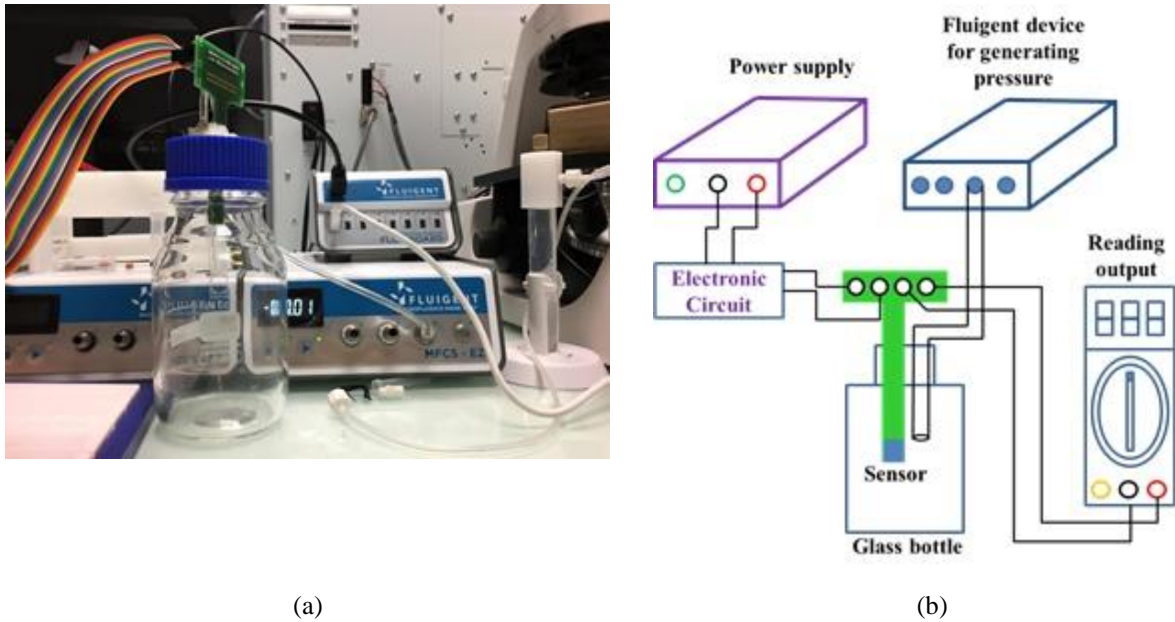


Figure 2-8: Experimental setup of the pressure sensor. (a) The sensor is inserted into the glass bottle and the surroundings of the insertion whole glued in order to make it leakage proof. A transparent plastic pipe is used to transmit the hydrostatic air pressure from the Fluigent SA to the glass bottle. (b) A schematic diagram which replicates the experimental setup of the pressure sensor.

The data reading circuit was built with an instrumentation amplifier AD620an. A DC voltage source was used to supply the power to the piezo-resistor Wheatstone bridge and the bridge output was connected to the instrumentation amplifier input. The bridge output will be varied linearly according to the applied hydrostatic pressure since the strain gauges are chained due to the pressure. The final output was collected from the amplifier end. A $5\text{ k}\Omega$ gain resistor was used to fix the gain at 10, but it can be changed to any other values according to the desired gain level. The schematic of the circuit is reported in Figure 2-9.

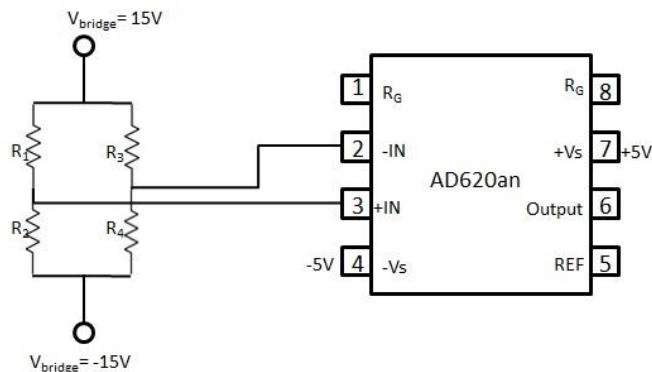


Figure 2-9: Schematic diagram of the data reading circuit. Here, the Wheatstone bridge consists of four resistors R_1 , R_2 , R_3 and R_4 represent the four piezoresistors of the pressure sensor.

2.6.2 Results and Discussion

Figure 2-10 gives an illustration of typical responses of the two pressure sensor. It is worth to mention that the responses of the pressure sensors were recorded under absolute pressure. This value was evaluated from the differential pressure produced by the experimental setup, assuming a value of 1 bar for the atmospheric pressure during the experiment.

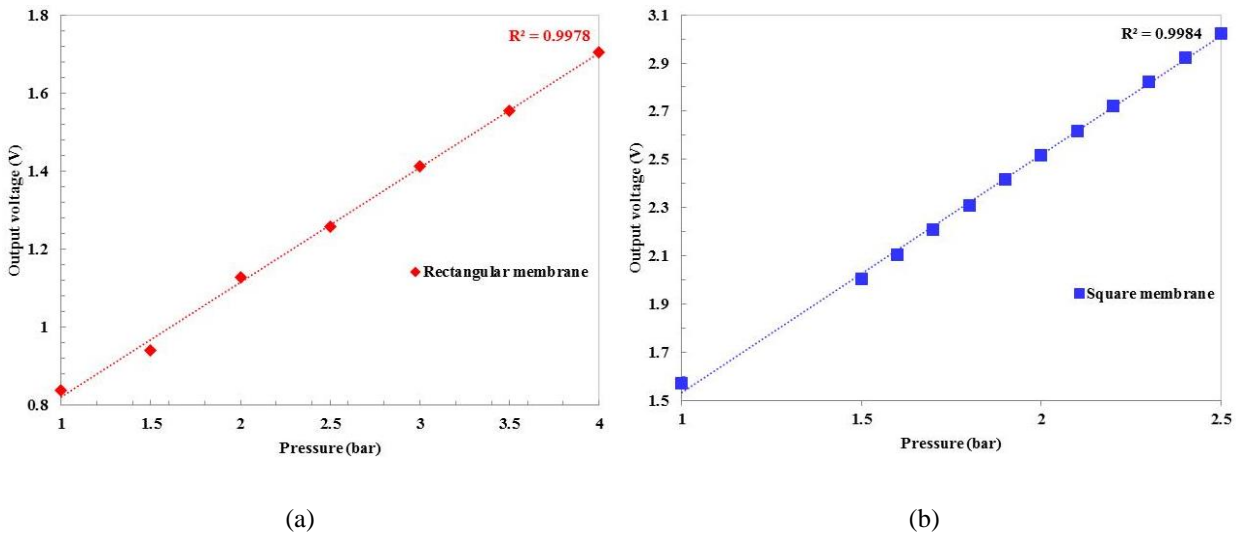


Figure 2-10: Measured responses of the (a) rectangular and (b) square shaped membrane pressure sensor. Excellent linearity is observed in both the cases with a coefficient of determination 0.998.

From the plots, it can be observed that both the sensors exhibit high linearity where the coefficient of determination values are higher than 0.99 with respect to the pressure increment. The output voltage magnitude differs for the two versions due to variation in the fabricated piezo-resistors' values.

2.7 Conductivity sensor design and characterization

2.7.1 Conductivity

Conductivity is the ability of a substance *i.e.*, metal, liquid and gas to conduct the electricity. The electricity is conducted through a metal by its free electrons. Hence, electricity cannot pass through an insulator since it does not contain any free electron. Likewise, the electricity passes through a fluid medium by the cations and anions of the corresponding fluid.

From this last statement, it appears that water conductivity is an efficient mean of measuring the ionic concentration of water. Hence it gives a rough idea of the ionic contaminants of water. Water conductivity can be regarded as an indicator of water quality, among other indicators, such as water turbidity for instance, which can be assessed by visual/optical manner.

Conductivity and conductance differ from each other. Conductance is related to conductivity, it is dependent on the length of related substance as like the term resistance³⁹. On the other hand, conductivity is related to the resistivity. Conductivity is correlated to resistivity but reciprocal. Conductance is measured in mho (or Ohm^{-1} , the reciprocal of Ohm) also named Siemens. The link between conductance and conductivity involves a surface to length ratio, similar to the link between resistance and resistivity. Conductivity is measured with the unit of the conductivity is S/cm ⁴⁰.

Some basic equations are recalled hereafter, which are useful to understand the experimental measurement protocol.

Conductance (G) is defined as the reciprocal of the electrical resistance (R) of a solution between two electrodes: $G = 1/R$. On the other hand, electrical conductivity σ is defined as the ratio between the current density (J) and the electric field intensity (E) and it is the reciprocal of the resistivity ρ , whose unit is Ohm.cm . $J/E = \sigma = 1/\rho$. The SI unit of conductivity σ is Siemens per meter (S/m). However, practically, it is not straightforward to measure current density J and electric field E . Therefore, the water conductivity ρ_w is derived from measurements done on the water resistance R_w , which is more easily attainable through the measurement of both voltage V and electrical current I . Indeed, from Ohms' law: $V = R_w I$, where V is the voltage difference across the water plug, R_w is the electrical resistance of this water plug and I is the current flowing through the electrodes placed at the borders of the water plug.

We also know the following relation between resistance R_w and water resistivity ρ_w : $R_w = \rho_w L/S$. Here L and S is the length and surface area of the water plug, respectively. Now this equation can be rewritten as:

$$R_w = 1/\sigma_w \text{ (L/S)} \quad (2-1)$$

Replacing the resistance R_w by the ratio V/I , we obtain $V=1/\sigma_w \text{ (IL/S)}$ that can be finally rewritten in, the following form:

$$1/V = \sigma_w \text{ (S/IL)} \quad (2-2)$$

In the latter equation, $1/V$ is the reciprocal of the voltage V . It appears directly proportional to the water conductivity σ_w , with a proportionality factor (S/IL) that can be seen as a scale factor, which can be determined through a calibration phase. In such a calibration phase, we need to use calibrated water samples, which means the whose value of $\sigma_{w\text{-calibrated}}$ is known a priori. Then, plotting the curve ($1/V$) versus $\sigma_{w\text{-calibrated}}$ gives a linear response, whose slope is (S/IL). After completion of such sensor's calibration, it can be used to read water samples of unknown conductivity.

2.7.1.1 Water conductivity

It is mentioned in the previous section 2.7.1, that the conductivity of a fluid depends on the ions concentration. So, the conductivity hence the ability of electrical conduction of water depends on its ions concentration ⁴¹. The ions in the water are produced by the dissolved salts. Moreover, some inorganic materials such as- chlorides, alkalis, sulfides and carbonate compounds also increase the ions in the water ⁴². These dissolved compounds are known as electrolytes. If a water sample contains a high concentration of ions, then its conductivity will be higher. For this reason, the conductivity of the sea water is comparatively high. On the other hand, distilled or deionized water behaves like an insulator due to the low ions present in the water ⁴³ with a lower theoretical limit of the conductivity equal to $0.04 \mu\text{S/cm}$ at 20°C and even down to $0.01 \mu\text{S/cm}$ at 0°C for ultrapure water ⁴⁴, in an ideal situation where the only ions are H_3O^+ and OH^- .

2.7.1.2 Typical water conductivity values

There is no standard value of the water conductivity for different water sources. Each of the natural sources possesses different conductivity ranges. Usually, the conductivity of a specific waterbody depends on the geological surrounding. Due to the geological effects, a freshwater source has a wide conductivity range. Some lakes exhibit high salinity or conductivity because of the restricted outflow and the presence of particular ionic compositions ⁴⁵. In the case of a river, the conductivity varies a lot since the river water consistently influenced by the flow of the fresh and salt water. On the other hand, the conductivity of the seawater depends on the salinity and the temperature of the water ⁴⁶. Although there is no defined

conductivity value of the water sources, hence the typical conductivity ranges are presented in Table 2-1 below proposed by different organization ^{47,48}.

Table 2-1: Conductivity ranges of different water

| Water source | Conductivity range ($\mu\text{S/cm}$) |
|-----------------------|---|
| Ultrapure water | 0.04 (@ 20°C) |
| Distilled water | 0.5 - 3 |
| Tap water | 50 - 800 |
| Melted snow | 2 - 42 |
| Freshwater | 100 - 2000 |
| Portable water (US) | 30 - 1500 |
| Seawater | 55000 |
| Industrial wastewater | 10000 |

2.7.1.3 Importance of conductivity

In order to determine the water quality, the conductivity hence the specific conductance is one of the most commonly measured parameter ⁴². Besides, the conductivity information of a water body is used to calculate the salinity and total dissolved solids (TDS). Generally, a water body has a stable conductivity level which can be considered as a reference value for comparison with future measurement ⁴¹. There are several factors that can affect the conductivity of the water. Rapid change in conductivity of a water source may occur if the water flows over a soil which is rich in salt and minerals. In addition, natural flooding, evaporation, and manmade pollution can also vary the normal conductivity of water body.

The deviation of the conductivity by any portion from the normal value of a water body indicates the occurrence of a contamination. Addition of any chemical compounds, particularly the chloride, phosphate and nitrite ions due to the sewage leakages or agricultural runoff will increase the conductivity of the water ⁴¹. Moreover, an amalgamation of the elements those are not decomposed into ions in the water or accidental oil spill over to the water will actually decrease the conductivity ⁴⁹. Hence, any increment or decrement of the usual conductivity level has a negative impact on the water quality.

2.7.2 Introduction of the conductivity sensor and its working principle

The considered conductivity sensor consists of four probes, where two of them for injecting current to the operation medium and remaining two for measuring the wafer voltage. The conductivity information σ_w is obtained according to the equation below (as discussed in section 2.6.1)-

$$\sigma_w = \left(\frac{L}{S}\right) I/V \quad (2-3)$$

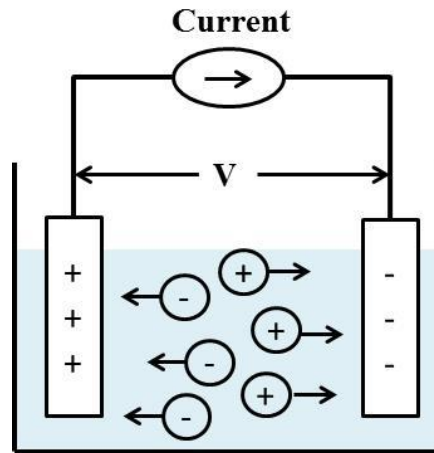


Figure 2-11: Schematic illustration of ions migration in a solution due to the electricity

The water conductivity is measured using considered sensor by injecting an AC current I to the outer two electrodes. Thus, the electricity passes through the water and two inner voltage electrodes determine the voltage drop V hence the resistivity of the water after calibration (see details in section 2.6.1). The reciprocal value of this resistivity gives the corresponding conductivity. A schematic diagram of the sensor's electrodes is presented in Figure 2-12 below in case of a 4-probe terminal configuration.

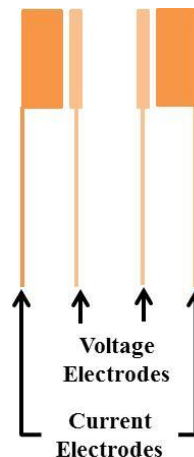


Figure 2-12: Current and voltage electrodes of the conductivity sensor

Based on the detection mode, the conductivity sensor can be categorized into two categories- contact mode and contactless mode⁵⁰. In contact mode, the electrodes are directly in contact with water and in the contactless mode, the electrodes are isolated from the water with a thin coating layer of few nanometers

made of a high dielectric permittivity material. This coating layer works against the oxidation of the electrodes and biofouling during the continuous measurement under the water. Thus, this thin coating layer enhances the lifetime of the sensor.⁵¹

Three different versions of the conductivity sensors were fabricated, where they differ according to their electrode dimensions. The electrodes were realized with different dimensions (taking into account the parameters L and S in the above equations and also some edge effects) in order to study their impact on the sensors' sensitivity.

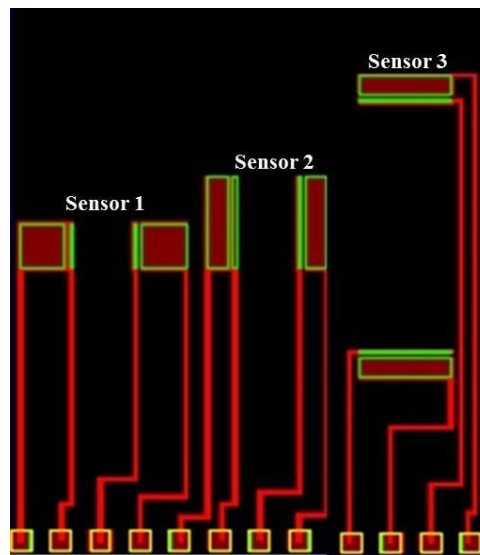


Figure 2-13: Different versions of the conductivity sensor

Figure 2-13 reports the schematic diagram of the different conductivity sensors. In these three versions, the sensors can be distinguished according to the electrode shape and arrangement (mainly surface area S and electrode spacing L). From the same figure, it can be observed that the sensors 1 and 2 have square and rectangular voltage electrodes respectively and their current electrodes have similar height according to their adjacent voltage electrodes. Sensors 2 and 3 have identical voltage and current electrodes, but their placing manner and spacing is different. Before providing the dimensions of the sensors' electrodes, a set of nomenclatures (different from the above parameters S and L) are provided below for better comprehension.

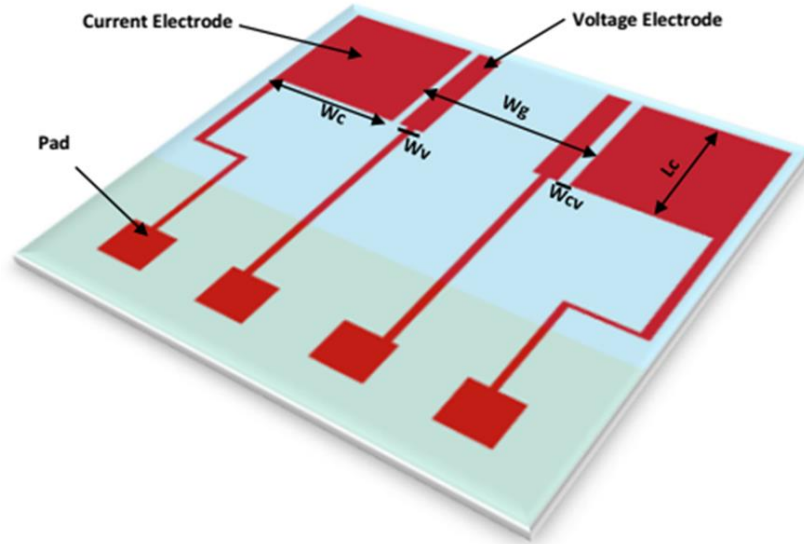


Figure 2-14: Different parts of the conductivity sensor electrodes labelled with nomenclature

Here,

W_c = width of the current electrode

W_v = width of the voltage electrode

W_{gv} = gap width between two voltage electrodes

W_{gc} = gap width between two current electrodes

W_{cv} = gap width between the current and voltage electrode

L_c = length/height of the current electrode

* $L_c = L_v$; L_v = length/height of the voltage electrode

Dimensions of the labelled parts in the Figure 2-14 are reported in Table 2-1.

Table 2-1: Dimensions of the different parts of conductivity sensor electrodes

| Sensor | W_c (μm) | W_v (μm) | * L_c (μm) | W_{gc} (μm) | W_{gv} (μm) | W_{cv} (μm) |
|--------|-------------------------|----------------------------|---------------------------|-------------------------------|-------------------------------|-------------------------------|
| 1 | 500 | 50 | 500 | 800 | 640 | 30 |
| 2 | 250 | 50 | 1000 | 800 | 640 | 30 |
| 3 | 250 | 50 | 1000 | 3000 | 2840 | 30 |

2.7.3 Experimental setup

The realized conductivity sensor was characterized by different reference conductivity solutions. The reference solutions were prepared using a commercial portable conductivity meter named Mettler Toledo FG3 FiveGo. Five solutions of different conductivity levels ranging from $\sim 500 \mu\text{S}/\text{cm}$ to $2500 \mu\text{S}/\text{cm}$ with a step of nearly $500 \mu\text{S}/\text{cm}$ were prepared. The preparation of the conductivity solutions was involved in adding salt to distilled water and then measuring the resulting conductivity using the reference conductivity sensor Mettler Toledo FG3 FiveGo, which was previously calibrated using a set of calibration standards. For the purpose of preparing the different solutions, distilled water was taken in a small glass beaker and different conductivity solutions were obtained by varying the amount of dissolved salt. The sensor was connected to the voltage data reading electronic circuit using the particular PCB and the reading circuit was connected to the computer through the NI DAQ system. In this experimental setup, NI DAQ system not only uses for voltage (V) data acquisition, but also it generates the required AC current supply (I) for the 4-probe sensor. LabView software interface was used to control the power supply from the DAQ board and visualize the input-output of the sensor. The simple reading circuit was used, which includes an $82 \text{ k}\Omega$ serial resistor and a fixed 100 mV amplitude AC power supply from the DAQ board for the purpose of generating the current (I) whose fixed amplitude is estimated to $1.22 \mu\text{A}$. Note that the frequency of this AC current is tunable as there is an optimal frequency range for proper operation as illustrated below. The photo of the experimental setup is demonstrated in Figure 2-15.

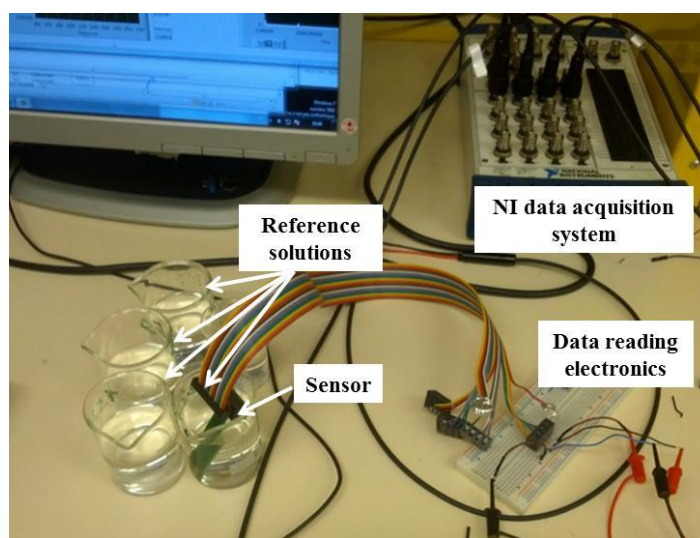


Figure 2-15: Conductivity sensor experimental setup. The sensor is submerged under a solution. There are five beakers with different conductivity solutions. The input-output of the sensor is connected to the NI DAQ board for supplying the power and reading the measured data.

2.7.4 Results and Discussion

In section 2.7.2 three different configurations (Figure 2-13) of the conductivity sensor were illustrated. The experiments were conducted with these three devices within the mentioned conductivity range (from $\sim 500 \mu\text{S/cm}$ to $\sim 2500 \mu\text{S/cm}$) at different AC supply frequencies. The AC power supply was chosen in order to avoid the electro-erosion and redox of the electrodes and the optimum operating frequency range was determined after behavioural modelling (See Annex 2).

The supply source frequencies were 5 kHz, 10 kHz and 15 kHz while determining the sensors responses' in terms of different reference solutions. These three frequencies were determined from the frequency sweep analysis. In this case, the sensor was submerged under a specific reference solution and the frequency of the supply source was varied from 30 Hz to 49 kHz. The extracted response expresses the operating frequency range for linear operation of the corresponding sensor. The comparison between the sensors was studied in different perspectives like- the linearity with respect to the reference conductivity solution, coated ALD material, with/without ALD layer.

In Figure 2-16, the frequency sweep analysis of the three versions of the conductivity sensors is presented. The notations S1, S2 and S3 stand for sensor 1, sensor 2 and sensor 3 respectively.

For each sensor type, the responses were measured with respect to the five reference solutions within the above-mentioned frequency range. A monotonous trend under a certain frequency range for a specific sensor represents the linear operating frequency of the corresponding sensor. In Figure 2-16(a), the first version of the conductivity sensor with square-shaped electrodes shows irregular responses within the whole velocity range for each reference solutions. These results denote that the conductivity sensor S1 will exhibit almost no linear sensitivity for measuring the conductivity within this frequency range, probably due to the square shape of its electrodes, leading to excessive border effects. On the contrary, the subsequent two versions S2 and S3 (Figure 2-16 (b) and (c)) - both with rectangular electrodes, show uniform horizontal response under a certain frequency range starting after 200 Hz to until 10 kHz. This frequency range can be referred to as the linear operating frequency range and the gap magnitudes between the different conductivity solutions indicate the sensor's sensitivity to different conductivity level.

Based on the frequency sweep experiments results, the considered three sensors were operated at 5 kHz, then 10 kHz and then 15 kHz. For each frequency, the sensor was submerged under the five solutions in a successive manner and the measured data were recorded. For each time, 20 measurements were performed in order to determine the uncertainties. The obtained results are presented in Figure 2-17 below.

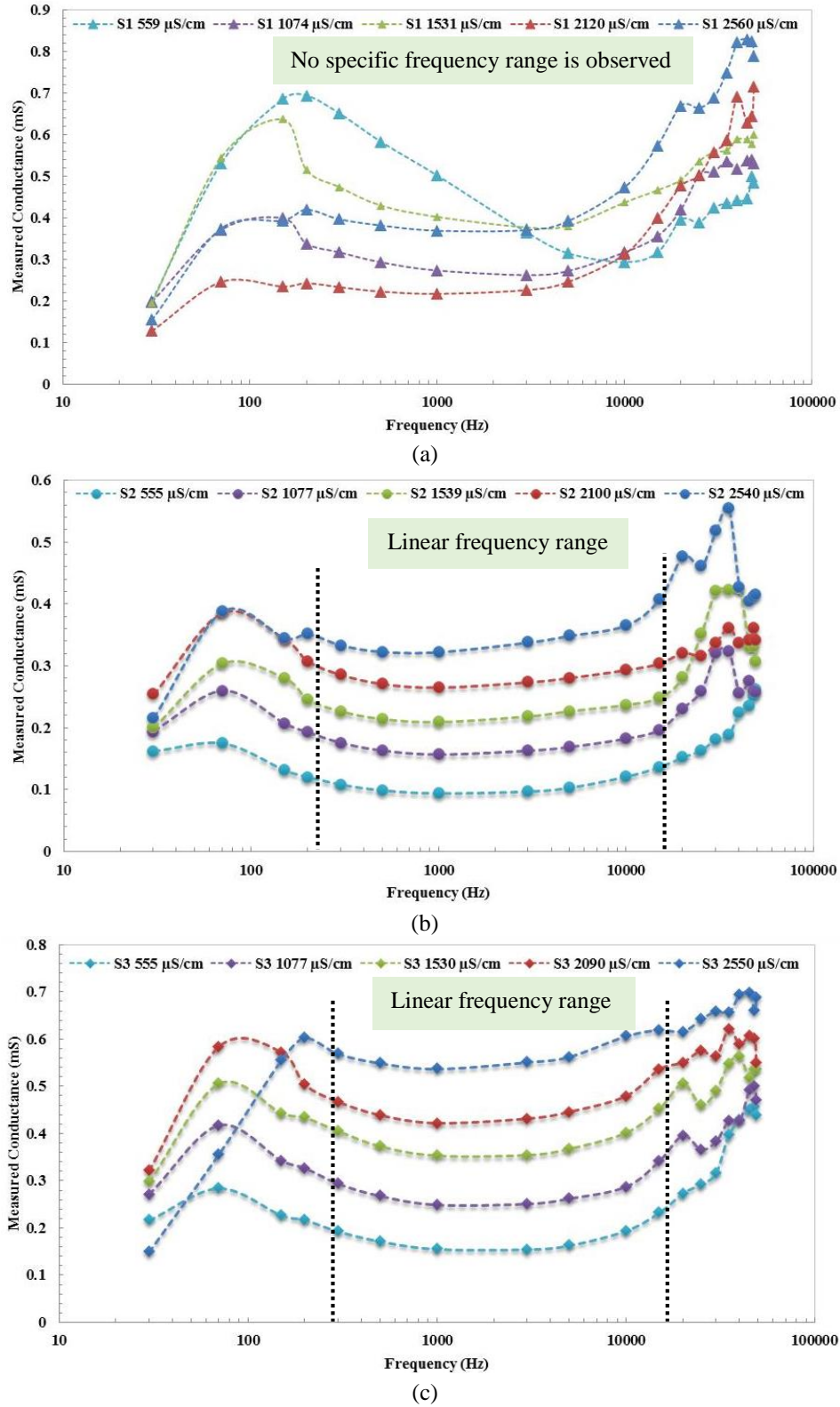


Figure 2-16: Responses of the three sensors in frequency sweep analysis (a) sensor 1, (b) sensor 2 and (c) sensor 3 under the frequency range $\sim 500 \mu\text{S}/\text{cm}$ to $\sim 2500 \mu\text{S}/\text{cm}$.

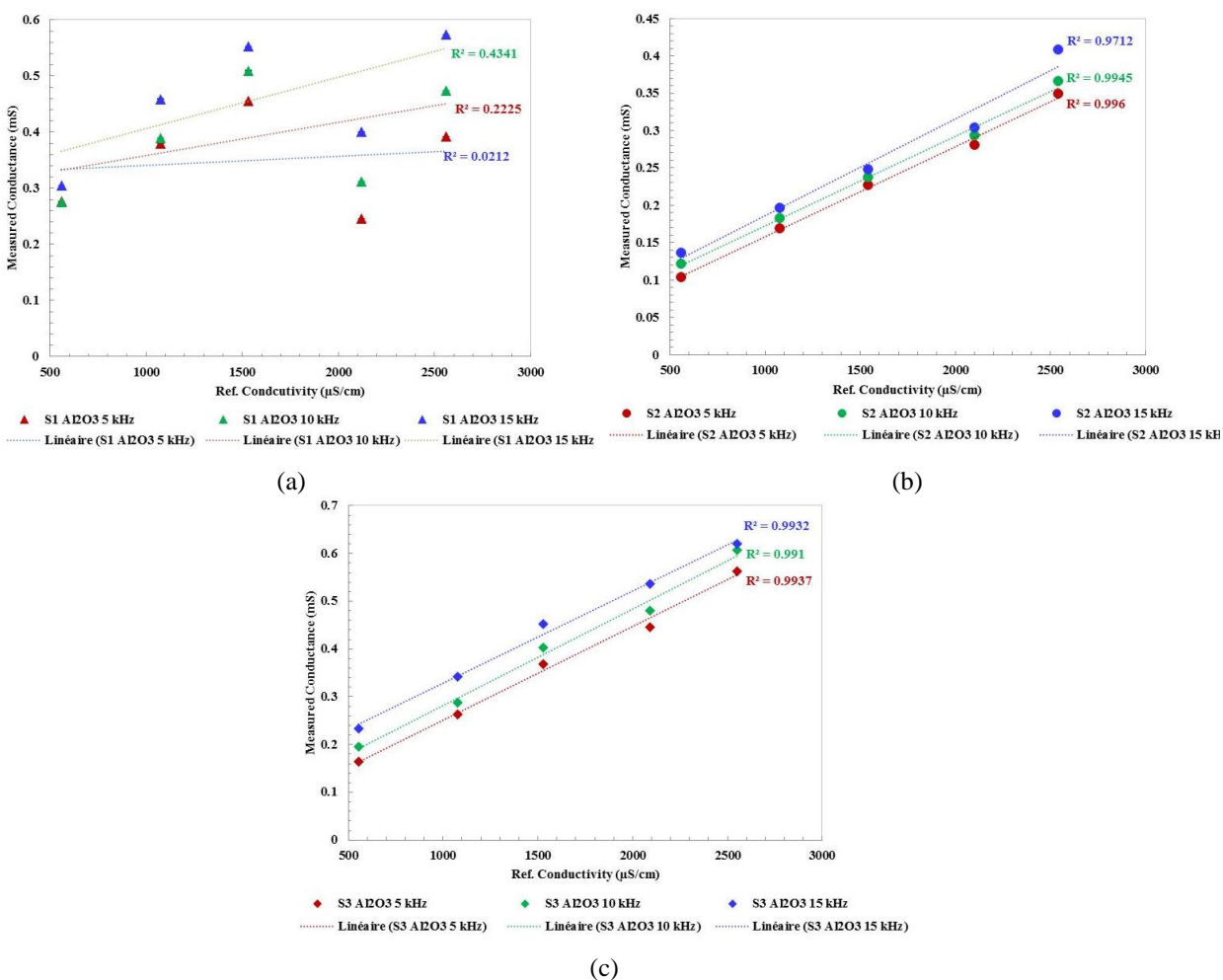


Figure 2-17: The response of the S1, S2 and S3 sensors under the considered five conductivity solutions at 5 kHz, 10 kHz and 15 kHz supply frequencies. Error bars are added in the plots, but not visible due to the small uncertainties.

It can be seen from the above figure that the sensor S1 exhibits a completely inconsistent response to different conductivity solutions under the three frequencies. On the other hand, the fitted regression values for the sensors S2 and S3 indicate excellent linearity within the whole conductivity range for the three operating power supply frequencies. From Figure 2-17(a), it obvious that the S1 cannot be used to determine the conductivity of a sample. Therefore, this version will be skipped in the forthcoming discussion. Hence, the sensors S2 and S3 express almost similar sensitivity under identical condition; so for comparison sake *i.e.*, in terms of the ALD coating layer, sensor S2 will be considered. Indeed, there is no specific physical structure difference besides the electrodes arrangement between these two sensors.

The presented results in Figure 2-17 are involved with the silicon-based device coated using ALD with Al_2O_3 . In order to investigate the impact of the ALD layer on the sensor's sensitivity, the obtained response

of S2 with ALD was compared with the same device response that was fabricated without ALD coating. The comparison plot is showed in the figure below.

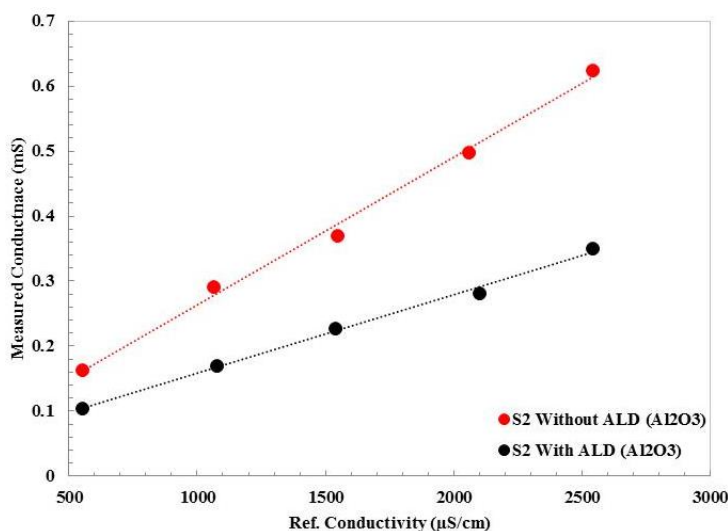
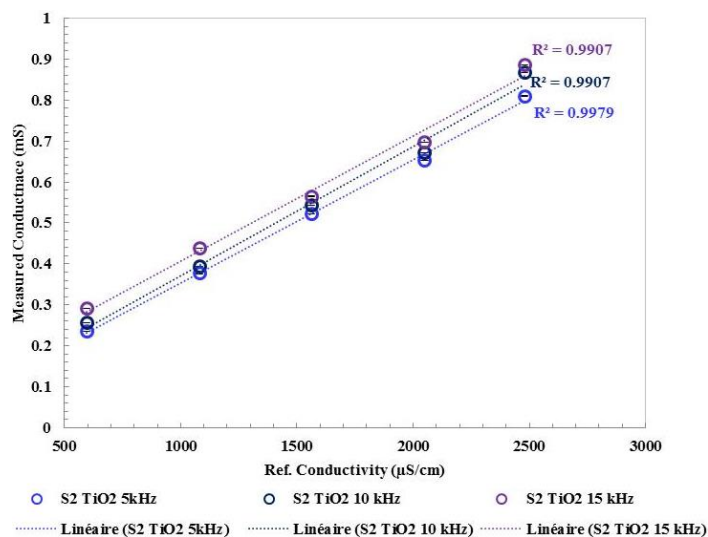


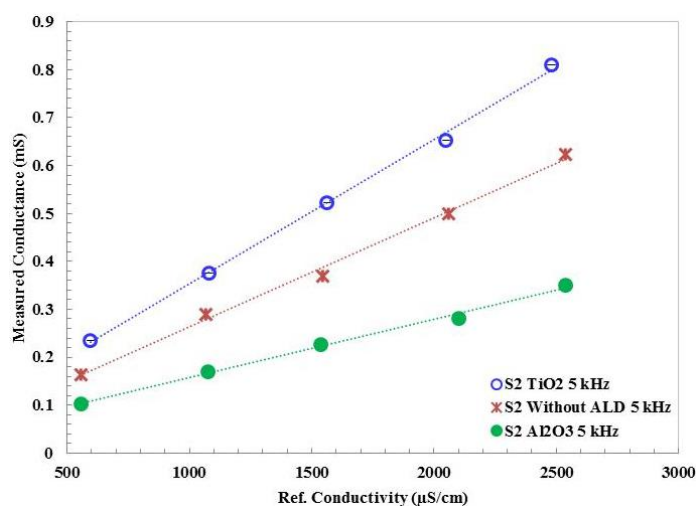
Figure 2-18: Conductivity sensor response at 5 kHz with and without coating layer made of Al_2O_3

Here it can be observed from the plot (Figure 2-18) that, the coating layer reduces the sensor's sensitivity. Under at a certain frequency which is 5 kHz here in this case, the magnitude of the sensor's response decreases gradually as the magnitude of the reference conductivity increases. The apparent measured conductance is around 0.62 mS at the maximum conductivity when there is no ALD layer on the sensor. Hence, under a similar situation, the magnitude of the measured conductance obtained by the same device is decreased to 43.55 % of the previous value at the maximum reference conductivity with ALD layer. Indeed, the sensor will be implemented in the water distribution network; therefore, there is a high possibility of biofouling generation for a long run implementation. So, the ALD coating layer is potentially important to protect the sensor from the biofouling hence increase the lifetime of the device. But definitely, this will be at the expense of a reduced sensitivity, which was expected due to the serial impedance introduced by the ALD coating.

In order to distinguish the most favourable ALD coating material, another prototype of the same device was coated by TiO_2 with same thickness (10nm). The extracted responses of the device at different frequencies and the comparative results of this device with the others (Al_2O_3 and without ALD) are reported in Figure 2-19.



(a)



(b)

Figure 2-19: (a) The measured response of the S2 sensor with TiO₂ ALD layer at 5 kHz, 10 kHz and 15 kHz and (b) comparison among the measured response of the same sensor with TiO₂, Al₂O₃ ALD layer and without ALD layer.

The conductivity sensor S2 with TiO₂ ALD layer also exhibits higher sensitivity with respect to the reference solutions under the three operating frequencies. The coefficients of the determination from Figure 2-19(a) denote that the sensor S2 has higher sensitivity with TiO₂ ALD layer. From Figure 2-19(b), it can be observed that the TiO₂ ALD layer discloses the higher sensitivity than the ALD layer Al₂O₃ even better than the device without ALD, which is an astonishing result, not yet understood. The measured data of the

device without ALD shows an intermediate response between the TiO₂ and Al₂O₃ ALD layer. Therefore, either S2 or S3 can be determined as the final version of the conductivity sensor with TiO₂ ALD coating layer.

2.7.5 Evaluation of Antifouling Properties of Al₂O₃ / TiO₂ ALD-coatings

In order to evaluate the effectiveness of the ALD coating layer in terms of anti-fouling, real field tests were conducted with the sensor chips incorporation with the collaborator SMAS from Portugal. ALD has the main advantages of (i) conformal deposition, hence ensuring that all the surface of the sensitive parts of the multi-parameter sensor chip is properly covered by the coating material (ii) the thickness can be atomic up to a few tens of nanometer, hence not introducing significant electrical perturbations to the sensor's operation. The material TiO₂ was selected for its well-known photocatalytic properties, which can help to deteriorate any organic material that accumulates to the surface. Al₂O₃ was also found in the literature as a potentially good candidate for an antifouling coating. For the test, the samples with TiO₂ at 10 and 30 nm thickness and Al₂O₃ at 10 nm thickness were considered. Tests were conducted with different water like- wastewater, treated drinking water and raw water.

The testing protocol was established to compare the growth of biofilm on the surface of different types of toppings of the sensor node, being used as a reference board with no cover, and three others with alumina (10 nm) and titanium oxide (10 to 30 nm). The table below summarizes chip characteristics:

Table 2-2: Different versions of the conductivity sensor with different ALD coating material and thickness layer.

| chip version | ALD | thickness (nm) | Quantity | Comments |
|--------------|--------------------------------|----------------|----------|-------------------------|
| 1 | Al ₂ O ₃ | 10 | 2 | |
| 2 | TiO ₂ | 30 | 2 | |
| 3 | TiO ₂ | 10 | 2 | |
| 4 | nothing | 0 | 3 | SiO ₂ ,400nm |

In order to replicate the real scenario, a few dummy PVC tubes were prepared with a flat head similar to the sensor node for mounting the sensor chip. The chip was attached to the PVC head by epoxy resin. Prior to this, the chip was cleaned with IPA solvent. The considered four chips were attached to the PVC head and afterwards, the PCV tube along with chips was put inside the oven at 65 °C to ensure the proper adhesion.

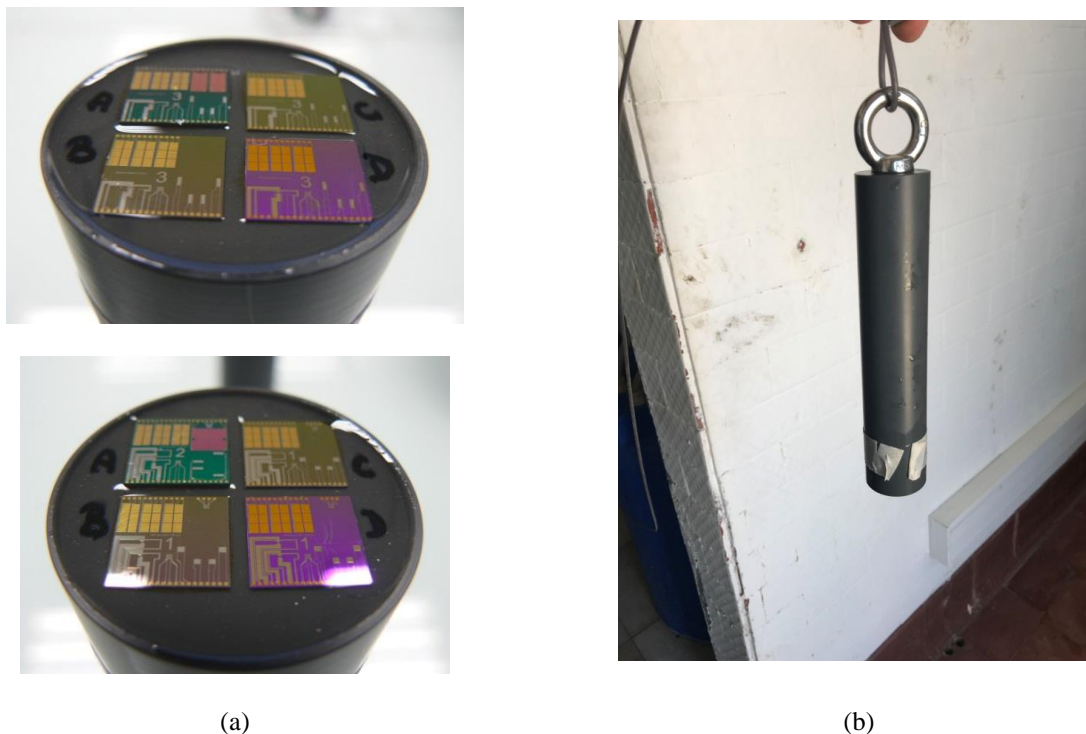


Figure 2-20: (a) Two prepared PVC tubes for the test where the sensor chips are mounted on their head, after oven dried at 65 °C, each tube contains four chip denoted by A, B, C and D. No ALD coating on-chip A, chip B is coated by Al_2O_3 with 10 nm thickness and chip C and D are coated by TiO_2 with 10 and 30 nm layer thicknesses respectively. (b) The prepared prototype for the field test.

Luminometer EnSure (model V.2, Hygiena, US) was used for measuring the growth of biofouling on the surface of the chip. Compatible calibration probe was used along with the device and ATP swab used for collecting the samples from the sensor chip (See Annex 3).

Test in Wastewater

The tests were mainly aiming at evaluating the capability of the sensor to continue to carry out measurements in residual water, considering that there should be a rapid deposition of substances on the surface of the device, preventing it from effective readings. Obtained results under the wastewater environment are reported in the table below.

From the obtained results, it can be observed that whatever the coating on the sensor chips, in such wastewater conditions, the deposit quickly covers the entire testing device. This first result with dummy sensor chips highlights the difficulty of measurement with microsystems in wastewater. It can be also seen from the data that there are no significant differences observed when comparing the devices that have the anti-fouling coating with those that did not have such a coating.

Therefore, the sensor chips are subjected to biofouling in wastewater and that a nanometric thickness of either TiO₂ or Al₂O₃ is not efficient enough to prevent biofouling, or even may increase biofouling.

Table 2-3: Anti-biofouling test results under wastewater medium.

| Date | A no ALD (RLU) | B Al ₂ O ₃ 10 nm (RLU) | C TiO ₂ 30 nm (RLU) | D TiO ₂ 10 nm (RLU) | Comments |
|------------------|----------------------|--|--------------------------------------|--------------------------------------|---|
| 29/3/17 17:00 | 0 | 0 | 0 | 0 | Fully cleaned before employment in the wastewater |
| 30/3/17 10:30 | 7832 | 7324 | 7130 | 7579 | After 1 day |
| 30/3/17 11:00 | 0 | 0 | 0 | 0 | Fully cleaned before employment in the wastewater |
| 3/4/17 10:45 | 3055 | 6747 | 5508 | 7648 | After 3 days |
| 3/4/17 11:30 | 0 | 0 | 0 | 0 | Fully cleaned before employment in the wastewater |
| 28/7/17 15:00 | countless | countless | countless | countless | After 3 months |

Test in Drinking water (treated and raw)

This test aims at testing for biofilm growth and limestone incrustation, depending on whether water with biocide (hypochlorinated acid) or water still without a sanitary barrier is considered.

The test results undertreated and raw drinking water condition show inconsiderable growth of deposit. For the maximum test duration (173 days) only the sensor chip with TiO₂ 30nm thick ALD exceeds 100 RUL and rest of the cases it exhibits only 2 orders of magnitude.

Hence, for both the cases, no significant biofouling is observed in comparison with the case of wastewater. Therefore, there is no need for an anti-fouling protection layer at least for periods up to 6 months (173 days). Moreover, the reported results in Table 2-2 and 2-3 suggest that the addition of coating has no added value, or may even detrimental in comparison with the pure SiO₂ surface.

Table 2-4: Anti-biofouling test of the considered devices under treated drinking water environment.

| Date | A no ALD (RUL) | B Al ₂ O ₃ 10 nm (RUL) | C TiO ₂ 30 nm (RUL) | D TiO ₂ 10 nm (RUL) | Comments |
|------------------|----------------------|--|--------------------------------------|--------------------------------------|--|
| 3/4/17 16:00 | 0 | 0 | 0 | 0 | Fully cleaned before employment in water |
| 5/4/17 14:45 | 25 | 36 | 30 | 17 | 2 days, with free chlorine > 0.5 mg/L |
| 5/4/17 15:00 | 0 | 0 | 0 | 0 | Fully cleaned before employment in water |
| 20/4/17 9:45 | 0 | 0 | 1 | 55 | 15 days, with free chlorine > 0.5 mg/L |
| 20/4/17 10:30 | 0 | 0 | 0 | 0 | Fully cleaned before employment in water |
| 5/5/17 9:45 | 0 | 0 | 2 | 2 | 15 days, with free chlorine > 0.5 mg/L |
| 5/5/17 10:30 | 0 | 0 | 0 | 0 | Fully cleaned before employment in water |
| 28/7/17 15:00 | 11 | 24 | 130 | 82 | 84 days, with free chlorine > 0.5 mg/L |

Table 2-5: Anti-fouling test under raw drinking water

| Date | A no ALD (RUL) | B Al ₂ O ₃ 10 nm (RUL) | C TiO ₂ 30 nm (RUL) | D TiO ₂ 10 nm (RUL) | Comments |
|---------------|----------------------|--|--------------------------------------|--------------------------------------|--|
| 28/7/17 16:00 | 0 | 0 | 0 | 0 | Fully cleaned before employment in water |
| 17/1/18 15:20 | 60 | 91 | 70 | 88 | 173 days without free chlorine |

2.8 Conclusion

The detailed physical description of the considered MPSC has been reported in this chapter. Different sensing elements of the multi-sensing device and their corresponding fabrication steps are discussed elaborately. A comprehensive pictorial illustration of the fabrication procedures involved in creating multiple resistive sensing devices on a single chip has also been demonstrated. Unification of different micro-sensors on the same chip is a challenging task in the perspective of manufacturing technology and the transduction fundamentals of each sensing component. Identical working principle (resistance variation) facilitates the coexistence of the assorted sensors. On the other hand, geometric optimization allows the co-integration of several realized sensors without degrading their performance. Prior to obtaining effectively functional co-integrated prototype of the multi-parameter sensor chip; several steps have been performed associated with the physical structure modification. The sensor that has been realized to determine the water pressure strongly influenced the co-integration issue. As a consequence, it has been included in this part with preliminarily obtained experimental measurements. The conductivity sensor has been introduced afterwards, where the different versions of the sensor were highlighted with their corporeal description and the measured responses under different operation conditions. The remaining sensors (flow-rate and temperature) will be discussed in the subsequent chapters comprehensively. They are sorted based on their operation principle since both of them are realized based on thermal transduction. The similarity of the flow-rate and the temperature sensor lies in their sensing elements. We have to carefully elaborate on those two sensors since thermal effects are involved in both with potentially critical impacts on the whole constituents of the MPSC. A thin-film resistor is used to determine two different parameters- water flow and temperature. Therefore, before introducing these two sensors, a chapter (Chapter 3) is dedicated to Resistance Temperature Devices (RTD), where the diverse use of a resistive element has been emphasized.

Part II: Multi-Parameter Sensing Chip

thermal sensors

3 Chapter 3: Electrical resistance as a key building block for measurement of temperature and related water parameters

3.1 Introduction

Temperature is among the most commonly measured parameters, whatever the medium. Precise and localized temperature measurement is required for thermal monitoring and processes control⁵². It is worth mentioning that *temperature measurement is performed not only to extract the temperature as an intrinsic environmental parameter, but also to have a better accuracy on other temperature-dependent parameters*. Indeed, a large variety of physical parameters depend on temperature and they require very often a correction, based on the value of temperature. This is true in particular for all water parameters considered in this work on multi-parameter water sensing probe, namely: pressure, conductivity, flow-rate and concentration of the various chemical contents.

Besides their primary function of giving information on the actual temperature, it appears that *temperature sensors are also important building blocks in many other kinds of sensors*. They indirectly give access to many other parameters. Among others, they are used in Pirani gages for vacuum measurement, in bolometers for infrared radiation energy measurement and in flow-rate sensors based on convective heat transfer. All those indirect measurement schemes involve heat transfer mechanisms. Therefore, based on what precedes temperature sensors appear as important, multi-purpose building blocks. Accordingly, a water temperature sensor is included in the MPSC to determine the temperature of water, which also enables accounting for other parameters temperature dependence. Furthermore, such temperature sensor will also serve as the basis of the architecture of a flow-rate sensor as described in chapter 4.

In this chapter, thermometry and its fundamental principles will be reviewed first along with different temperature measurement techniques. A special attention will be paid to temperature measurement based on resistive elements: Resistance Temperature Detectors (RTD), Thermistors and Thermocouples. The manifold applications of a thin-film RTD are also reported here; where it has been shown how fascinating can be the use of a simple resistor, as it can be employed for different applications with a simple modification in its operation scheme. The chapter will be ended with a discussion on temperature sensor used as a part of the MPSC to measure water temperature.

3.2 Water temperature variations and its impacts

3.2.1 Natural and anthropogenic factors impacting water temperature

In the case of natural water source or water networks, water temperature is affected by both natural causes, which include *Sunlight, Turbidity, Atmosphere* and *Confluence*. It is also affected by anthropogenic factors, such as *Impoundments, Deforestation* and *Thermal pollution*.

Sunlight is the main source of heat which increases water temperature of different natural sources *i.e.*, river, ocean, pond, lake. Sunlight easily increases water temperature since water has very low albedoⁱⁱⁱ 53. Therefore, high absorption of solar energy leads to the rapid temperature increase of water. Hence, the temperature of a waterbody varies daily depending on the amount of absorbed sunlight. Among the different layers of the water in a source, the light only passes through the photic zone^{iv}. Generally, the depth of the photic zone depends on the presence of solid and other light-scattering elements in water. For instance, an ocean can have a 200 m deep photic zone 54. Almost more than half of sunlight is absorbed by the first 2 meter of water 45. As a consequence, the superficial bodies of water become warm faster than the deeper parts.

Turbidity- The amount of suspended solid particles in water is known as turbidity and it has an impact on the water temperature as well. Heat absorption capacity of the solid particles is higher than the water and the absorbed heat is then directly transferred from the floating particles to the water 41. So, turbid water tends to warm rapidly compared to pure water.

Atmosphere- atmospheric temperature also plays a role to alter the temperature of the natural water sources and reservoirs. If the surrounding air temperature is higher than the water, then heat will be transferred to water. On the other hand, water will lose heat and become colder if the adjacent air temperature is lower than the water. In this case, the heat transfer depends on the thermal inertia and on the specific heat of the water 45.

Among these three anthropogenic factors, impoundments and deforestation do not cause significant water contamination. Instead, these two phenomena have a role in water temperature variation of natural sources that affect the local aquatic life. In some cases, the dam without flow controlling sliding gate may increase the downstream water temperature. Further, the unusual release of hot and cold water from the dam also affect the normal temperature of the corresponding aqua environment 55. On the other hand, plant shadow protects the water surface from direct sunlight that prevents the water become hot. Deforestation

ⁱⁱⁱ The term Albedo refers the ability of a surface to reflect incident solar light mainly by diffuse reflection.

^{iv} Light reaching zone or the uppermost surface of the river or lake which expose to the intense sunlight.

increases the temperature of the pond, lake in the forest region ^{45,56}. Hence, impoundments and deforestation hinder the spawning and hatching process. Besides, thermal pollution has a significant effect on water quality. The river or water ducts close to the residential or industrial area are often confronted with thermal pollutants that increase the temperature of those waterbodies. The sudden change in the water temperature reduces the amount of dissolved oxygen and aquatic animal *i.e.*, fish ^{45,56}.

3.2.2 The impact of water temperature on other parameters governing water quality

Temperature is one of the governing parameters that should be considered prior to evaluating water quality since several physical and chemical water properties strongly depend on temperature. A small alteration of water temperature may bring a significant variation of its normal characteristics. Figure 3-1 below illustrates the main properties of water that are related by temperature. More details on those relations are given in what follows.

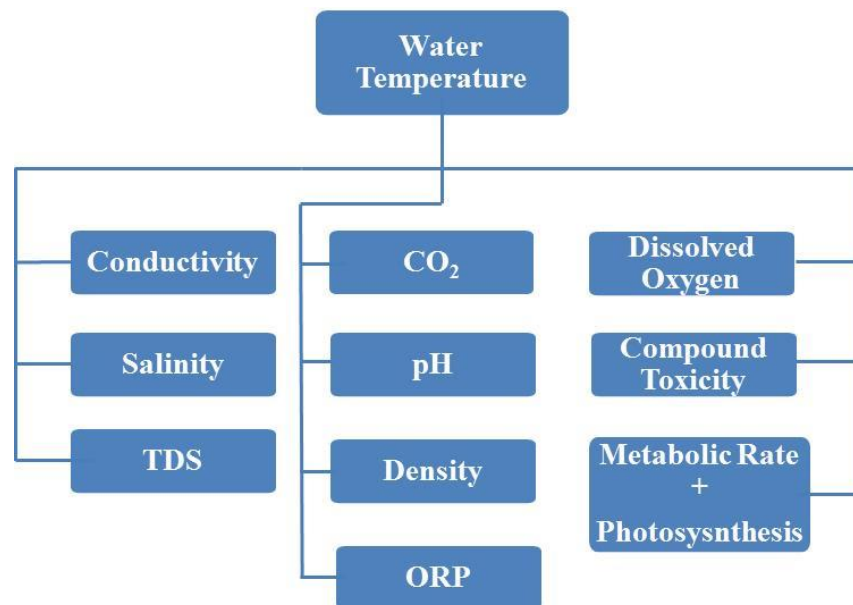


Figure 3-1: Main water quality parameters that are affected by the water temperature (TDS: Total Dissolved Solids, ORP: Oxidation Reduction Potential).

Water electric conductivity and Water Temperature: Conductivity depends on the concentration, charge and mobility of ions. Ions' mobility depends on the viscosity of the corresponding liquid ⁵⁷. In a high viscosity liquid, ions mobility is very low. Besides, viscosity is temperature dependent. More specifically, it is inversely related to temperature. As temperature increases, viscosity decreases. As a result, ions mobility increases. Hence, a high water temperature will induce a high electric conductivity in comparison to standard conditions due to the variation of viscosity ⁴². In general, a 1 °C increase in temperature induces an electric conductivity increase by 2 ~ 3 %, and 5 % in the specific case of pure water ⁴².

Total Dissolved Solids (TDS) and Water Temperature: TDS refers to the number of solutes smaller than 2 microns dissolved in a solution ^{41,58}. It is also related to electrical conductivity of the water solution. Since conductivity depends on temperature, TDS is also temperature-dependent. Since high temperature enhances the solubility of different salts ⁵⁹, as a consequence, when salts are dissolved, they decompose as ions. Therefore, hot water is likely to have higher ionic concentration than cold water. Hence, TDS is affected by temperature, and the latter effect has a second-order impact on conductivity as well.

pH and Water Temperature: pH indicates the concentration of H⁺ ions in a solution or water, which is an indication about the acidity or basicity of the solution. pH is temperature dependent since the formation of hydrogen ions from water is an endothermic process:



Dissolved Oxygen (DO) and Water Temperature: the presence of dissolved oxygen and other gases depend on the corresponding water temperature. The solubility of Oxygen varies inversely to temperature ⁵⁵. Cold water contains more Oxygen than hot water. If water temperature is significantly high, then local aquatic life suffers from low Oxygen; and longtime insufficient Oxygen may lead to its extinction.

Compound Toxicity and Water Temperature: Temperature alteration can change the water toxicity level also. As it was discussed above that the solubility of the present elements increases with the increase of temperature. So, some heavy metals such as- Zn, Pb, Cd and compound like ammonia (NH₃) dissolved in the water at a high temperature which increases the toxicity of the water ^{60,61}. Temperature above 25 °C significantly increases the mortality rate for Zn in comparison with a temperature less than 20 °C ⁶⁰. At high pH level, NH₃ becomes toxic; but high temperature can modify the intense and chronic criteria concentrations as well ⁶².



At neutral pH, the above chemical reaction remains shifted to the left, but for every 10 °C increase in temperature the ration of unionized ammonia to ammonium become two times higher ⁶². Water temperature not only responsible for increasing the toxicity, it decreases the tolerance margin of the local aquatic entities ⁶⁰. Since, high water temperature enforces the Oxygen consumption, metabolic rate and tissue permeability ⁶⁰.

Oxidation Reduction Potential (ORP) and Water Temperature: The ORP of a solution also depends on temperature. Indeed, the solution temperature has an impact on chemical species *i.e.*, atoms, molecules and

ions that exist in the solution which alter the ORP value ⁶³. Therefore, temperature reading should be recorded and considered while measuring and analyzing the ORP data of a water body.

Density and Water Temperature: There is a direct relationship between temperature and the water density. The density of pure water reduced to around 9% when it becomes ice ⁶⁴. As a consequence, ice can float on the water. The pure water obtains its maximum density (1 g/ml) at 4 °C ⁶⁴, so water with temperature other than 4 °C including the super-hot or super-cold water will float on the water with 4 °C. Density is an intrinsic property of the water and it can be related to its temperature based on the water types such as- *Freshwater, Saltwater, Ice*.

Metabolic Rate and Photosynthesis and Water Temperature: The metabolic rates and the biological activities of aquatic organisms are directly related to water temperature ⁴⁵. This happens since the activeness of different cellular enzymes increases at high temperature ⁶⁵. Indeed, the local temperature variation of a water body influences the habitation of aquatic life. Some fishes *i.e.*, Trout, Salmon are comfortable with the colder environment, on the other hand, some aquatic plants prefer warm temperature to flourish ⁴¹. For most of the fish, their physiological function rate becomes double to 10 °C increase in temperature ⁶⁶. Plant respiration and photosynthesis also depend on the temperature ⁴⁵. Different species of trees required a different level of temperature for favourable photosynthesis activity. Any deviation of the standard temperature value can enhance or diminish the photosynthesis rate.

3.3 Fundamentals on temperature and its measurement

3.3.1 Basics on temperature

Temperature is a physical quantity which provides objective information at the macroscopic scale, about how “hot” or “cold” an object or a medium is. It has close relations with heat, which is a form of energy related to the microscopic motion or vibration energy of the molecules or the particles in a substance. Upon heating, particles gain higher energy and move faster in a fluid medium or vibrate vigorously in a solid medium. In a closed system, temperature is increased when the system gains heat from its surroundings. Temperature can be seen as an indicator of the microscopic kinetic energy of particles inside a system. At non-zero absolute temperature, and from a microscopic point of view, particles are continuously moving. All particles do not have the same velocity and direction. Measuring temperature actually provides information on those particles average kinetic energy. A high temperature is equivalent to a fast average movement of the particles in the system.

Temperature is also related to the potential of *heat transfer* between two objects by different means like- conduction, convection and radiation. A temperature difference between two objects leads to a heat flow in

the manner a potential difference at the two terminals of a conductor leads to a current flow. According to the second principle of thermodynamics, heat always flows from the hot body to the cold one. Heat flow continues till the two bodies eventually reach the same temperature which is known as thermal equilibrium. This thermal equilibrium concept is used when measuring temperature by a thermometer. In general, to measure the temperature of an object, a thermometer is placed in contact with it. The system composed of the thermometer and the considered body reaches thermal equilibrium after certain duration. Under these conditions, the temperature read on the thermometer is equal to the object temperature.

The most commonly used scale for temperature measurement is Centigrade or Celsius scale ⁶⁷. This Celsius unit system is proposed based on the fundamental temperature interval of 100 degrees, from the melting point of ice to the boiling point of water under standard atmospheric pressure. The symbol of this Centigrade unit is ‘°C’. There is another temperature scale called Fahrenheit (symbol: °F) which was named after a physicist Daniel Gabriel Fahrenheit and invented before the Celsius scale. In Fahrenheit scale, the lowest temperature point is defined as 0 °F by taking as reference the temperature of the brine solution. At present, the Fahrenheit scale range is defined by two fixed temperature points- melting point of ice and boiling point of water under standard atmospheric pressure at sea level corresponding to 32 °F and 212 °F, respectively. In the case of physical science, another temperature scale is used, the Kelvin scale, named after its inventor, Lord Kelvin. Kelvin scale is known as absolute temperature scale. It is defined by ascribing the value 273.16 K to the triple point of the water. According to the definition of the Kelvin scale, the absolute zero or 0 K is equal to -273.15 °C and -459.67 °F ⁶⁷⁻⁶⁹. This scale does not admit negative temperature values. This ultimate limit of 0 K also corresponds to the zero-level of thermally-induced molecular vibrations.

3.3.2 *Brief history of temperature measurement*

The history of thermometry is quite ancient. The first thermometry application was found by a Greek physician named Claudius Galenus (AD 129 - 200) ⁷⁰. He used temperature measurement for clinical purposes and the basis of his thermometry technique was based on Aristotle postulation on the four basic qualities: hot, cold, dry and wet ^{70,71}. Galenus proposed a standard neutral temperature point as well that can be made by mixing tantamount of ice and boiling water^{70,72}. More than thousand years after Galenus, in 1578, Hasler used thermometry to create a mixture of different drugs based on the Galenus concept. He wrote a medical book *De Logistica Medica* in which he explained his temperature measurement method. In the second century BC, Greek physicist and engineer Philo Mechanicus (BC 280 - BC 220) designed an instrument which demonstrates experimentally the expansion of air on heating, but the proposed device could not provide the temperature reading. ⁷⁰

A complete design description of a temperature measurement device was disclosed by Santorio in his paper Commentaries on Galen⁷⁰. Although Galileo is acquainted as the inventor of the thermometer, in reality, he is not. He proposed a device which is called a thermoscope^{70,73}. The advancement in temperature measurement devices has a long history and the current elevated form of those devices has been achieved by a lengthy evolution process.

Huge progress has been accomplished since those ages. Nowadays, temperature measurement methods can be divided into three types- **a.** Contact/Invasive, **b.** Semi-invasive and **c.** Non-contact/non-invasive temperature sensing⁷⁴.

Measurement process depends on different constraints such as the operation media and principle, temperature range, level of accuracy, measurement duration, cost, size and toughness. Existing methods of temperature measurement can be classified under the above mentioned three categories.

In this report, we will not elaborate on the numerous measurement techniques for temperature measurement. Instead we will concentrate on those techniques which are based on the use of an electrical resistance, since this is in line with our primary choice of having all sensors of the MPSC based on a resistive read-out. This is particularly sound as such kind of temperature sensor can also be re-used as the building block of other types of sensors involving heat transfer, as described in this section, with further detailed description in chapter 4 dealing specifically on flow-rate sensors.

3.3.3 *Electrical Resistance Devices*

Resistive temperature measurement is one of the most widely used processes for measuring the temperature at which a resistor is used as a temperature detector. The electrical resistance of a resistor depends on its physical temperature and this fundamental concept is used to operate numerous temperature detecting devices⁷⁴. For a specific metal, the electrical resistance generally depends on temperature. Therefore, it is very easy and convenient to use metallic resistors for temperature measurement by measuring the resistance value. However, several issues need to be considered prior to manufacturing such devices such as oxidation resistivity, cost, temperature coefficient resistance, and compatibility with the operation medium⁷⁴.

Different metals such as Gold, Platinum, Nickel, Silver, Titanium and Copper have been widely used to produce resistive thermometers^{75,76}. A great number of resistive temperature sensors are made of platinum. The temperature coefficient of resistance (TCR), defined as the relative change of resistance due to temperature variation ΔT , that is $TCR = (\Delta R/R_0)/\Delta T$, is the most important parameter when considering a material for a resistive temperature sensor. The higher the TCR value the higher the sensitivity of the

sensor. Platinum has a high TCR value and excellent linearity of its resistivity over a wide temperature range. Some other materials have higher TCR value than platinum (Pt), but none of them show high reproducibility and chemical stability at high temperature⁷⁷. Besides, this material has corrosion resistivity and outstanding accuracy with approximately one order of magnitude uncertainty⁷⁸⁻⁸¹. The value of the resistivity at ambient temperature and the TCR values of widely used materials are reported in Table 3-1.

Table 3-1: Resistivity at 20 °C and TCR value of different materials^{82,83}

| Material | Resistivity ($\Omega\cdot\text{m}$) | TCR ($10^{-4}/\text{K}$) |
|----------------|---------------------------------------|----------------------------|
| Aluminum (Al) | 2.69×10^{-8} | 42.0 |
| Copper (Cu) | 1.67×10^{-8} | 43.0 |
| Gold (Au) | 2.30×10^{-8} | 39.0 |
| Nickel (Ni) | 6.84×10^{-8} | 68.1 |
| Palladium (Pa) | 10.8×10^{-8} | 37.7 |
| Platinum (Pt) | 10.6×10^{-8} | 39.2 |
| Silver (Ag) | 1.63×10^{-8} | 41.0 |
| Tungsten (W) | 5.50×10^{-8} | 46.0 |
| Iron (Fe) | 9.71×10^{-8} | 65.1 |

The main electrical resistive temperature sensing devices are Resistive Temperature Detectors (RTD) and Thermistors. RTD is more significant than the thermistor in terms of this dissertation context. Indeed, two sensing elements: Flow-rate and Temperature of the MPSC have been fabricated based on RTD concept. Therefore, RTD will be reported explicitly after exploring different temperature measurement techniques; and thermistor is presented briefly in the following section.

3.3.3.1 Thermistor

The word ‘Thermistor’ comes from two words *Thermal* and *Resistor*. The thermistor is a resistor which can be used as temperature sensing device. It measures the temperature by measuring a resistance change due to a temperature variation. Different materials are used to fabricate thermistors like metallic compounds including oxides or single crystal semiconductors like Silicon, Germanium^{84,85}. Usually, a thermistor is made of non-metallic solid state materials. Two types of thermistors are available, depending on their temperature coefficient, which is an important parameter as it determines the working range and the sensitivity of the resulting sensors. The resistance value is related to temperature variation of a thermistor as follows:

$$\Delta R/R_0 = \alpha \Delta T \quad (3-3)$$

Here,

ΔR : resistance variation,

R_0 : initial resistance value,

α : first-order temperature coefficient of the resistance (TCR),

ΔT : temperature variation.

The temperature coefficient of a thermistor can be either positive or negative. Negative temperature coefficient thermistors are more common. In fact, the sign of α depends on the used material. In the case of a positive temperature coefficient, the resistance of a thermistor increases when the temperature increases. The opposite occurs in the case of a thermistor with negative temperature coefficient. The value of temperature coefficient varies up to several % per degree Celsius. Therefore, thermistors are very sensitive and are able to detect very small temperature variations. In addition, data reading can be obtained easily since thermistors have a high ambient resistance value in the range of $k\Omega \sim M\Omega$. As a consequence, small connection wires have an insignificant impact on the measured data. Thermistors are commonly used in temperature monitoring systems and as switches.

3.3.3.2 Noise thermometry

Noise thermometry is an elegant process of temperature measurement based on the basic characteristics of thermal fluctuation within an electrical resistance. In 1927, J. B. Johnson observed first thermal noise. Later, after Nyquist's explanation of this phenomenon in 1928, a new technique became popular for temperature measurement⁸⁶. Thermal noise is a randomly generated voltage due to conduction electrons Brownian motion^{87,88}. Albert Einstein was the first to predict the existence of the thermal fluctuation in electronic circuits, known today as Johnson noise. It is described by the Nyquist theorem as follows:

$$d\overline{V_T^2} = 4hfRe(Z) \left[\frac{1}{2} + \frac{1}{e^{\left(\frac{hf}{kT}\right)} - 1} \right] df \quad (3-4)$$

Here,

V : noise voltage across the resistor

Z : complex impedance

h : Planck's constant

k : Boltzmann's constant

f : frequency

The noise thermometry is compatible with a wide temperature range from a few mK to 1500 °C⁷⁴. Practically, the most straightforward method for extracting temperature value from noise consists of concentrating in the frequency range where equation (3-4) takes its constant asymptotic value, called white noise, in which the mean square fluctuation of the voltage is directly proportional to temperature and to the resistance value:

$$d\overline{V_T^2} = (4RkT)df \quad (3-5)$$

Where $Re(Z)$ has been also replaced by R.

3.3.4 Resistance Temperature Device (RTD)

RTD is the **R**esistance **T**emperature **D**etector often referred as **R**esistance **T**emperature **D**evice. RTD is a very common way to measure the temperature in different fields, such as industrial application, laboratory, food manufacturing⁸⁹. Temperature is deduced from the resistance variation of the sensing element as a function of temperature.

While thermistors can exhibit both negative and positive TCR (Temperature Coefficient Resistance), RTDs have only positive TCR and are generally made of metal⁸⁵. In addition, thermistors are more sensitive while RTDs are more accurate⁸⁴. The sensitive part of an RTD, generally a highly pure small diameter metallic wire, is often made of materials such as Platinum, Copper and Nickel.

In order to measure temperature, the RTD can be used by supplying a constant current. Since the resistance value of an RTD depends on temperature, then, when the medium temperature changes, the resistance value changes after thermal equilibrium is reached. Knowing the value of injected electric current, a measurement of the voltage value enables the calculation of the resistance value, hence temperature value. Generally, a very small biasing current is chosen to operate the RTD in order to avoid Joule self-heating, which would affect the reading by introducing a severe bias. As a consequence, temperature value provided by the thermometer may be somewhat higher than actual temperature. This discrepancy is known as self-heating error. Self-heating error may occur for different reasons, mainly: i. excessive operating current and ii. low heat transfers between the thermometer and the operating medium.

If R the resistance value for a given temperature T, then the relation between these two quantities can be expressed as follows:

$$R = R_0(1 + \alpha_1.T + \alpha_2.T^2 + \dots\dots\dots + \alpha_n.T^n) \quad (3-6)$$

Where,

R_0 : resistance value at temperature T_0

α_1 : temperature coefficient resistance (TCR); the TCR value is related to the material used for the sensing element of the RTD. For instance, the standard TCR value for platinum is $3.850 \times 10^{-3} \text{ }^\circ\text{C}^{-1}$ ⁸⁴.

The number of terms of equation (3-6) depends on several parameters such as the temperature range, expected precision of measured data, material. But the equation can be reduced as below when the temperature span is short and normal accuracy, in the order of 0.1° is desired:

$$R = R_0[1 + \alpha(T - T_0)] \quad (3-7)$$

Different RTDs are available nowadays for different applications especially based on Pt, which are called Platinum Resistance Thermometer (PRT). The PRTs can be divided into three main categories- i. Standard Platinum Resistance Thermometer (SPRT), ii. secondary Standard Platinum Resistance Thermometer (secondary SPRT), and iii. Industrial Platinum Resistance Thermometer (IPRT). Among these PRTs, some of them are compatible to perform the measurement in immersion mode, which is useful to measure the temperature in water distribution pipelines, tanks and air conditioning systems. Particular RTDs are designed for long-term complete immersion under an aqua environment like- sewers, rivers and cooling ponds. Application fields of different PRTs, their working temperature span and operating medium are reported in Table 3-2.

Table 3-2: Different Platinum Resistance Thermometer and their applications area ⁸⁵

| RTD type | Application | Temperature range | Probe type |
|-----------------|-------------------------------|--------------------|-------------------------|
| SPRT | Calibration of secondary SPRT | -200 °C to 1000 °C | Immersion |
| secondary SPRT | Laboratory use | -200 °C to 500 °C | Immersion, Air |
| Wire-wound IPRT | Industrial use | -200 °C to 648 °C | Immersion, Air, Surface |
| Thin-film IPRT | Industrial use | -50 °C to 260 °C | Immersion, Air, Surface |

3.4 RTD-based Temperature Sensor

Our MPSC contains two kinds of sensors based on RTDs; they were designed and fabricated with distinct configurations, optimized to their different goals. Here we introduce the temperature sensor first.

3.4.1 Design of the temperature sensor

Fabrication details of the considered temperature sensor have already been presented in chapter 2. The final version of the MPSC is based on a silicon substrate and the temperature sensor obtained by metallization. The sensing element or the resistor is made of Pt and the connecting wire is also made of Pt along with gold. Having such sandwich of gold over platinum has the advantage of producing wires of lower equivalent resistivity. Gold was also used to facilitate external connection by creating gold pads on the chip borders and hence to facilitate wire bonding with gold, Figure 3-2(c). The TCR value used for platinum is $2.218 \times 10^{-3} \text{ } ^\circ\text{C}^{-1}$.

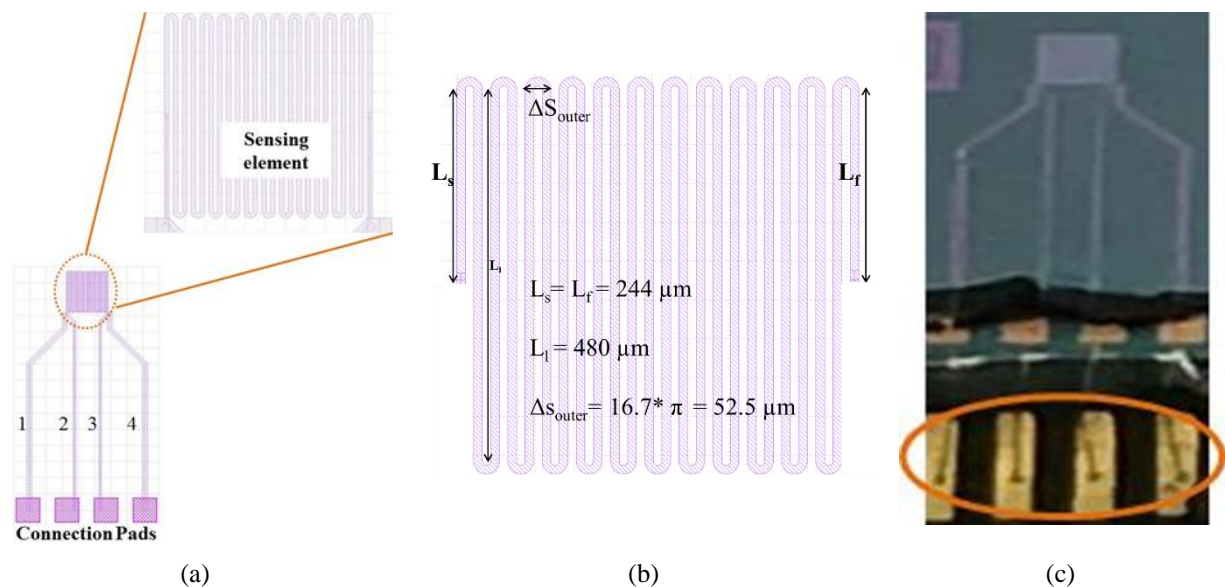


Figure 3-2: (a) Mask Layout of the temperature sensor; 1, 2, 3 and 4 represent the connection wires where 1 and 4 are used for power supply and 2 and 3 to read data, (b) physical dimensions of sensing resistor of the temperature sensor and (c) real temperature sensor.

Figure 3-2 shows the geometry of the temperature sensor. The sensing resistor is connected to four wires enabling four probes measurement. The two outer wires, which are also the widest, are used for current injection through the corresponding pads, while the two inner wires, which also the thinnest, are used for voltage readouts. This 4-probe arrangement allows deducing of the exact resistance of the temperature-dependent sensing element, with minimum influence of the wires.

Therefore, four probes arrangement ensures high precision measurement and reduces parasitic resistance of connection wires. Golden connection pads as well as connections wires are visible in Figure 3-2(c). The orange circle on the same figure indicates the connection between the sensor and the PCB. The connection is protected by UV glue to make it aqua resistive. From Figure 3-2(a), it can be observed that the Pt resistor

(sensing element) has a spiral shape. The spiral geometry is adopted for compactness purposes. The targeted resistance value of the sensing resistor at ambient temperature is around 1 k Ω . According to equation (3-8) below resistance is proportional to its length L , and inversely proportional to its cross-sectional area A .

$$R = \frac{\rho_e L}{A} = \frac{\rho L}{t \cdot w} \quad (3-8)$$

Where,

R : resistance (Ω)

ρ_e : resistivity ($\Omega \cdot m$)

L : length (m)

A : cross section area (m^2)

w : width (m)

t : thickness (m)

The resistivity of platinum in its bulk form is in the order of $\rho_e = 1 \times 10^{-7} \Omega \cdot m$ (more precisely, reported values range from $0.98 \times 10^{-7} \Omega \cdot m$ to $1.11 \times 10^{-7} \Omega \cdot m$ at room temperature). However, it is also well-established that such value of resistivity might vary in a significant manner when considering thin-film deposited materials, as their properties might differ from those of their counterparts in the bulk format. This statement holds true for the electrical resistivity of thin-film platinum layers. In our case those thin-films were obtained by DC sputtering and we found that the corresponding value of resistivity is $3.10 \times 10^{-7} \Omega \cdot m$, which appear three times larger than the bulk value. It is worth mentioning that this value of resistivity was evaluated based on measurements done on a large number of resistors across the wafer.

Other geometrical parameters of the resistance are determined as follows:

The resistor's thickness is given by the value that was selected during fabrication for the thin-film platinum, which is 0.34 μm . As for length and width, they are defined according to our design as follows:

Length = 12255 μm ; Width = 11 μm .

Those dimensions have been carefully selected so as to target a nominal value of 1 k Ω for the resistor. Eventually the nominal resistor was found to be 1.015 k Ω , this value being the result of statistics presented in section 3.5.

It worth-mentioning length of the resistor is rather big value (more than 12 mm) for a micro-scale device. Therefore, the resistor had to be folded so as to minimize its total foot-print. Figure 3-2(d) gives a close view of the resistor design along with some guidelines used to evaluate its total length.

3.4.2 Characterization

The experiment was carried out using a very simple electronic circuit, which enables the control of the injected DC current through the 2 outer ports and recording the resulting voltage difference across the 2 inner ports. Constant current supply was ensured using an IC LM317. LabView software interface was used to read and record data from the electronic circuit. A small supply current of typically 3 mA was used for sensor operation, in order to avoid Joule self-heating. A photography of the experimental setup is shown in Figure 3-3.

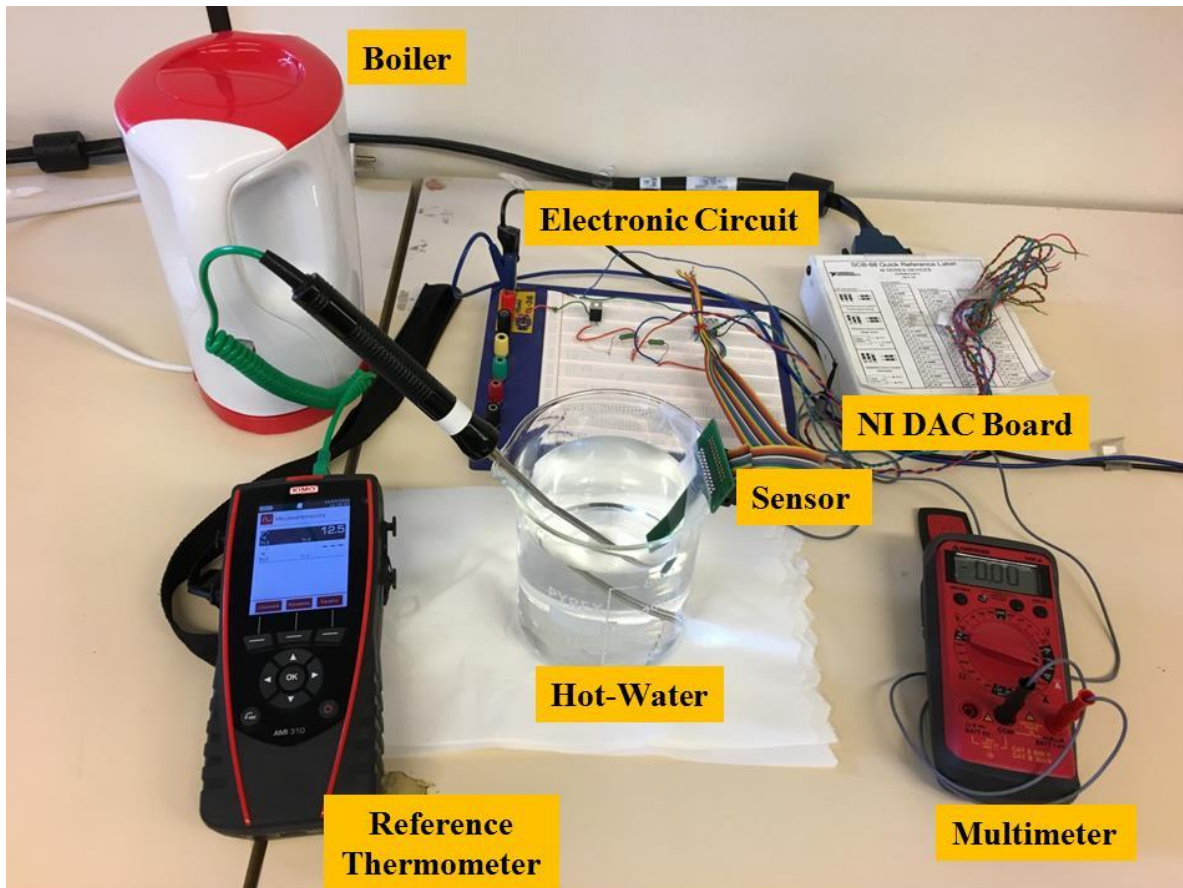


Figure 3-3: Experimental setup for the temperature sensor Calibration.

The sensor response was extracted at different water temperatures under constant current supply whose value is checked using a multimeter. A water boiler was used to warm the water and the hot water poured in a glass beaker, where a reference thermometer (a K-Type thermocouple probe connected to KIMO AMI 310 multi-purpose sensors) was also submerged for calibration purposes. The measurement was performed within the temperature range from 25 °C to 90 °C with a step of 5 °C. Among the four probes, the two inner probes were connected to the LabView data acquisition system NI USB 6216 along with SCB-68. Thirty

measurements were taken at each temperature step in order to calculate the uncertainties for measured value.

The resistance variation as a function of temperature is measured at different water temperatures. The sensing element is a thin-film Pt resistor; which can be considered as a thin-film RTD. Due to the low supply current, no significant Joule self-heating is generated. Therefore, the probe is at thermal equilibrium with its surrounding medium and its resistance value corresponds to the temperature of the surrounding medium. When the sensor is introduced in water at a given temperature, the resistance value varies accordingly.

The temperature sensor response exhibits excellent linearity within the considered temperature range (from 90 °C to 25 °C). The measured response, its resistance variation namely, is plotted as a function of temperature in Figure 3-4. Using the fit equation from Figure 3-4, and given an experimental resistance value within the range shown in Figure 3-4, the corresponding temperature can be calculated in a straightforward manner.

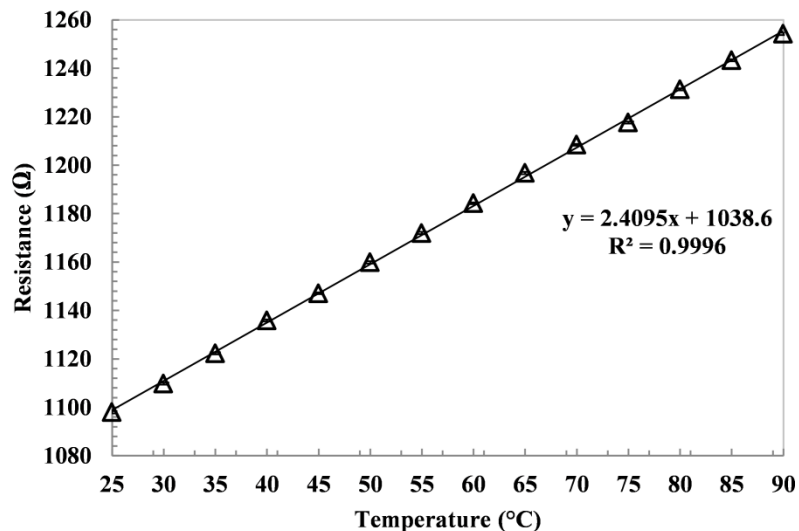


Figure 3-4: Temperature sensor response at different water temperature under 0.5 mA current supply.

From Figure 3-4, it can be observed that the initial resistance value of the temperature sensor is 1098 Ω at 25 °C water temperature. For every 5 °C change in the temperature, the sensor exhibits pronounced variation of resistance. The calculated sensitivity of the sensor in terms of the resistance variation from the measured data is approximately 2 Ω/°C.

3.4.3 Joule Self-Heating

Because electrical current fed into a resistor leads to Joule heating, it may have a more or less severe impact on the actual temperature of the resistor. From this point-of-view, it is important to make sure that a temperature sensor is not affected by this phenomenon, which is called Joule self-heating. On the contrary, Joule self-heating is desired in case of other kinds of sensors based on heat exchange (for instance the thermal flow-rate sensors as well as the Thermal conductivity detectors, as discussed later). An experimental illustration of Joule self-heating is given in Figure 3-5 below.

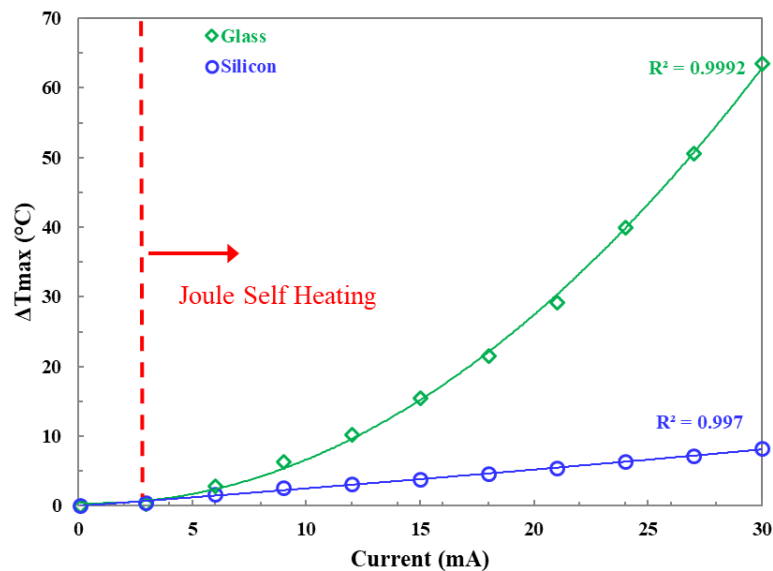


Figure 3-5: Illustration of Joule self-heating phenomenon. Depending on the current magnitude injected into a resistor, the local temperature is more or less affected, leading to 2 regimes: (i) low current, typically for operation of the temperature sensor resistor, (ii) High current, which is conducive to operate the flow-rate sensor resistor.

It is therefore important to control Joule self-heating and precisely know in which operation mode a resistance is used depending on the current or voltage magnitude. This can be studied based on a simple theoretical model described in what follows.

Let's consider a resistor of rectangular cross section, of length L , width w and thickness t in which we inject an electrical current I . The problem is simplified by considering that heat transfer consists only in thermal conduction along the resistor main axis (say x -axis), which also allow us to simplify the situation into a 1D problem. Heat is therefore allowed to flow towards the resistors borders, where the temperature is considered equal constant and equal to the ambient temperature T_0 . Solving the problem starts considering the following equation:

$$\frac{\partial^2 T}{\partial x^2} = \frac{1}{\lambda} Q_{gen} \quad (3-9)$$

Where $Q_{gen} = \frac{I^2 R}{wtL}$ is the generated (electrical) power per unit volume ($\text{J.K}^{-1}.\text{kg}^{-1}$), where R can be rewritten as $R = \frac{\rho_e L}{wt}$, with ρ_e being the electrical resistivity of the resistor's material.

$\alpha = \lambda/\rho c$ is the thermal diffusivity coefficient ($\text{m}^2.\text{s}^{-1}$), with λ being the thermal conductivity ($\text{W.K}^{-1}.\text{m}^{-1}$), ρ the density (kg.m^{-3}) and c the specific heat ($\text{J.K}^{-1}.$

) of the resistor's material.

Solving this equation, considering the boundary conditions of constant temperature at the resistor's borders $x=\pm L/2$, and assuming a constant value for $\frac{1}{\lambda} Q_{gen}$ as a first order approximation, one obtain the following temperature variation:

$$\delta T(x) = \delta T_{max} \left[1 - \left(\frac{x}{L/2} \right)^2 \right] \quad (3-10)$$

with $\delta T_{max} = \frac{L^2 \rho_e}{8\lambda w^2 t^2} I^2$

This leads to an average temperature variation $\langle \delta T \rangle = \frac{5}{6} \delta T_{max}$, which can be rewritten as :

$$\langle \delta T \rangle = \frac{5L^2 \rho_e}{48\lambda w^2 t^2} I^2 \quad (3-11)$$

It is worth-mentioning that when operating at constant voltage U, and considering that $U = RI = \frac{\rho_e L}{wt} I$ the latter equation simplifies as:

$$\langle \delta T \rangle = \frac{5}{48\lambda \rho_e} U^2 \quad (3-12)$$

It appears from this equation (3-11) that the average temperature variation $\langle \delta T \rangle$ scales merely with I^2 and is also dependent on the resistor's dimensions and its material properties. More surprisingly, it also appears from equation (3-12) that when considering operation at fixed voltage, we have no more dependence on the resistor's dimensions. It appears indeed that only the quantity U^2/ρ_e is governing the temperature increase $\langle \delta T \rangle$.

A more standardized way is to express the temperature variation $\langle \delta T \rangle$ as a function of the electrical power $P_e = RI^2$. One then have from both (3-11) and (3-12), the following unified relation:

$$\langle \delta T \rangle = \left(\frac{5}{48\lambda} \frac{L}{wt} \right) P_e \quad (3-13)$$

which can be rewritten in the form:

$$\langle \delta T \rangle = R_{th} P_e \quad (3-14)$$

where we introduce the thermal resistance as follows:

$$R_{th} = \frac{5}{48\lambda} \frac{L}{wt} \quad (3-15)$$

Now if we consider that the temperature dependence of electrical resistance R equation (3-7) where the quantity $(T - T_0)$ is nothing else than $\langle \delta T \rangle$, then repeating the calculations starting from equation (3-9), we obtain the following refined model for $\langle \delta T \rangle$:

$$\langle \delta T \rangle = \frac{R_0 R_{th} I^2}{1 - \alpha R_0 R_{th} I^2} \quad (3-16)$$

$$\langle \delta T \rangle = \frac{(R_{th}/R_0) U^2}{1 + \alpha (R_{th}/R_0) U^2} \quad (3-17)$$

depending whether we operate at constant current or at constant voltage. It is worth mentioning that we obtain a negative sign in the denominator only in equation (3-17) corresponding to constant current operation.

From the above analytical models, one can therefore plot in Figure 3-6 similar curves as the experimental curve presented in Figure 3-5, corresponding to a resistor whose dimensions are ($L= 106 \mu\text{m}$, $w=10 \mu\text{m}$, $t=0.34 \mu\text{m}$) and whose nominal resistance is $9,7 \Omega$ at room temperature. Material properties of platinum are taken as follows: electrical resistivity $\rho_e = 3.10 \times 10^{-7} \Omega \cdot m$, thermal conductivity $\lambda = 71.8 \text{ WK}^{-1}m^{-1}$ and $TCR = 2219 \text{ ppm/K}$. It is worth-mentioning that, contrary to electrical resistivity, it appears from the literature that there is no significant difference between bulk and thin-film values of thermal conductivity. It varies only from 71.8 to $80.7 \text{ WK}^{-1}m^{-1}$ in case of thin-films⁹⁰.

Figure 3-6 gives the calculated temperature variation versus current, based on the first order model (equation 3-11) and the second-order model (equation 3-16). The latter illustrates a clear divergence after 10 mA (while at lower current values, the curves are almost the same). The effect of divergence (due to the negative sign in the denominator of equation 3-16), is very significant at the large current values, since at 30 mA , we reach 1200° while it is only 300° with the first order model. Now comparing those modeling results with the experimental results shown in Figure 3-5, (which show a maximum heating of 65°), one

can conclude that the analytical models give only qualitative trends but they are not enough to give quantitative evaluation of the temperature variation due to self-heating. This is understandable as this discrepancy is due to the numerous assumptions made in our theoretical analytical model (1D modeling, ignoring heat conduction in the surrounding medium, which includes the fluid and the substrate. The effect of the substrate is clear in the experimental results shown in Figure 3-5 since it appears that Joule heating is reduced when using silicon as a substrate, compared to a glass substrate. Better accuracy in the simulations requires numerical modeling.

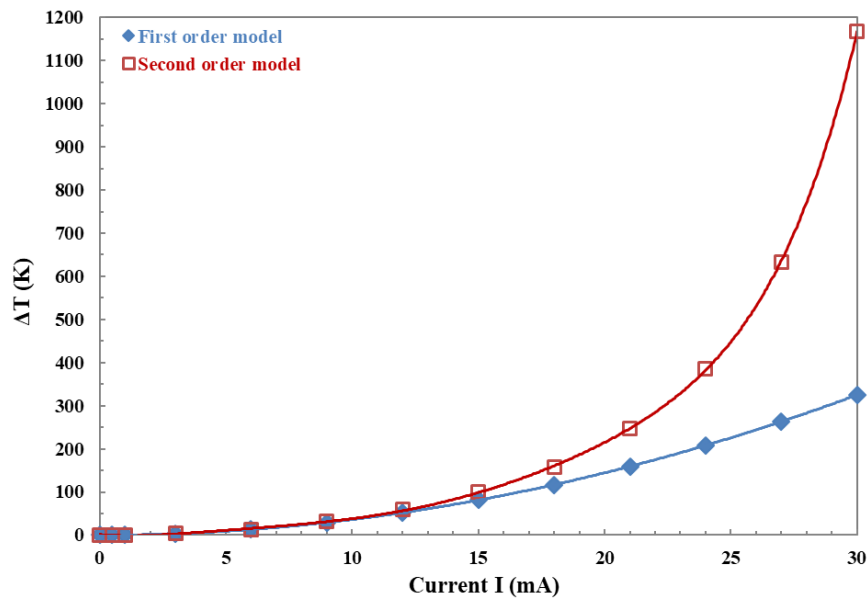


Figure 3-6: Theoretical Joule self-heating on the same resistor as the one considered for the experimental result shown in Fig. 3-5. Both first order model (equation 3-11) and second order model (equation 3-16) have been used.

3.5 Evaluation of fabrication process uniformity in terms of resistance variations and TCR at wafer-level

Nominal values of the sensor's resistance as well as their spread at the wafer level have been evaluated. This study was not limited to temperature sensors. It has been extended for the 3 types of purely resistive physical sensors, considered in the MEMS platform, namely, temperature sensors, flow-rate sensors and pressure sensors.

A summary of the measured data is presented in Table 3-3, Table 3-4 and Table 3-5 below. More details on the distribution of the values over the silicon wafer are given in the following Figure 3-7, Figure 3-8, Figure 3-9 and Figure 3-10. It is worth mentioning at this stage that all recorded values show excellent

uniformity across the wafer with dispersion in the order of 1% up to 2%. Note that such statistics cannot be carried out for the conductivity sensors, as it is designed not to be conductive in air.

Table 3-3: Wafer-level statistics for Temperature Sensor's Resistance Characterization.

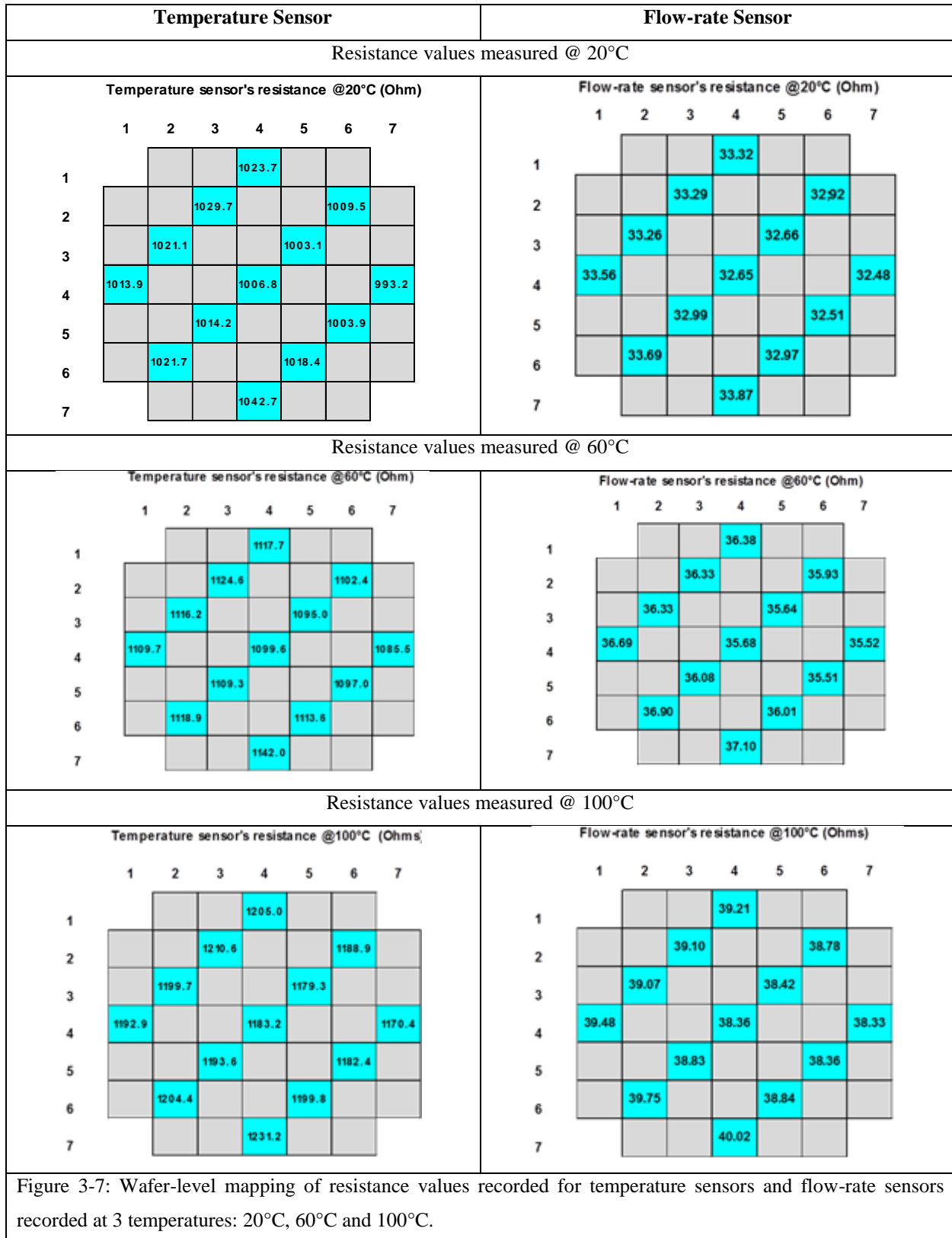
| | Temperature = 20°C | Temperature = 60°C | Temperature = 100°C | TCR (ppm/°C) |
|---------------------------------------|-----------------------|-----------------------|------------------------|-----------------|
| Mean Resistance value (Ω) | 1015,5 | 1110,1 | 1195,5 | 2215 |
| Standard deviation (Ω) | 12,9 | 14,7 | 15,7 | 21 |
| Ratio (%) | 1,3% | 1,3% | 1,3% | 0,9% |

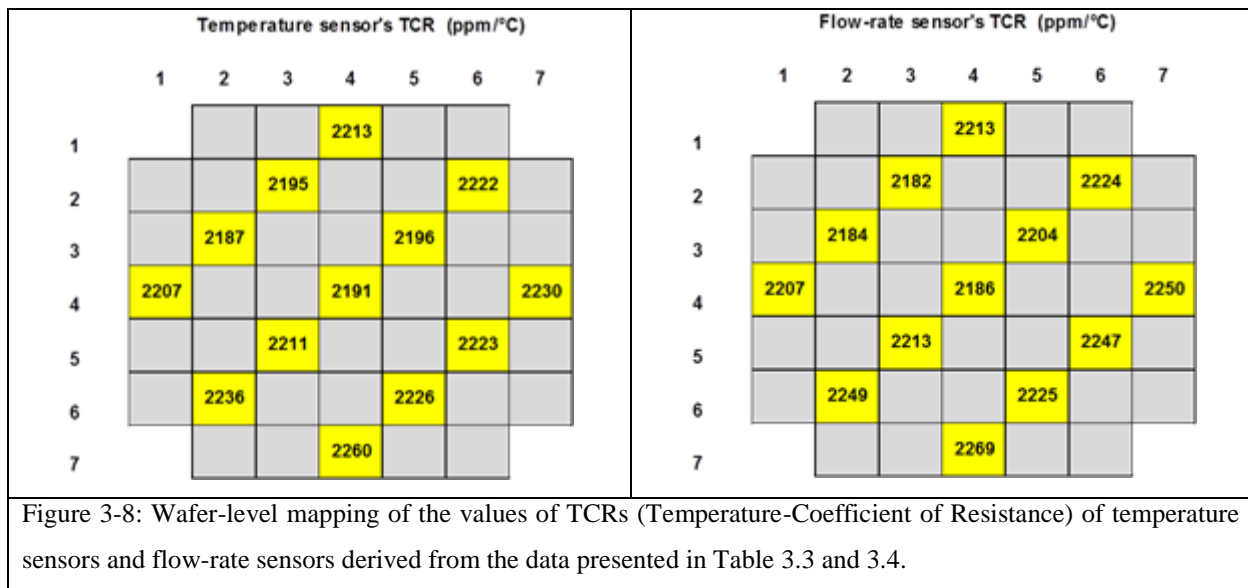
Table 3-4: Wafer-level statistics for Flow-rate Sensor's Resistance Characterization.

| | Temperature = 20°C | Temperature = 60°C | Temperature = 100°C | TCR (ppm/°C) |
|---------------------------------------|-----------------------|-----------------------|------------------------|-----------------|
| Mean Resistance value (Ω) | 33,09 | 36,16 | 38,97 | 2219 |
| Standard deviation (Ω) | 0,45 | 0,52 | 0,55 | 28 |
| Ratio (%) | 1,4% | 1,4% | 1,4% | 1,3% |

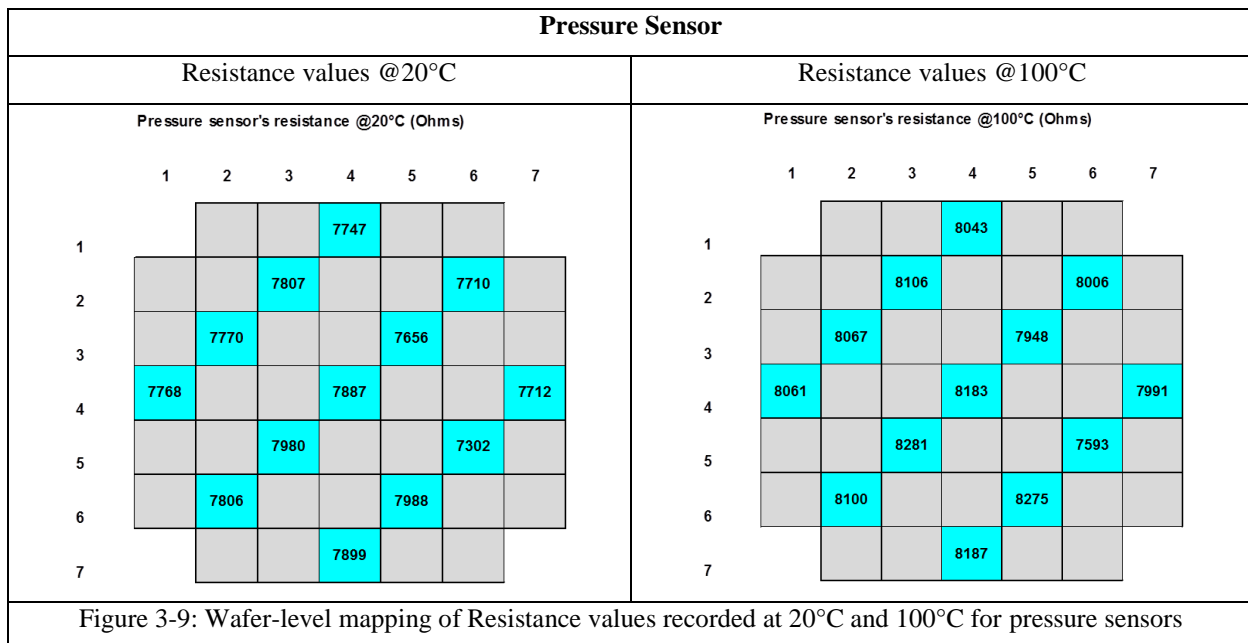
Table 3-5: Wafer-level statistics for Pressure Sensor's Resistance Characterization.

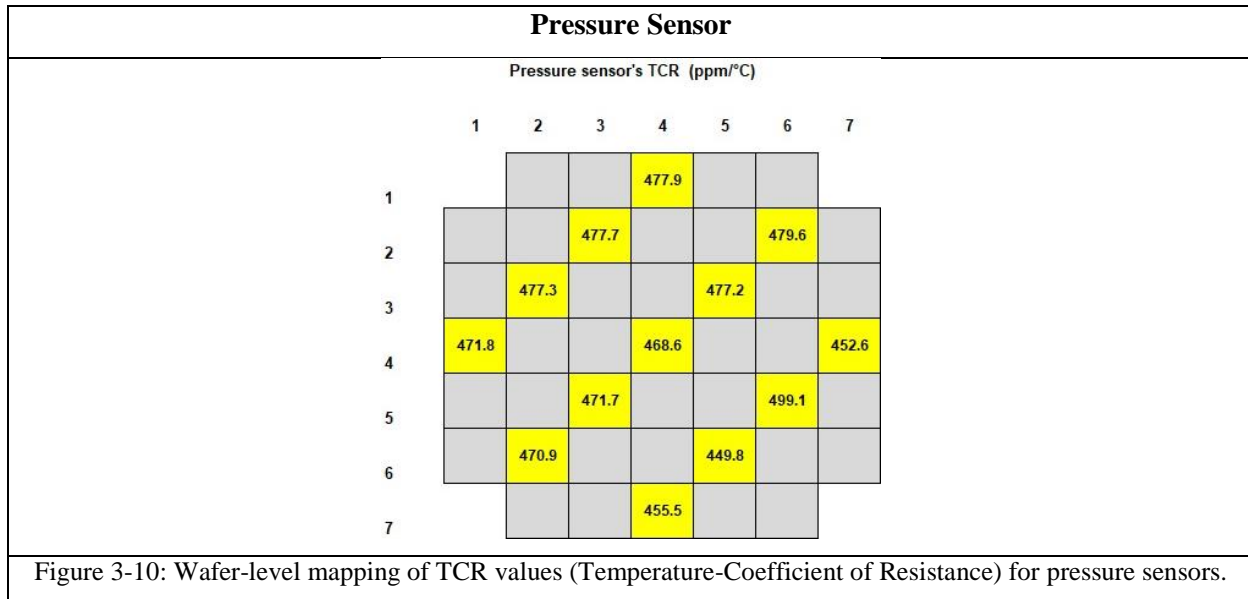
| | Temperature = 20°C | Temperature = 100°C | TCR (ppm/°C) |
|--|-----------------------|------------------------|-----------------|
| Mean Resistance value (Ω) | 7772 | 8065 | 472 |
| Standard deviation (Ω) | 174 | 175 | 13 |
| Ratio (%) | 2,2% | 2,2% | 2,8% |





It is also worth mentioning that the nature of the material used to fabricate the sensing resistors matters a lot. This holds true with respect to the TCR values, which is in the order of 2220 ppm/°C for platinum-based resistors (used for temperature and flow-rate sensors), while it is (only) 472 ppm/°C for polysilicon-based resistors (used for pressure sensors). The latter, though smaller than for platinum, is still significant enough to not be ignored, necessitating some temperature compensation for pressure sensors in the calibration phase. In this respect, it is also worth mentioning that not only the resistance value is temperature-dependent. Indeed, the piezo-resistive coefficient has also some temperature dependence, although limited, but not evaluated in the frame of this work.





3.6 The electrical resistance as a temperature sensor and multi-purpose building block for sensors based on Heat transfer

Resistance variation as a function of temperature enables RTD use in manifold purposes such as flow-rate sensing and thermal conductivity detection (TCD) for gas chromatography (GC). In what follows, we introduce first two important applications of RTDs as a building block of two quite different sensors: (i) a flow-rate sensor and (ii) a thermal conductivity detector (TCD).

3.6.1 Application of RTD as Flow-rate sensor

As we will see more in detail in the next chapter, the flow-rate sensor of the MPSC is a thermo-resistive flow-rate sensor. Its working principle is based on heat transfer between the device and the operation medium. Different versions of the sensor have been fabricated in order to study different parameters. The early versions of the sensor contain three resistors to enable different operating modes: calorimetric, anemometric and time-of-flight. The latest versions contain only *a single resistor* and are optimized for *anemometric* operating modes. The resistors are made of platinum and fabricated on silicon or glass substrates. A detailed discussion of the resistors arrangement and their usefulness to different operation principles will be presented later. All resistors are identical. Each one of them is an RTD. Water flow is determined according to the cooling magnitude of the heating resistor. The resistor is heated by a constant current supply. Under a fluid flow, heat is transferred from the heater to the surrounding medium. The temperature of the resistor decreases gradually as the fluid velocity increases. The cooling magnitude provides information on the fluid velocity and flowrate. In the case of a temperature sensor, a low supply current is preferable in order to avoid Joule self-heating which is obviously not the case for the flow-rate

sensor. On the contrary, significant Joule self-heating is desirable for the flow-rate sensor. The initial self-heating temperature is an important parameter for a thermal flow-rate sensor. High self-heating temperature leads to a highly sensitive sensor and a wide turn-down ratio. Hence, if optimal self-heating is ensured with moderate current supply, an RTD can be used as a thermal flow-rate sensor.

3.6.2 Application of RTD as Thermal Conductivity Detector (TCD)

A thermal conductivity detector is a device which detects the variation of the thermal conductivity of its surrounding medium. Such device is commonly used for gas chromatography (GC). TCD becomes a key part of miniaturized GC—or micro GC (μ GC). μ TCD is actually a non-specific and non-destructive detector for GC, therefore it can detect several compounds including— air, carbon monoxide, hydrogen, sulfur oxide, nitrogen and so on ⁹¹. In GC systems, TCD is used to sense the variation of the thermal conductivity of samples (gases) which enables determining their composition. The generic system configuration contains two channels: one is used as reference and other for measurement. The reference channel contains the pure carrier gas flow. On the other hand, the second one contains the sample to be analyzed in addition to the carrier gas. TCDs are placed in both channels. Both RTDs and thermistors can be used for this purpose. The difference in gases composition of the two channels induces a thermal conductivity difference. This thermal conductivity difference leads to different equilibrium temperatures of the two TCDs, hence, to a voltage difference if RTDs of identical initial resistance are used and operated under the same constant current. The generated signal, voltage difference for instance, is proportional to the sample concentration in the measurement channel.⁹² Commercially available TCDs have different configurations. Some of them are based on thin-film RTD while others are based on small bead thermistors ⁹³.

3.7 RTD Transient Behavior

In the above two examples of sensors involving an RTD, besides the needs for temperature measurements, there is a crucial role of the different heat transfer mechanisms, that is convection and conduction in both cases. The dynamics of those heat transfer mechanisms involve a time constant to account for the overall thermal behavior of the device. Such time constant will have important consequences in the sensor performance and its response time will be affected. It is therefore important to study the transient behavior of the TCD seen as a building block that can be used for a variety of sensors.

As a first guess the thermal time constant will strongly depend on the device architecture and its constitutive materials. It is likely that the device environment will be an important factor. Not only will matter the nature of the surrounding fluid, but also its velocity and initial temperature. All those parameters will be considered in what follows through simulations and experiments.

3.7.1 Simulation of RTD transient behavior

3.7.1.1 Simplified theoretical model of thermal time constant accounting for heat conduction

An analytical formula can be derived for the thermal time constant, through simplified theoretical modeling. To this end, we will make the same assumptions as in section 3.4.3, considering a 1D model for the resistor of rectangular cross-section, considering that heat transfer is done only by conduction through the resistor's main axis. In this case, we need to take into account the time dependence of temperature in the heat equation, as follows:

$$\frac{\partial^2 T}{\partial x^2} - \frac{1}{\alpha} \frac{\partial T}{\partial t} = \frac{1}{\lambda} Q_{gen} \quad (3-18)$$

The thermal time constant can be obtained by solving the equation without right-hand part, also corresponding to a cooling process:

$$\frac{\partial^2 T}{\partial x^2} - \frac{1}{\alpha} \frac{\partial T}{\partial t} = 0 \quad (3-19)$$

We can also capitalize on part of the results obtained in the steady-state regime and detailed in section 3.4.3. In particular, we saw that the temperature distribution has a parabolic shape with a maximum value given by equations (3.10) and (3.11). Here, for better convenience when solving equation (3.19), instead of a parabolic shape, we will approximate the temperature profile by a cosine function. The general solution of (3.19) can then be written as:

$$\delta T(x, t) = \delta T_{max} \cos \frac{\pi x}{L} \cdot e^{-\frac{t}{\tau}} \quad (3-20)$$

Then, the time constant τ can then be obtained by injecting equation (3.20) into equation (3.19). Recalling that $\alpha = \lambda/\rho c$, one finally obtain :

$$\tau = \frac{\rho c L^2}{\pi^2 \lambda} \quad (3-21)$$

It appears that resistor's length L is the major factor affecting the time constant, besides thermal diffusivity, at least based on our assumptions made in this simplified model.

Similarly, to the thermal resistance introduced in equation (3-14), one can also introduce the thermal capacitance by considering that the time constant can be written as an RC product:

$$R_{th} C_{th} = \tau = \frac{\rho c \pi L^2}{\pi^2 \lambda} \quad (3-22)$$

Which leads to:

$$C_{th} = \frac{48}{5\pi^2} \frac{\rho c L w t}{\lambda} \quad (3-23)$$

Finally, one can also build a second-order model, similarly to the method used in section 3.4.3, taking into account the temperature dependence of the resistance. After calculation, one eventually obtain:

$$\tau' = \frac{R_{th} C_{th}}{1 - \alpha R_0 R_{th} I^2} = \frac{\tau}{1 - \alpha R_0 R_{th} I^2} \quad (3-24)$$

$$\tau' = \frac{R_{th} C_{th}}{1 + \alpha (R_{th}/R_0) U^2} = \frac{\tau}{1 + \alpha (R_{th}/R_0) U^2} \quad (3-25)$$

Depending whether one operates under constant current I or under constant voltage V . Here again it is also worth mentioning that the time constant can be either decreases or increased severely, when taking into account the negative sign in the denominator of equation (3-25).

3.7.1.2 Numerical simulations

Numerical simulations can take into account several factors that have been ignored in the previous simplified analytical model. First, instead of 1D modeling, one can have a better representation of the resistor shape as schematized in Figure 3-11 (a). Second, as depicted in Figure 3-11 (b), one can take into account the surrounding environment, which consists of a substrate material (either silicon or glass) and a surrounding fluid (either air or water).

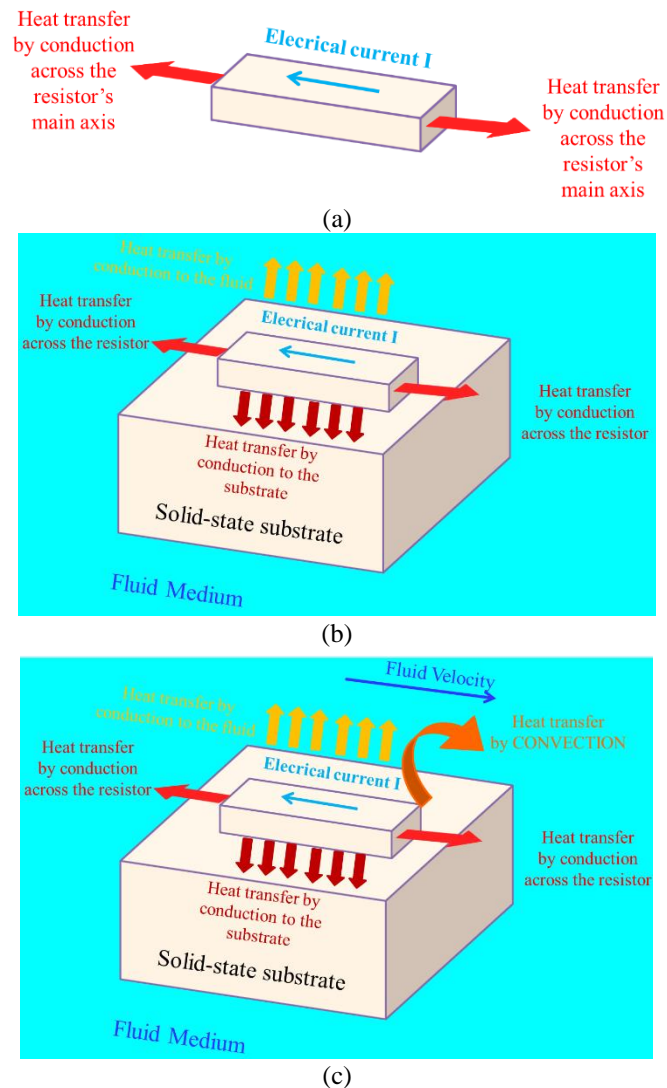


Figure 3-11: Sketch of 3 different models accounting for heat exchange phenomena on a heated resistor. (a) heat transfer only within the resistor's material, (b) additional heat exchanges with the substrate material and surrounding fluid medium and (c) heat transfer through convection due to the fluid velocity.

Those materials both solid and fluidic will lead to additional heat conduction. Finally, in case the fluid is moving with a given velocity, one can also take into account the resulting additional heat transfer by convection, as illustrated in Figure 3-11 (c).

Those different scenarios have been evaluated in the simulation results presented in what follows. The numerical simulations have been performed on COMSOL Multiphysics based on the same resistor described before for the temperature sensor, made of platinum and with dimensions given in section 3.4.1.

First, we considered the effect of the substrate material (either glass or water) as well as the effect of the surrounding fluid (either air or water). The corresponding results are Figure 3-12 and summarized in Table

3.10. First, one can notice from these results that water environment leads to much higher time constants than in air, nearly 10x more.

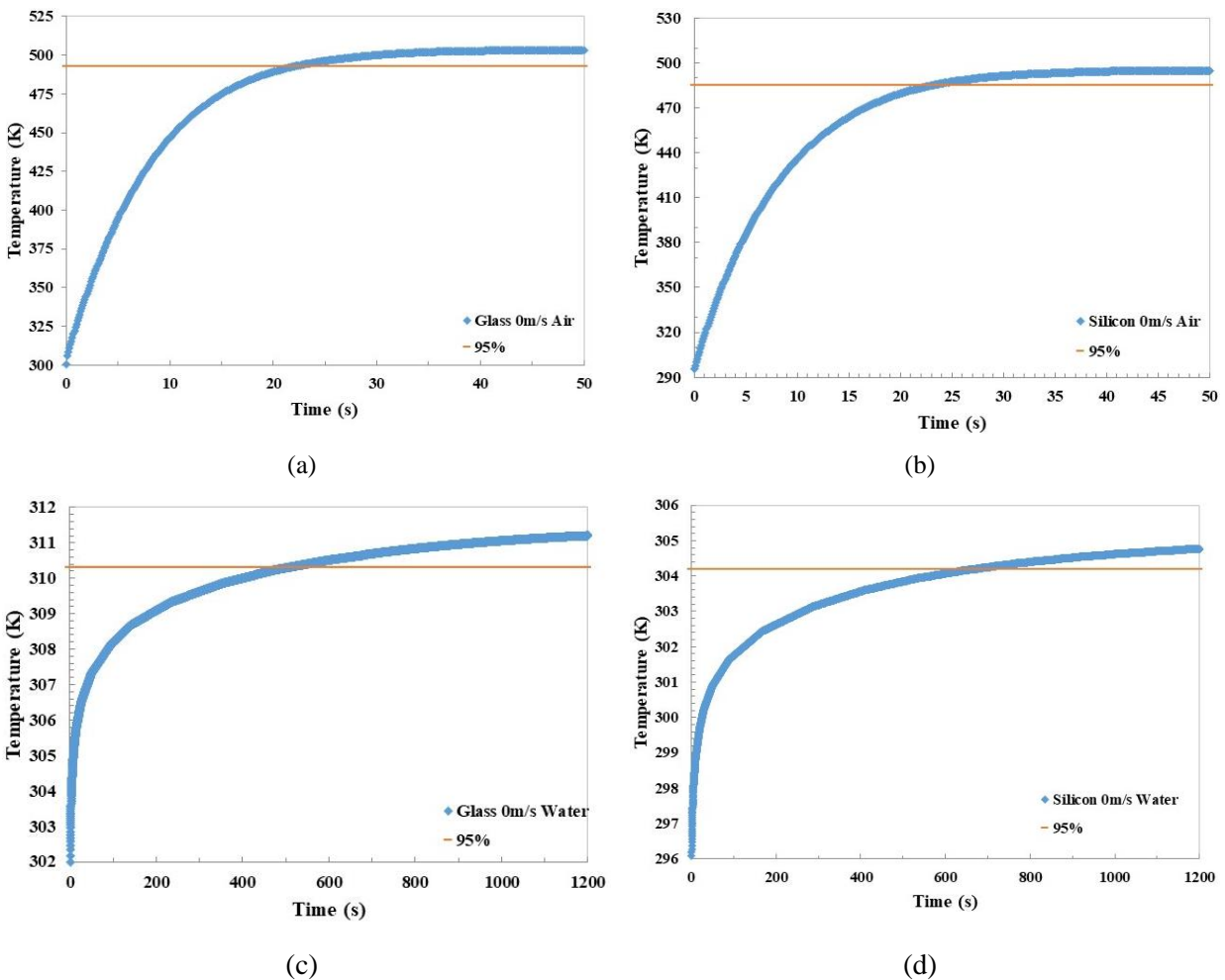


Figure 3-12: Numerical simulations of the transient temperature response, considering different substrate materials (Silicon versus Glass) and surrounding fluid media (Air versus Water).

Table 3-6: Thermal time constant considering different substrate materials and surrounding fluid media

| | Glass substrate | Silicon substrate |
|-----------------------------------|------------------------|--------------------------|
| Surrounding fluid is Air | 21 s | 23 s |
| Surrounding fluid is Water | 507 s | 662 s |

In order to illustrate the scenario depicted in Figure 3-11(c), which considers a forced convection heat transfer, we performed additional simulations, where we introduced fluid velocity of different magnitudes.

The corresponding results of the simulated transient response are shown in Figure 3-13. It is interesting to note that it is not only the steady state temperature which is affected by fluid velocity –which was expected by due to the additional convective heat transfer, due to a large velocity. Indeed, it also appears that the time constant is also affected by the velocity. This important observation suggests new possible operation modes for flow-rate sensors operating in transient mode, rather than in steady state. Indeed, besides the novelty of such approach, such operation in transient mode may reduce the time required for measurement since there will be no need to wait for the steady-state. Hence, as time decreases, the total energy consumption of the sensor can be reduced accordingly.

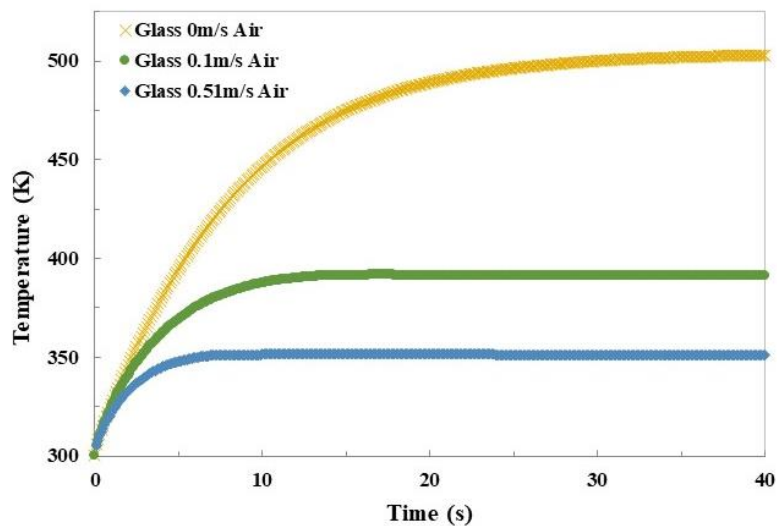


Figure 3-13: Numerical simulations of the transient temperature response of a heated resistor, considering the effect of velocity (in this case substrate material is Glass and surrounding fluid is Air).

3.7.2 Experimental measurement of RTD transient response

In what follows, we present experimental results of the transient response of resistor's temperature operated under different conditions. Recall that temperature is acquired directly through reading the resistance value.

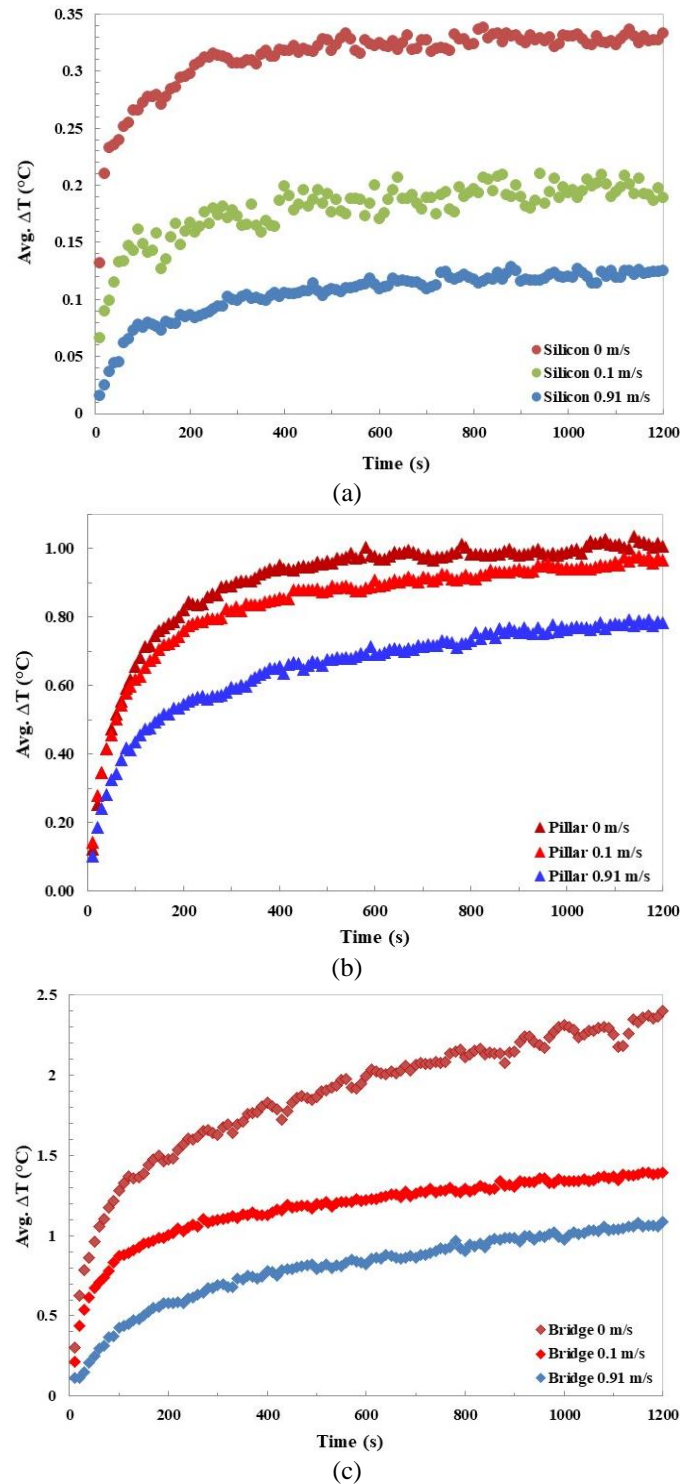


Figure 3-14: Experimental measurement of the transient temperature response of 3 different resistor designs based on silicon substrate, operated under 3 different water velocities.

Experimental results are consistent with previously presented numerical trends. In addition to the effect of velocity and substrate material, we highlighted an additional dependence of transient response to the device structure and geometry.

3.8 Conclusion

In this chapter, we introduce the needs for water temperature measurement and highlight the importance of this parameter as it affects many others. Aiming to develop a temperature sensor, we introduced the platinum-based Resistance Temperature Device (RTD) as a suitable solution for operation under water environment, which eventually appears also as a convenient building block for other kinds of sensors based on heat transfer, which include the flow-rate sensor, presented in the next chapter. The RTD has been studied in detail through analytical models, numerical simulations and experimental measurements. Both steady-state and transient behavior have been investigated.

4 Chapter 4: Flow-Rate Sensor Co-integration

4.1 Background and State of Art

4.1.1 Flow-rate measurement

Flow-rate measurement is important in different aspects of human life. From the very beginning of the human being civilization until now, flow-rate measurement is involved in different fluid media. The history of flow-rate measurement is quite primordial. Since the early ages, cognitive perceptions about the direction and the velocity of different fluids *i.e.*, air, water helped the helmsman for navigation purposes. In the ancient times, the Egyptians used flow measurement of the Nile river's water in order to predict their crops harvesting condition^{94,95}. From historical perspective, the first water flow measurement was used by the ancient Sumerians cities of Ur and Kish near to the Tigris and Euphrates rivers in 5000 BC for supplying water in the cities' aqueducts⁹⁶.

Daniel Bernoulli (1700-1782), a Swiss physicist was a pioneer to develop the scientific concepts for determining flow-rate. He succeeded to establish a first relation between pressure loss and velocity.

An important subsequent contribution was provided by British scientist Michael Faraday (1791-1867) in 1831⁹⁷. His law on electromagnetic induction is involved in the working principle of the magnetic flow-rate sensor, also referred to as flowmeter in what follows. He discovered that, if a copper disk is rotated in-between the two poles of a permanent magnet then it generates electricity. Using the same principle, the velocity of a fluid can be determined. If a conductor is rotated by a liquid in a magnetic field through a pipe whose diameter is known, then the voltage produced by induction process can be used to access the corresponding information about fluid velocity.

Using the Doppler effect another flow measurement technique was developed, which is known as Doppler flowmeter. Christian Doppler (1803-1853) observed that, if a sound source is moving towards the sound receiver then the frequency appears higher. Hence, flow-rate can be calculated using the shift in frequency as a function of the average travelling velocity. Many other kinds of flowmeters were developed since that time.

An important parameter has to be considered while measuring the flow-rate or the velocity of a fluid; it is the velocity regime of the corresponding fluid. There are mainly two fluid flow regimes that can be distinguished: *Laminar* flow and *Turbulent* flow. The British mechanical engineer Osborne Reynolds proposed a dimensionless parameter called after him, the Reynolds number denoted by R_e and defined by $R_e = \frac{LV}{\nu_e}$, where L is the characteristic length of the medium, V is the fluid velocity and ν_e is the kinematic

viscosity of the fluid (m^2/s). It can be also written as $R_e = \frac{\rho LV}{\mu}$, where μ is the dynamic viscosity and ρ the density of the fluid medium. In the latter formulation one can notice that the Reynolds number reflects which effect dominate among inertial (proportional to ρ) and frictional (proportional to μ) depending on fluid velocity V and characteristic length L . The value of R_e actually provides information about the flow regime whether it is laminar or turbulent. It is usually admitted that when $R_e < 2300$, the flow is considered as laminar and when $R_e > 4000$, the flow is turbulent. When the value of R_e ranges between 2300 and 4000 then the flow is in the so-called transient regime.

Nowadays, advanced technologies have enabled sophisticated flow-rate measurement devices based on the above-mentioned principles and others, which can provide accurate measurement within a wide flow-rate range. In particular, the micro and nanotechnology bring a significant advancement in the case of miniaturized flow-rate measurement devices. There are numerous advantages of such miniaturized devices in terms of production cost, easy installation and maintenance, large-scale implementation⁹⁸ as well as their suitability for measurement in confined environments including microscale channels. Due to the smaller size of this sort of micro-machined flow-rate devices, they are being used in the field of biology^{99,100}, and medical applications^{76,101,102} as well as applications of microfluidics at large. Besides, accurate microscale flow-rate measurement is important in some other branches of science and engineering like- gas chromatography^{75,103,104}, environmental monitoring^{105,106}, weather forecasting¹⁰⁷, aircraft monitoring⁷⁸ and industrial process control¹⁰⁸.

4.1.2 Commercial flow-rate sensors

As mentioned in the previous chapter, the aim of this work is to develop a multi-parameter sensing module for an application to water networks monitoring. In the proposed module, a micro-machined thermal flow-rate sensor is used to measure the water flow-rate. Several commercial flow-rate sensors are already available in the market in order to respond similar need, but they are mostly based on single devices and their operating principle is not always applicable in micro-scale, neither they can be found in a co-integrated format with other kinds of sensors. All these flow-rate devices are realized based on different operation principles and applicable in different fluid media- gas, air, water and oil. For instance, OMEGA® is a specialized company in flow-rate meter manufacturing and they produced a wide variety of flow-rate meters for various kinds of fluid media.



Figure 4-1: Flowmeters manufactured by OMEGA company

Figure 4-1 illustrates a few flow-rate meter products manufactured by OMEGA. Another illustration is the company named UFM ® (Universal Flow Monitoring), which also manufactures different flowmeters like OMEGA including thermal flowmeters for measuring air and gas flow. One can also mention the Chinese company named LONGRUN ® produces heat meters, water meters and flowmeters only based on Ultrasonic measurement (Figure 4-2). They produce various ultrasonic flowmeter with several options like portability, high accuracy, clamped and splitting connections etc. Big names of manufacturers of flow-rate sensors include BRUKER®, SENIRION®, NEWPORT®, SEAMETRICS®, AQUEOUS®, HYDROTECHNIK®, AW-LAKE®, FIRST SENSOR®, KOBOLD®, to name a few.



Figure 4-2: Different Ultrasonic Flowmeters of LONGRUN company

4.1.3 Micro flow-rate sensors

(a) Microfluidic instrumentation:

All the above mentioned flowmeters are compatible to measure different fluid flows in macroscopic scales. Besides, there is a need to generate or measure the fluid flow at microscale or even at nanoscale. The company Fluigent® has developed a microfluidic instrumentation platform which can produce and measure flow with high precision at the microscale so as to enable flow control within microfluidic devices and related experiments. The whole system for flow control consists of two kinds of devices- on one hand, an adjustable pressure generator and on the other hand, flow measurement devices, which consists of flow units connected to a flow board. The flow units measure the fluid flow at different locations of the fluidic circuit while the flow board is working as a communication hub between flow units and the software interface. Figure 4-3 illustrates typical Fluigent devices. It is worth mentioning that fluid units can be

operated in a closed-loop mode together with the pressure generator so as to achieve high precision flow-rate control. A similar microfluidic instrumentation platform is also proposed by the company ELVEFLOW[®].



Figure 4-3: Fluigent flow-rate platform, (a) adjustable pressure generator (b) flow units connected to the flow board

(b) Micro-machined flow-rate sensors:

In the recent decades, due to the advancement of the micro and nanofabrication technologies, there are numerous micro-machined flow-rate sensors, such as the flow-rate units used by Fluigent in their instrumentation platform. Such flow-rate microsensors have been developed by different research groups. For instance, M. Dijkstra et al. proposed a micro-machined flow-rate microsensor to measure the water flow in nano-litre scale based on calorimetric operation principle¹⁰⁹. The heating element of this sensor is placed inside a microchannel which is made of silicon-nitride. Planar integration ensures the close proximity to the fluid and avoids large dead-volumes.

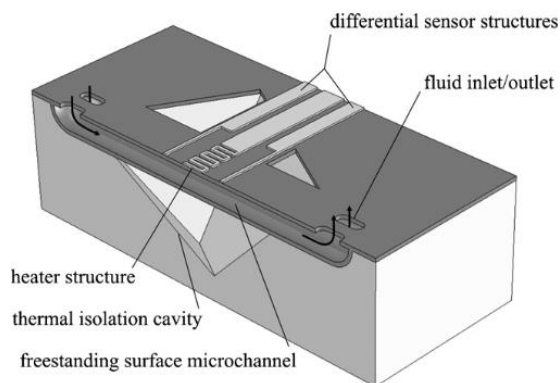


Figure 4-4: Cross-section view of a micro-machined flow-rate sensor¹⁰⁹

Figure 4-4: shows the schematic cross-section view of the heater, thermal isolation cavity and suspended microchannel. This sensing device has low hydraulic resistance with a total 4.5 nL fluidic volume. Pressure

is used as an external force in order to introduce the water flow inside the microchannel. The suspended thermal isolation cavity length is $800\ \mu\text{m}$ and the microchannel dimensions are $5\ \mu\text{m} \times 15\ \mu\text{m} \times 80\ \mu\text{m}$. The output sensitivity of the sensor is $0.2\ \mu\text{V}/\text{nLmin}^{-1}$ and it can measure the water flow up to $300\ \text{nL}/\text{min}$ ¹⁰⁹.

A thermal MEMS sensor for nano-fluidic application is designed by Shuyun Wu et al. with two different physical configurations¹¹⁰. In the first version, the heater is placed on the substrate and in the second version, the heater is fabricated in a suspended mode where a portion of the substrate is taken off leading to a suspended microchannel. The schematic images of these two configurations are presented in Figure 4-5.

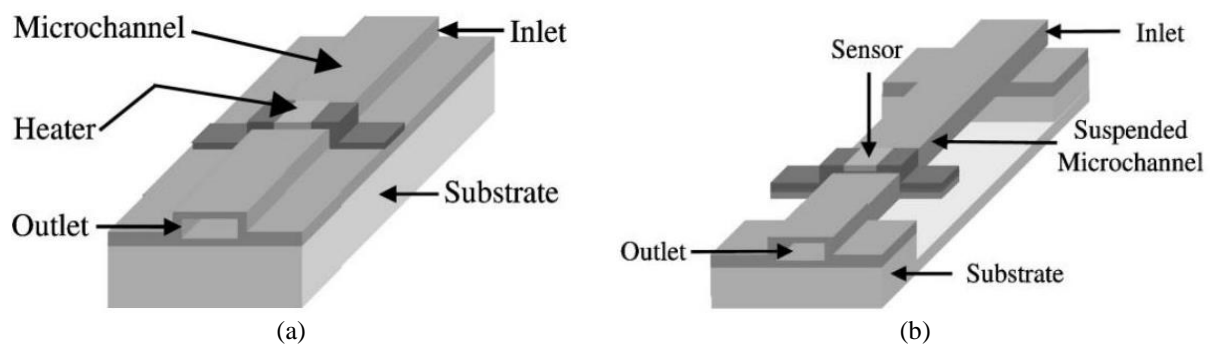


Figure 4-5: A microchannel flow-rate sensor, where the channel is fabricated on (a) the substrate and (b) in suspended configuration¹¹⁰

The heater is made of boron-doped polysilicon thin-film which is integrated within a silicon-nitride microchannel. The channel dimensions are $2000\ \mu\text{m} \times 20\ \mu\text{m} \times 2\ \mu\text{m}$. The reason behind to choose the boron-doped polysilicon is to obtain a high TCR (temperature coefficient of resistance) value for the heater. This sensor has a flow-rate resolution about $0.4\ \text{nL}/\text{min}$ and it can detect the micro bubbles in the fluid¹¹⁰. The picture of the real fabricated devices is shown in Figure 4-6.

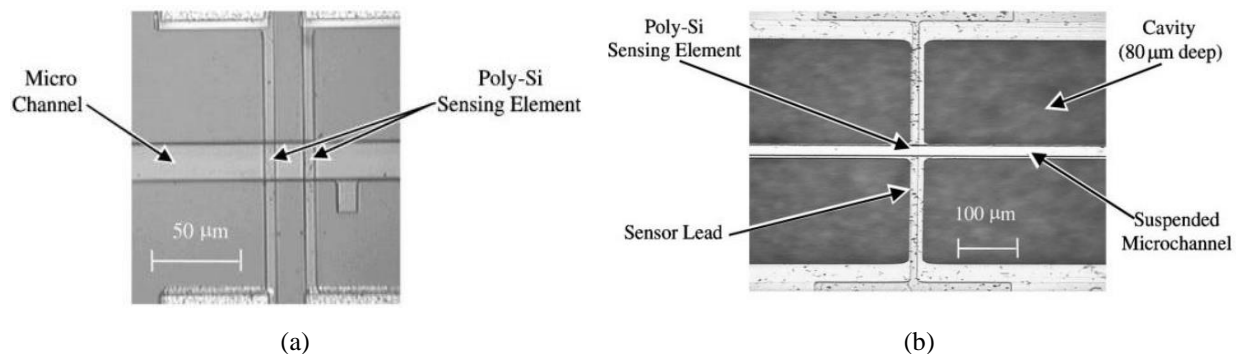


Figure 4-6: Fabricated flow-rate sensor (a) microchannel fabricated on the substrate and (b) a suspended microchannel¹¹⁰

An artificial lateral line MEMS flow-rate sensor was developed by Jack Chen et al. which is based on the concept how a fish senses the surrounding flow field ¹¹¹. The goal here was to mimic the fish flow sensing system. A fish uses its neuro-mast which is composed of hair cilium and nerve cells to sense the water displacement. But this neuro-mast does not have the direct contact with the water. It is a part of the lateral line under the epidermis and this lateral line has canal on it to sense the water displacement. A sensor array can be used to perform a similar action where each sensor contains in-plane fixed cantilever and a fabricated cilium will be attached vertically at the free end of the cantilever (Figure 4-7). Therefore, the external flow has an effect on the cilium and due to the rigid connection between the cantilever and the cilium a mechanical bending is sensed by the cantilever beam. The bending magnitude can be captured by the piezoresistive sensor. In order to interpret accurate flow field and access the information about the flow field structure evolution, an array of individual sensor nodes can be implemented in the operation media with systematically varying the position and orientation of cilium with different heights.

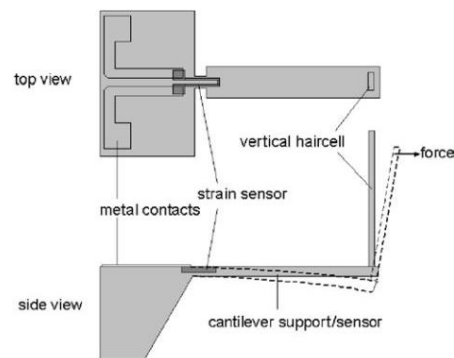


Figure 4-7: Schematic representation of single hair cell biomimetic flow-rate sensor ¹¹¹

In spite of the availability of different sensors in macro or micro scales for measuring the water flow-rate, still there is a need of a complete monitoring system which will not only measure the water flow but also provide information about other parameters of the water environment. Hence, the novelty of our flow-rate sensor is that it is not a single sensing device rather it is a part of a multi-parameter sensing system (MPSC) which is a smart and complete multipurpose module to monitor the water distribution network. Moreover, such micro-machined flow-rate sensor is not well-acquainted with the conventional water distribution system. The considered flow-rate sensor can cover more than the usual flow-rate range of the distribution system. The normal water velocity of a water distribution network ranges between 0.1 m/s and 10 m/s.

A comparative study is reported below in Table 4-1 between the considered flow-rate sensor of the MPSC and state-of-art devices. The collation of comparison is made upon focusing on two important

parameters: power consumption and velocity/flow-rate range. The information about power consumption and velocity range are rarely available conjointly in most cases. Therefore, a few articles are enlisted here among numerous publications, which are mainly focused on micro-machined devices.

Table 4-1: Comparison between the fabricated flow-rate sensor and the existing devices in terms of power consumption and velocity.

| Micro-machined Flow-rate sensor | Power consumption | Velocity/flow-rate | Application domain |
|--|---|--|----------------------------------|
| Silicon substrate | | | |
| Ref. Dev. 1 ¹⁰⁹ | > 30 mW | 300 nL/min (in water) | Micro and nano |
| Ref. Dev. 2 ¹¹² | 600 mW | 25 μ L – 10 mL/min (in water) 0 – 60 mL/min (in Nitrogen) | Mass-flow |
| Ref. Dev. 3 ¹¹⁰ | 140 μ W | < 10 nL/min (DI water) | Micro and nano |
| Ref. Dev. 4 ¹¹³ | 5 mW | 0 – 10 mL/min (in viscose sugar water) | Biomedical |
| Ref. Dev. 5 ¹¹⁴ | < 5 mW | 100 μ g/h (in water) 100 nL/h (in gas) | Biology/Bio-MEMS |
| Ref. Dev. 6 ¹¹⁵ | 5.8 mW | 0 – 5 m/s (in air) | Autonomous navigation |
| Ref. Dev. 7 ¹¹⁶ | 1 mW/mm ² (in gas) 4 mW/mm ² (in liquid) | 0 – 4 m/s (in liquid) 0 – 180 m/s (in gas) | Thermal mass-flow |
| Ref. Dev. 8 ¹¹⁷ | < 10 mW | 0 – 8 m/s (in water) | Micro biology and micro chemical |
| Ref. Dev. 9 ¹¹⁸ | 380 μ W | 0 – 1 m/s (in gas) | Microfluidic |
| Our silicon based pillar device | 43.78 mW | 0 – 0.91 m/s (in water) | Water distribution network |
| Glass substrate | | | |
| Ref. Dev. 10 ¹¹⁹ | 3.3 W | 10 – 250 mm/s (in air) | Lab-on-chip |

| | | | |
|--|------------------|--|--|
| Ref. Dev. 11 ^{120,121} | 150 mW | 6.48 m/s (in Nitrogen) | Gas flow-rate, automotive and domestic |
| Ref. Dev. 12 ¹²² | 75 mW and 200 mW | 0 – 20 sccm | Microchemical reactors |
| Ref. Dev. 13 ¹²³ | 31.6 μ W | 190 mm/s (in air) 7.8 mm/s (in water) | Biomimetic flow sensing |
| Our glass substrate device | 13.21 mW | 0 – 0.91 m/s (in water) | Water distribution network |

From the tabulated information, it can be seen that the majority of micro-machined flow-rate devices are compatible with micro and nano fluidic applications and their turn-down ratio is limited to μ L or nL. None of them can be employed in the targeted medium (water distribution network) of flow-rate sensor of the MPSC. Among mentioned devices, reference device 11 can be implemented in a domestic environment in a gaseous media. Hence, two versions of the considered flow-rate sensor are highlighted here based on the glass and silicon substrate. These two flow-rate sensors cover a wide velocity range in comparison with existing devices under moderate power consumption. It can be noticed from the table that the proposed silicon substrate pillar device consumes more power than the glass based device. The reason behind this higher power consumption of the silicon substrate device is explained explicitly in the result and discussion section.

4.1.4 Thermal Flow-rate sensors

At the beginning of this chapter, we discussed the different operation principles of a flow-rate sensor. In order to access the flow-rate information of a fluid, a flowmeter can be developed *a priori* based on any working principle. It can be observed that most of the operating mechanisms are based on either mechanical or thermal transduction method. For micro-machined flow-rate sensors, the thermal-based working procedure is the most widely used ^{110,111,124}. The flow-rate sensor of the MPSC is a thermo-resistive flow-rate sensor and its working principle relies on heat energy transfer to the surrounding medium. A platinum thermistor is used as a heating element of the flow-rate sensor, which is heated by injecting an optimum amount of current. When the sensor is subjected to the fluid flow then the heat will be taken away by the fluid flow leading to cooling of the heater. The magnitude of this cooling is proportional to the fluid velocity. Thermal flow-rate sensors can be categorized into three categories based on their operation principle- (i). Anemometric (Hot-wire), (ii). Calorimetric and (iii). Time-of-Flight (TOF) ⁸². A detailed description of these three working principles is presented in the following section.

(i) Anemometric operation principle

An anemometric flow-rate sensor or Hot-wire measures the effect of flowing fluid on a hot body. Normally, in an anemometric flow-rate sensor, a metallic resistor is used as a heater^{77,125}. When the sensor is submerged in the flowing fluid, heat is transported from the heater, which causes a variation of its temperatures. Heat is transferred from the heater to the substrate by thermal conduction. However, between the heater and the fluid, heat transfer is governed mainly by convection which strongly depends on the fluid velocity. Consequently, the fluid velocity can be deduced from the heater temperature variation. For a given electrical power supply, the heater resistor reaches its maximum temperature under zero velocity. Afterwards, temperature gradually decreases as the fluid velocity increases. Therefore, the velocity information can be simply extracted by reading the voltage or the resistance change of the heating resistor since the resistor value depends on temperature.

An analytical theoretical model can be established in a quite straightforward manner if we neglect the conduction losses to the substrate and consider only the heat transfer by convection, a situation which reflects better the case of a suspended hot wire. In such situation, the thermal equilibrium leads to:

$$I^2 R_w = h \cdot A_w (T_w - T_f) \quad (4-1)$$

Where I is the electrical current, R_w is the heater resistance, T_w its temperature, A_w its projected surface area. T_f is the fluid temperature and h is the heat transfer coefficient of the wire. The so-called King's law¹²⁶ gives h as a function of fluid velocity v as follows:

$$h = a + bv^n \quad (4-2)$$

where a , b and n are constants, with n being in the order of 0.5 while a and b are determined by calibration.

Taking into account that R_w depends on temperature as follows:

$$R_w = R_{ref} [1 + \alpha(T_w - T_f)] \quad (4-3)$$

Then Then injecting equation (4.2) and (4.3) into (4.1), one finally obtains:

$$a + bv^n = \frac{I^2 R_{ref} [1 + \alpha(T_w - T_f)]}{A_w (T_w - T_f)} \quad (4-4)$$

The latter equation can be rewritten as follows so that to derive the velocity:

$$v = \left\{ \frac{I^2 R_{ref} [1 + \alpha(T_w - T_f)]}{A_w (T_w - T_f)} - a \right\}^{\frac{1}{n}} \quad (4-5)$$

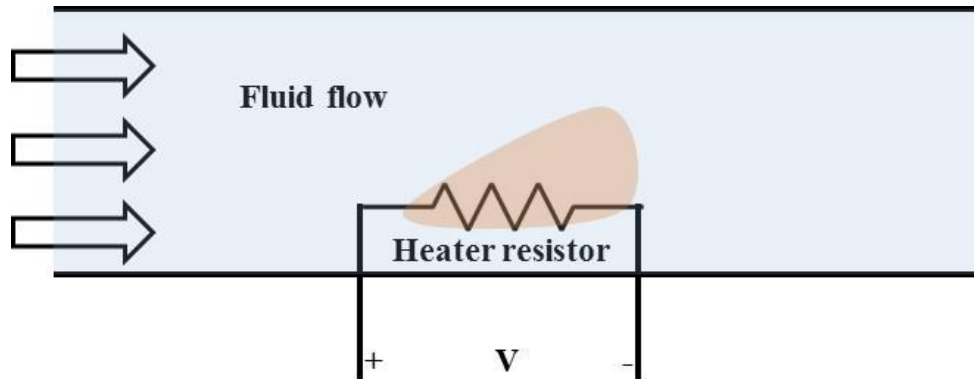


Figure 4-8: Schematic illustration of Hot-wire anemometer flow-rate sensor ⁸²

When considering the contribution of heat conduction to the substrate as well as the real geometry of the heater and its surrounding environment, one needs to proceed with numerical simulations as described in the following sections. However, based on equation (4.5) one can better understand some general statements as exposed here below.

The hot-wire flow-rate sensor can be operated under three operation schemes *i.e.*, constant current, constant temperature difference and constant power mode ^{106,127}.

In constant current mode operation, a constant current is supplied to the heater resistor of a thermal flow-rate sensor. Under no flow, a first equilibrium temperature is reached. When the sensor is submerged in a moving fluid, the temperature of the resistor decreases which will lead to a resistance variation. The temperature decrease magnitude increases with the fluid velocity. Thus, the fluid velocity can be deduced based on the heater resistance variation as a function of the fluid flow. On the other hand, constant temperature difference operation scheme involves in operating a thermal flow-rate sensor by maintaining a constant temperature difference between heater and fluid. Fluid flow causes a diminution of the heater temperature. As a result, temperature compensation is needed for the heater resistor in order to maintain the constant difference. The amount of power consumption that is required to reach the initial tantamount temperature depends on the fluid flow speed. The velocity of the corresponding fluid can be determined using the feedback signal required to maintain such constant temperature. The third operation method of a thermal flow-rate sensor is the constant power mode. In this method, the fluid velocity is measured based

on the temperature variation of the sensing element while maintaining a constant power supply for heating. For the same power supply, the larger the fluid velocity, the lower the temperature.

(ii) *Calorimetric operation principle*

The calorimetric flow-rate sensor measures the temperature profile around the heater. A fluid flow in a given direction induces an asymmetry of the temperature profile. The profile also depends on the fluid velocity. Measuring the temperature profile hence enables the determination of the fluid velocity. Such sensor contains at least two temperature sensors upstream and downstream of a heating resistor. These two sensors detect the distorted thermal profile around the heater resistor due to the flow velocity. At zero velocity, temperature profile is symmetric in the vicinity of the heater and there is no significant temperature difference between the two sensing resistors. When velocity is introduced, temperature profile around the heater is distorted and the temperature difference between the two upstream and downstream temperature sensors increases. The calorimetric sensor can not only detect the fluid flow-rate but also the direction of the flow as well. A schematic representation of a calorimetric flow-rate sensor is shown in Figure 4-9.

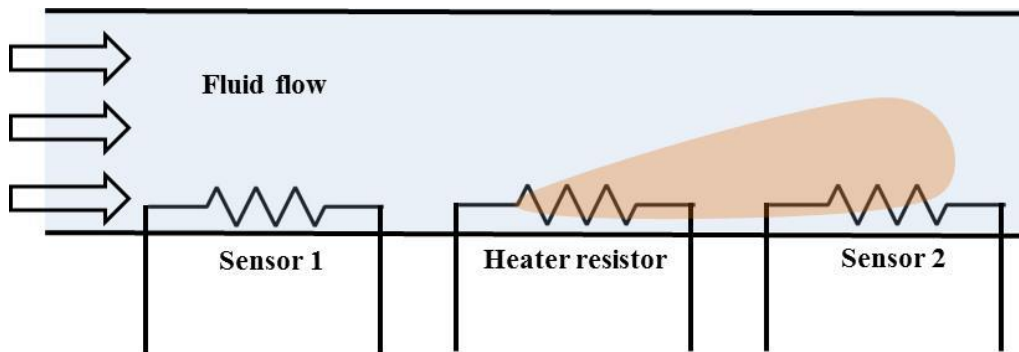


Figure 4-9: Schematic representation of calorimetric operation mode of a thermal flow-rate sensor ⁸²

In general, the turndown ratio of a calorimetric sensor is small. This kind of sensor is more suitable to measure a very low velocity⁷⁸. A calorimetric sensor can provide information regarding velocity until the temperature difference reaches zero between the heater and the sensing resistor. At very high velocity, the upstream or downstream sensor cannot sense heat dissipated from the heater resistor. In this case, the sensitivity range of the corresponding sensor can be extended by varying the distance between the heater and the sensing resistor. The relationship between the maximum velocity that can be sensed by a calorimetric sensor and the distance between the heater and a sensing element can be given by ¹⁰⁶:

$$V_{max} = \frac{2D_t}{\Delta S} \quad (4-6)$$

Here,

V_{max} : maximum velocity (m/s)

D_t : thermal diffusivity of the fluid (m²/s)

ΔS : heating and sensing resistor distance (m)

Therefore, the distance between the heater and the sensing resistor is a governing parameter for a calorimetric flow-rate sensor. The sensitivity can be enhanced to low velocities range by decreasing this distance; and for large velocities by increasing the heater-sensor separation^{82,106,128}.

(iii) *Time-of-flight (TOF) operation principle*

In a Time-of-Flight flow-rate sensor, flow-rate is determined by calculating the travel time of a thermal pulse in a fluid medium over a known distance. The TOF sensor consists of one heater and (at least) one sensing element. The heat pulse is generated from the heater resistor in the surrounding moving fluid and detected by the sensing resistor. A schematic description of the TOF operation mode is presented in Figure 4-10.

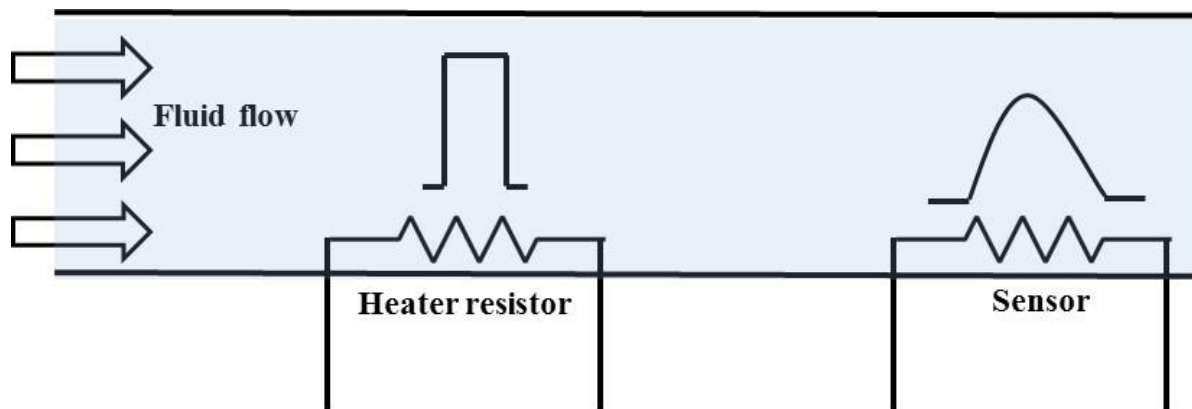


Figure 4-10: Schematic representation of Time-of-Flight operation principle of a thermal flow-rate sensor⁸²

The heater is isolated thermally from the substrate in order to avoid thermal leakage. This is recommended in general for all thermal flow-rate sensors. To determine the travel time of the short thermal pulse from the heater to the detector, several parameters have to be considered: thermal diffusivity and conductivity of the fluid, the ratio of the heater-detector distance and the average flow velocity. Generally, velocity is calculated by dividing the heater and sensor distance by the travel duration of the thermal pulse¹⁰⁶.

$$V = \frac{\Delta S}{\Delta t} \quad (4-7)$$

Here,

V = velocity (m/s)

ΔS = distance (m)

Δt = time duration between the pulse generation and detection

The distance ΔS has to be chosen carefully so as to avoid excessive thermal diffusion during the flight time Δt . Indeed, as depicted schematically in Fig. 4.13, an ideal square-shaped thermal pulse will gradually evolve into a Gaussian-like pulse during the flight path and it will eventually vanish due to lateral heat diffusion. This phenomenon is modeled as follows. If we consider the heater as a line source the thermal distribution can be expressed as a function of distance and time as ⁸²-

$$T(x, t) = \frac{q_0}{4\pi kt} e^{-\frac{(x-vt)^2}{4at}} \quad (4-8)$$

Here,

T = temperature distribution at time t (K)

x = distance between the heater and the considered position (m)

t = time (s)

q_0 = pulse signal input strength

k = thermal conductivity of the fluid (W/m.K)

a = thermal diffusivity (m²/s)

v = average flow velocity (m/s)

The flow-rate meter based on TOF operation principle is mainly used to measure liquid flow-rate. The TOF flow-rate sensors are not widely used in gaseous media due to the large thermal diffusivity of gases ^{82,106,119}.

4.2 Materials and Methods

A study based on numerical simulations and subsequent comparison with experimental results, is carried out to investigate the performances of the different flow-rate sensors under consideration, depending to different parameters, especially the device geometry, the substrate material and power consumption. This study is also intended to anticipate for unexpected behaviors as will be discussed in the next section of results and discussion.

4.2.1 Design summary of thermal Flow-rate sensors with co-integration constraints

As mentioned in Chapter 2, five different versions of the flow-rate sensor have been fabricated. The main difference between those five versions lies in their geometry and the substrate material. The initial prototype of the flow-rate sensor was fabricated on a glass substrate while the four subsequent versions were all made on silicon substrates. Four among the five versions are considered in this section for the purpose of evaluating their characteristics. The schematic diagram of those four versions is shown in Figure 4-11.

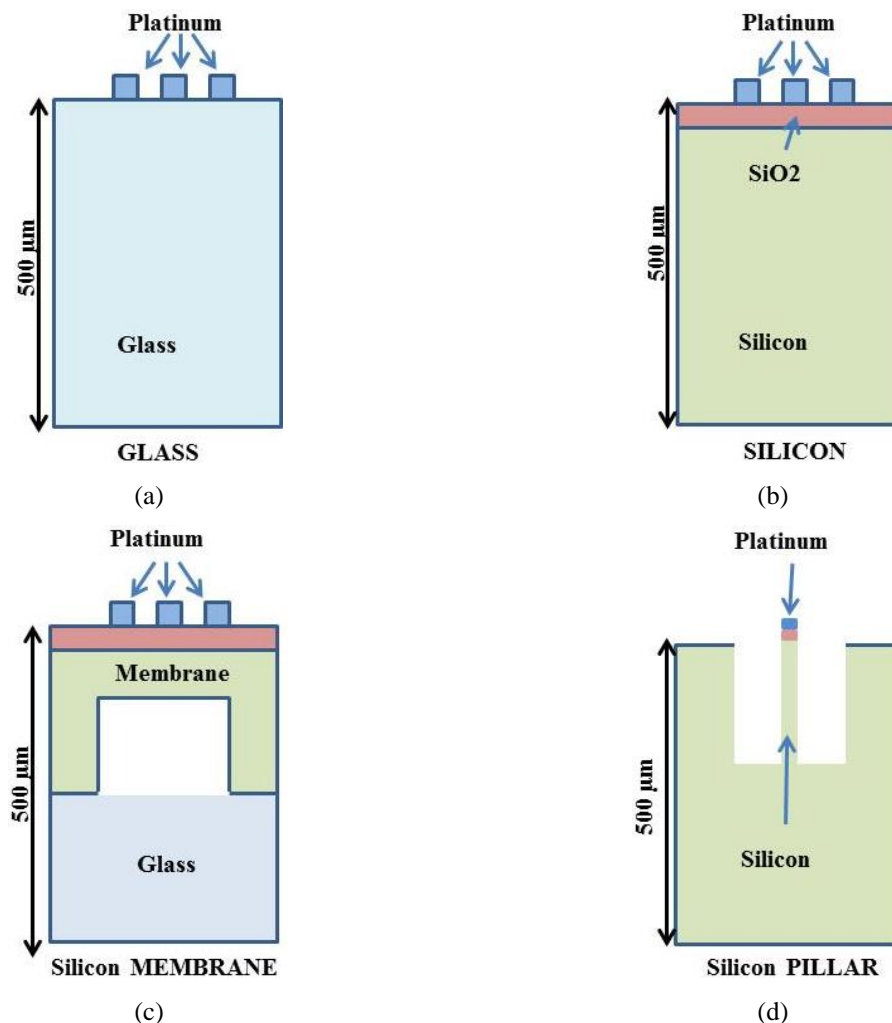


Figure 4-11: The 4 different configurations of the flow-rate sensor- (a) glass substrate, (b) bulk silicon, (c) silicon membrane and (d) pillar structure

It can be observed from Figure 4-11 that the first three versions of the flow-rate sensor have three Platinum (Pt) resistors and the silicon pillar structure has only one Pt resistor. First three prototypes contain

three resistors in order to keep the option for implementing different operation principles. For instance, anemometric operation scheme can be implemented using anyone of the three resistors as a heater. On the other hand, using middle resistor as a heater and the two others as temperature sensors enables the use of the calorimetric mode. Besides, the resistors arrangement of the first three versions is compatible with TOF operation mode as well. The middle resistor can be used as thermal pulse generator and a side resistor, either at the right side of the left side (depending on the flow direction) can be used as sensing resistor. For instance, if the flow direction is from left to right, then the right side acts as the sensing resistor. If the flow is in the opposite direction, the left-side resistor will act as the sensing resistor. Since the sensitivity of a TOF flow-rate sensor depends on the distance between the pulse generator and the detector, a three-resistor device also provides the option for two different sensitivity levels. Indeed, for low velocities, two neighbor resistors can be used. On the other hand, both left and right side resistors can be used to increase the sensor's sensitivity to large velocities.

For the first three versions of the flow-rate sensor, identical resistors dimensions are used ($106 \mu\text{m} \times 10 \mu\text{m} \times 0.34 \mu\text{m}$). The distance between the resistors is $20 \mu\text{m}$.

The ensuing version (pillar) contains only one resistor. Consequently, the latter configuration is compatible only for the anemometric operation principle. The resistor dimensions of the silicon pillar device slightly differ from those of the glass, silicon and silicon membrane based sensors. There are two sub-versions of the pillar structure device, differing in their cavity and resistor width. The cavity dimensions are $100 \mu\text{m} \times 200 \mu\text{m} \times 100 \mu\text{m}$ and $100 \mu\text{m} \times 600 \mu\text{m} \times 100 \mu\text{m}$ while the resistor dimensions are $100 \mu\text{m} \times 10 \mu\text{m} \times 0.34 \mu\text{m}$ and $100 \mu\text{m} \times 5 \mu\text{m} \times 0.34 \mu\text{m}$. It is worth noting that the heater resistor width is an important parameter as will be shown later in the next section of results and discussion. It is worth mentioning that for ensuring long lifetime, we have to keep the flowrate sensor mechanically robust enough. Hence we did not consider fully-suspended thin-film resistors as an option for designing our flow-rate sensor. The main reason is that, contrary to microfluidic devices, water networks not only involve quite large velocities, in the order of m/s, but they also might carry solid particulate matter of various sizes, which can impact the resistor and destroy it if it is too fragile.

Due to lack of time, and in order to facilitate comparison between all versions, all simulation and experimental results presented in the present work are based on anemometric operation mode solely.

4.2.2 Numerical simulation method

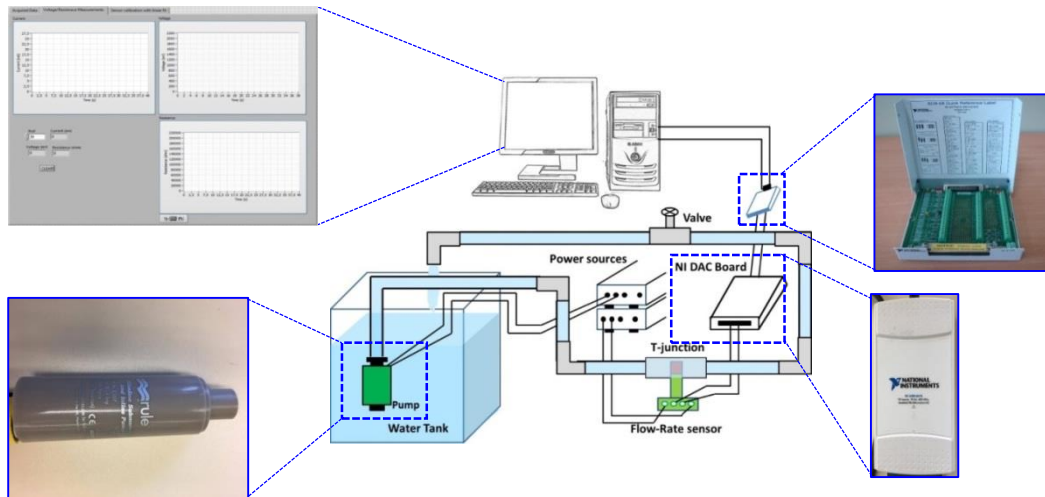
The different device configurations presented in Figure 4-11 are considered first for numerical simulations. Computational Fluid Dynamics (CFD) simulations are carried out based on Finite Element Method (FEM) and using COMSOL Multiphysics 5.2a. Material properties are imported from COMSOL

material library and conjugate heat transfer physics is used to account for heat transfer both in the solid and fluid media. As shown in Figure 4-11, the substrate thickness is 500 μm for all cases. When glass is used as substrate material, no insulation layer is introduced between the heater and the substrate, since glass has a low thermal conductivity compared to other device materials. When the substrate is not made of silicon, a 450-nm thick SiO_2 insulation layer is added under the heater resistor in order to reduce thermal conduction leakage. For membrane structure, the platinum resistor is fabricated on the top of a silicon membrane. The cavity depth under the silicon membrane is 430 μm and the empty space inside the cavity is considered as vacuum. The membrane is considered as a possible solution to reduce thermal leakage. The device first version, based on a glass substrate, shows a better thermal efficiency due to glass low thermal conductivity. As already discussed in Chapter 2, because silicon is necessary for co-integration of the different sensors on the same chip, similar thermal performance is then targeted, even when using high thermal conductivity materials like silicon. Indeed, silicon's thermal conductivity is approximately 100 times larger than that of glass^{129,130}. Other configurations, such as a heating resistor on top of a thin silicon pillar, are also considered for the same purpose, in this case through a reduction of the resistor-substrate contact area. The pillar is located in the middle of a cavity. A parametric study is conducted to optimize the pillar, resistor and cavity aspect ratio. The cavity depth and the width are varied from 50 μm to 300 μm and from 100 μm to 1000 μm , respectively. The length and height of the silicon pillar is equal to the cavity length and height. The resistor and pillar have the same length and width since the resistor is deposited on top of the pillar. The length is fixed at 100 μm and the width is varied from 5 μm to 10 μm . In order to experience the maximum velocity, the sensor is located at the pipe symmetry axis because of the parabolic velocity profile. A large fluidic domain, compared to the sensor size, is considered in the simulation so as to avoid edge effects.

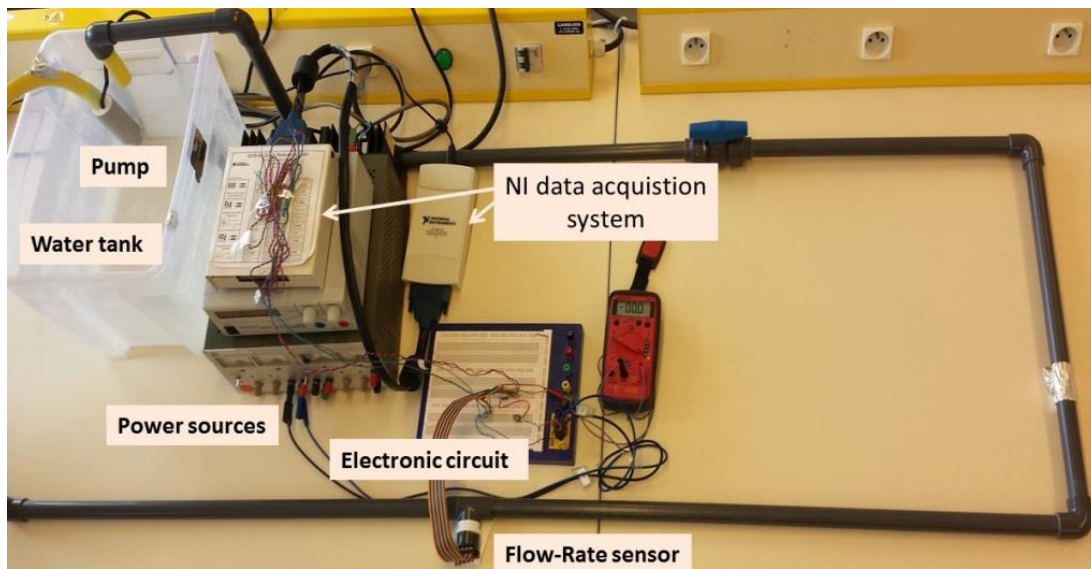
4.2.3 *Experimental Setup for calibration of the Flow-Rate Micro-sensors*

Regarding the experimental part of our study, we already presented in Chapter 2, the fabrication details of the different versions of the MPSC, which includes the flow-rate sensors. In the present section, we will focus on the description of the experimental setup that we developed and used for the purpose of measuring the characteristics of the fabricated flow-rate sensors.

Figure 4-12(a) and (b) illustrate the whole experimental setup, which can be described in two parts: a fluidic circuits and an electrical circuit.



(a)



(b)

Figure 4-12: (a) Schematic diagram and (b) labelled picture of the experimental setup.

(i) Fluidic circuit

The setup is built using a usual rigid plastic pipe in which the flow-rate sensor is inserted. The inner diameter of the pipe is 22 mm. The flow input and output is connected to the same water reservoir, which can be considered as a closed loop. Several pieces of a similar pipe are used to build the closed water loop. For avoiding turbulent flow at the sensor vicinity, the length of the pipe piece in which the sensor is inserted, is chosen as ten times of its diameter in order to avoid the edge effects and ensure a fully developed established flow regime around the sensor. To connect different parts of the pipe, several 90°-angle elbow-shaped pipes are used and the sensor is placed at the middle position between the two edges of the corresponding pipe. A variable speed water pump is submerged in the water tank and connected to the loop

input. Water velocity can be varied by varying the supply voltage of the pump. The different magnitudes of the flow-rate generated by the pump, for the considered setup and circuit, is first calibrated at different voltage intensities by volumetric measurement. Under a certain voltage supply, the required time was recorded to fill a certain volume of water. Since the diameter of the pipe was known; therefore, the velocity was calculated from the obtained flow-rate value, accordingly. Table 4-2 presents the values of the generated flow-rates obtained at different voltage levels (as well as the corresponding average velocities estimated as the ratio of flow-rate over the pipe cross-sectional area). After this calibration, the actual flow-rate was determined during the experiments simply from the data of the pump input voltage. During the measurements, the process was repeated several times in order to reduce the uncertainty level of the recorded time

Table 4-2: Supply voltage of the pump and the corresponding water flow-rates and average velocities generated by the pump in the considered experimental fluid loop.

| Supply voltage V_{pump} (V) | Flow-rate (liter/minute) | Average velocity (m/s) |
|--|---|---|
| 0 | 0 | 0 |
| 2 | 1.1 | 0.05 |
| 2.5 | 2.3 | 0.1 |
| 3 | 3.4 | 0.15 |
| 4 | 5.9 | 0.26 |
| 5 | 7.5 | 0.33 |
| 6 | 9.6 | 0.42 |
| 7 | 11.6 | 0.51 |
| 8 | 13.9 | 0.61 |
| 9 | 15.3 | 0.67 |
| 10 | 17.8 | 0.78 |
| 11 | 18.7 | 0.82 |
| 12 | 20.7 | 0.91 |

The water reservoir capacity is 20 litres. The same water level, reservoir and loop positions are respected for both pump characterization and sensor response measurement in order to avoid any variation of head loss during the different steps of experimental characterization.

(ii) Electrical circuit

A constant current source is built using an adjustable three-terminal positive-voltage regulator IC device (LM317). The current supply of the constant source is tuned at different intensities by varying the value of a variable resistor, which is placed in series with the reference and load (sensor) resistor. The reference resistor is used to determine the amount of injected current through voltage measurement. For a fixed value

of the variable resistor, the circuit will provide a constant current continuously while the resistance of the sensor's resistor changes according to its temperature. Figure 4-13, shows a schematic of the constant current source circuit. To increase the accuracy of measured data, a 4-probe measurement scheme is used so as to eliminate the parasitic wiring resistance which may vary due to local heating. The two outer ports are used to inject the current and remaining two inner ports are used for data reading of the voltage across the sensor's heater resistance, which is an indication of its temperature and hence of the flow-rate.

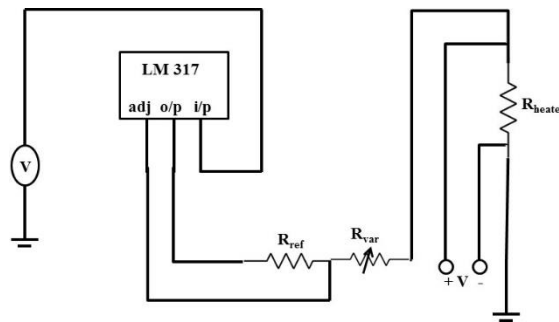


Figure 4-13: Schematic of the constant current circuit source.

The data acquisition system consists of an NI DAQ board and LabView software interface. An extra hardware SCB-68 manufactured by National Instruments was used along with the DAQ board USB-6216. The functionality of SCB-68 board is first to collect the data in analog format from the sensor reading output ports and send those data to the DAQ board connected to the computer. Two input ports of the SCB-68 device were also assigned to monitor the injected current intensity to the sensor and read the voltage across the heating resistor respectively. The USB-6216 board manipulates the data according to the LabView code and visualizes them on the computer screen (Figure 4-12). The LabView interface has been programmed to provide several graphical displays of useful information, such as injected current, voltage across the sensor's resistor, real-time value of the resistor's resistance due to local heating and velocity. This interface also enables recording data during the whole experiment.

The generated programme has three tabs. The first tab (Figure 4-12a) only shows the raw signal of the SCB-68. The acquired signals by these two ports are then manipulated by the formulated code in the LabView programme. The dedicated hardware only can read the voltage from the desired points. Hereafter, the desired information can be obtained from this voltage signal by the programming. The aim of linear regression tab is to determine the linear response of the sensor with respect to the velocities.

The fluid flow velocity and flow-rate are obtained indirectly through a measurement of the sensor's resistor resistance variation. Indeed, the setup measures a change in the resistance value of the device

platinum resistor due to a temperature variation induced by the fluid flow. The relationship between the resistance value and temperature variation can be expressed using the equation:

$$R(T) = R(T_0) \times (1 + \alpha \Delta T) \quad (4-9)$$

Where,

$R(T)$: resistance value at temperature T (Ω)

$R(T_0)$: the reference value of the resistance at the initial temperature T_0 (Ω)

$\Delta T = T - T_0$: temperature variation ($^{\circ}\text{C}$)

α : Resistance Temperature Coefficient ($^{\circ}\text{C}^{-1}$)

For a given fluid velocity, the resistance temperature drop with respect to zero velocity situation is calculated using same equation (4-9). It is related to the fluid velocity by a calibration process. Consequently, a measurement of the resistance value, hence temperature, enables to access the fluid velocity. Note that another initial calibration of the sensor is also required so as to determine the values of both $R(T_0)$ and T_0 .

4.3 Numerical Results and Discussion

In this section, numerical and experimental results will be presented. The numerical parametric study enables the device design optimization before fabrication. Then the optimally designed device is fabricated and experimentally characterized. First, numerical simulation results of each design of the flow-rate sensor will be presented. Then, the corresponding experimental measurement results will be presented for each design. Finally, a comparative discussion will be performed.

4.3.1 Glass substrate based flow-rate sensor

The first version of the flow-rate sensors is based on a glass substrate. The whole simulation domain, including the fluidic domain consists of three different materials- water, glass and platinum. Figure 4-14 shows the simulation domain of the glass substrate flow-rate sensor.

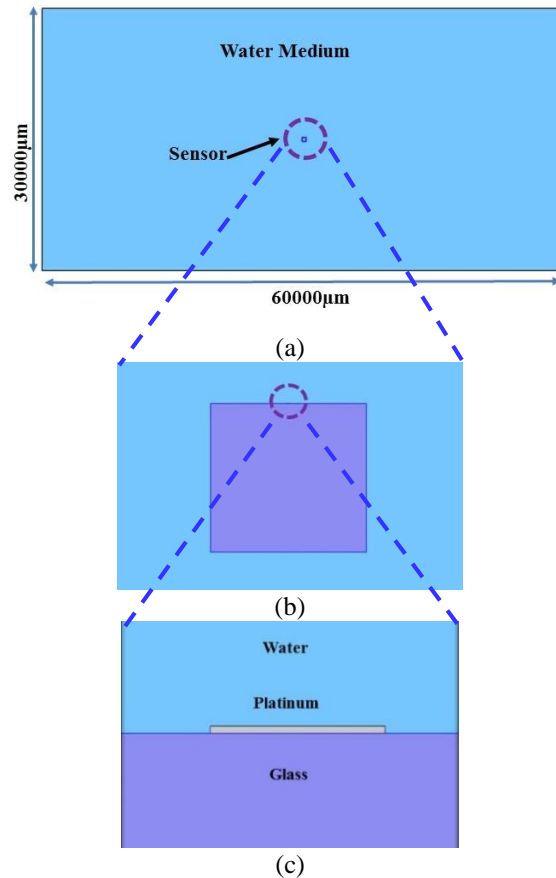


Figure 4-14: Geometry of (a) the whole simulation domain, (b) the sensor chip and (c) the platinum sensing element on top of a glass substrate.

Boundary conditions have to be defined for both the solid and fluid domains. For heat transfer, the left side of the fluid domain is set at a constant temperature, ambient temperature for instance (293.15K). A continuity condition is set at the other boundaries (“outflow” in COMSOL terminology). The platinum resistor is defined as the heat source with a volumetric power density. The heat source volumetric power density q is calculated using the equation:

$$q = \frac{P}{V} \left[\frac{W}{m^3} \right] \quad (4-10)$$

Where,

P : dissipated electric power (W)

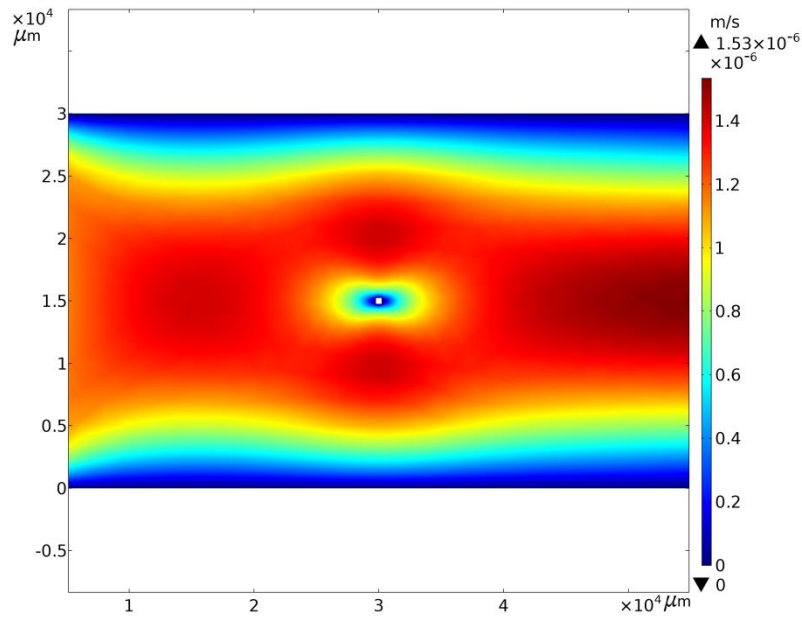
V : the heating resistor volume (m^3) (estimated as $106 \times 10 \times 0.34 \mu m^3$)

Default values of P and V are 10 mW and 360,4 μm^3 , respectively.

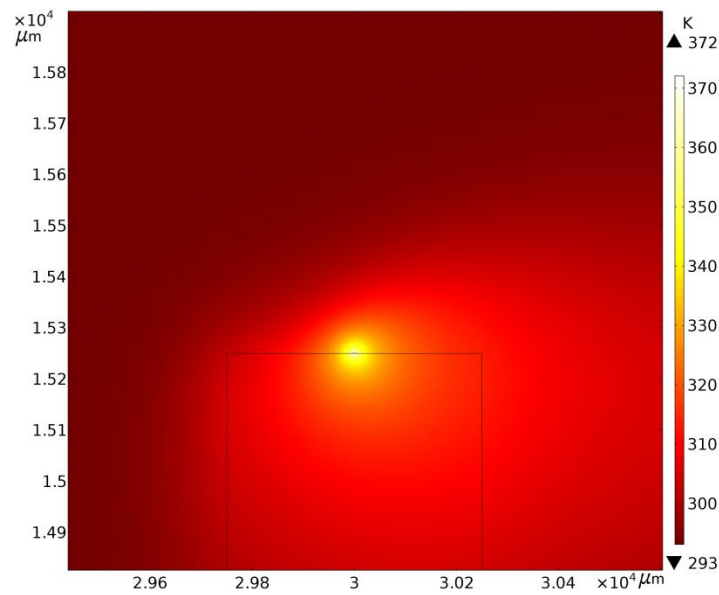
For mass transfer physics, a laminar flow is considered. The left edge of the fluid domain is defined as the flow inlet with a constant velocity profile and the right edge as flow outlet. The top and bottom sides are defined as symmetry axes. Exterior edges of the sensor chip are defined as walls with no-slip conditions. Simulations are done at 10 mW power supply with a velocity ranging from 10^{-6} m/s to 10 m/s. The steady state temperature of the heater resistor is calculated as a function of the fluid velocity. In the following, results will be presented using a normalized temperature \bar{T} . The normalized temperature is defined as the ratio between the temperature difference of the heater and the ambient temperature under flowing and non-flowing condition. The heater and ambient temperature difference under no-flow condition, i.e for zero fluid velocity, is called ΔT_{\max} and the same temperature difference for a given velocity is defined as ΔT . Consequently,

$$\bar{T} = \Delta T / \Delta T_{\max} \quad (4-11)$$

According to this definition, \bar{T} ranges between 0 and 1. Normalized temperature is used in order to have comparable values for all considered sensors designs independently of the absolute temperature reached by each device. Indeed, the maximum temperature of each design under a given power supply due to Joule self-heating can vary in a wide range.



(a)



(b)

Figure 4-15: The picture of (a) velocity profile and (b) temperature profile of the glass-based flow-rate sensor exported from COMSOL

Figure 4-15(a) and (b) illustrates the velocity and temperature profiles for the glass substrate device. We observe a zero velocity at the top and bottom edges of the fluidic domain (Figure 4-15(a)). This is consistent with no-slip condition at the pipe boundaries. Velocity is maximal at the sensor chip vicinity and the fluidic domain outlet. On the other hand, the maximum temperature is observed at the heater resistor position and the temperature field around the heater is distorted according to the flow direction (here to the right).

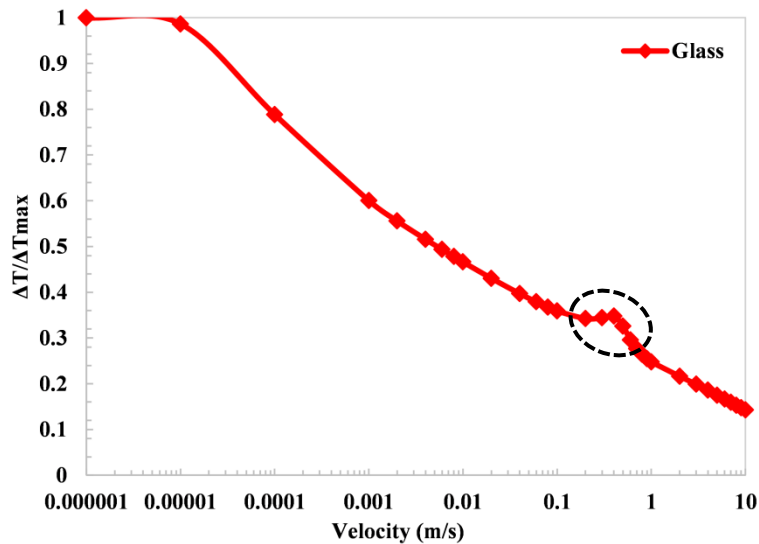


Figure 4-16: Normalized temperature of the glass based sensor versus fluid velocity.

The sensor response as a function of the fluid velocity is plotted in Figure 4-16. For very small velocities, from 10^{-6} m/s to 10^{-5} m/s, no temperature decrease of the sensor is observed. The fluid flow cooling effect is negligible. On the other hand, for large velocities, larger than 10 m/s, normalized temperature goes toward zero, *i.e.* the resistor temperature goes towards the fluid ambient temperature. For intermediate velocities, from 0.0001 m/s to until 10 m/s, the temperature of the heater resistor decreases gradually and exhibits an almost linear trend (with the logarithmic scale on the velocity axis). From 10^{-5} m/s to until 10^{-3} m/s the non-dimensional temperature value decreased largely. In this whole range, a monotonous temperature decrease is observed. For certain velocity values, around 0.7 m/s, the sensor exhibits inconsistent thermal behavior with respect to velocity, which can be seen anomalous *a priori*. Indeed, instead of a temperature decrease due to a fluid velocity increase, the heater temperature increases. This discrepancy is marked with a blue circle on Figure 4-16. A detailed calculation of the fluid velocity field around the sensor chip provides an explanation of this apparent inconsistency. Indeed, due to the sensor chip geometry, at this velocity range, a reverse flow is generated at the resistor vicinity. A detailed explanation regarding this reverse flow and its effects on the sensors thermal response is presented at the end of this section.

4.3.2 Silicon substrate based flow-rate sensor

The physical structure of the flow-rate sensor based on bulk silicon is very similar to that based on glass, except for a thin insulation layer. Indeed, a 450-nm thick SiO_2 layer is inserted between the platinum resistor and the silicon substrate in order to reduce the conduction heat leakage.

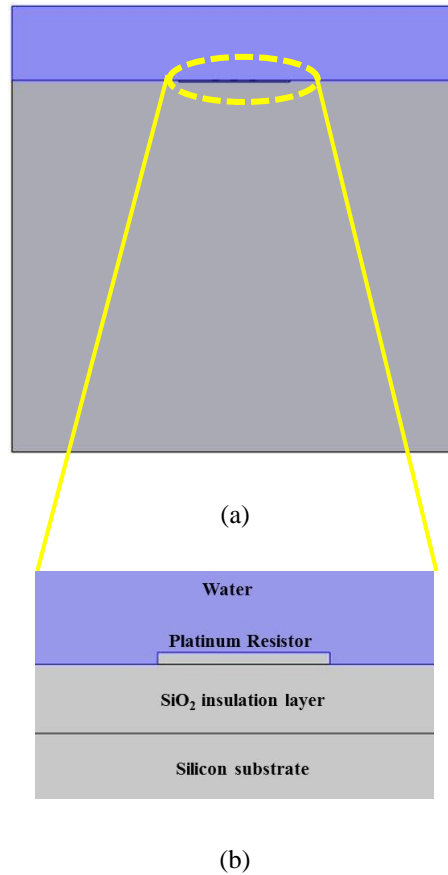


Figure 4-17: (a) Geometry of silicon substrate flow-rate sensor, and a (b) zoom picture of the platinum resistor and SiO₂ insulation layer

Figure 4-17 illustrates the geometric view of the silicon substrate flow-rate sensor. The same boundary conditions as previously are used for numerical simulations.

The velocity profile and temperature distribution around the sensor depend on the flow velocity. For a non-flowing, stationary fluid, *i.e.* when $v = 0$ m/s, the temperature profile around the heater is symmetric. The calculated temperature profile for bulk silicon flow-rate sensor is presented in Figure 4-18 under zero velocity. We observe no distortion of temperature distribution.

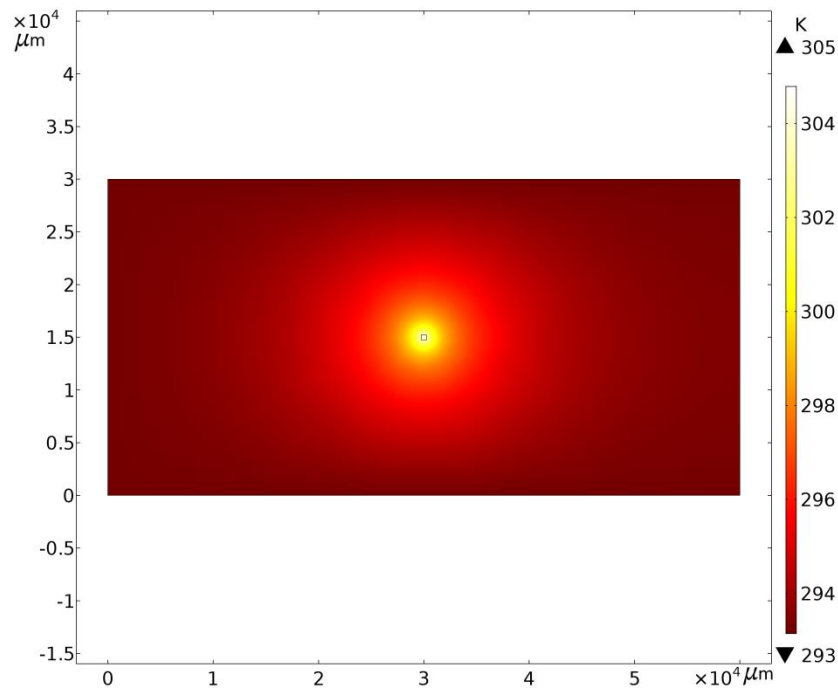


Figure 4-18: Temperature profile of the silicon based flow-rate sensor at $v = 0$ m/s.

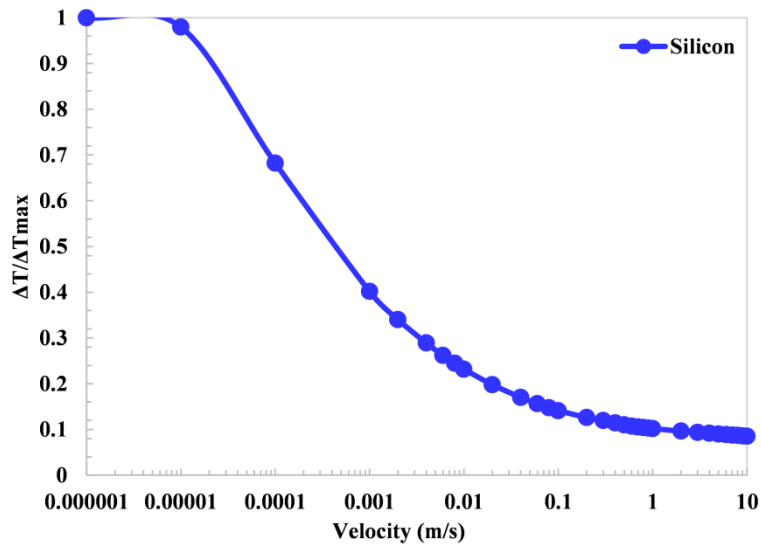


Figure 4-19: Silicon substrate flow-rate sensor's response versus the water velocity.

Silicon-based sensor exhibits a similar response profile to glass based sensor with respect to velocity. The normalized temperature variation of the silicon device reported in Figure 4-19 shows a similar trend but significantly different values for a given velocity. Indeed, the device temperature decreases more rapidly for silicon base device. For instance, within the velocity range from 0.1 m/s to 10 m/s the thermal variation is less than 0.1. The sensor is almost saturated for a fluid velocity of 0.1 m/s and hence not very sensitive

to this velocity range. Another view of this is that the velocity range is limited with this silicon-based sensor compared to the glass-based sensor.

4.3.3 Silicon membrane based flow-rate sensor

In this version, a silicon membrane is used as the substrate for the platinum heater. Then the membrane is deposited on a glass substrate. The thickness of the membrane is 70 μm . Contrary to bulk silicon device, no SiO_2 insulation layer is inserted between the platinum resistor and silicon substrate. The cavity below the membrane is considered as vacuum to enhance the thermal insulation between the heater and the substrate, which reflect reality actually, since this cavity is obtained from silicon-to-glass wafer bonding under vacuum environment. The physical structure of the membrane-based flow-rate sensor is shown in Figure 4-20.

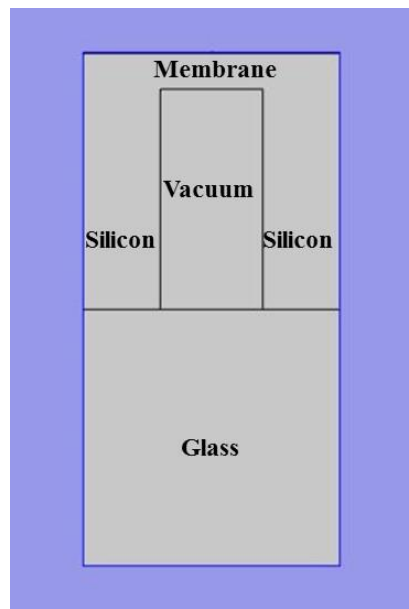


Figure 4-20: Membrane structure flow-rate sensor

A zoom on the platinum heater is not shown here since its structure is identical to that of bulk silicon device (Figure 4-17(b)).

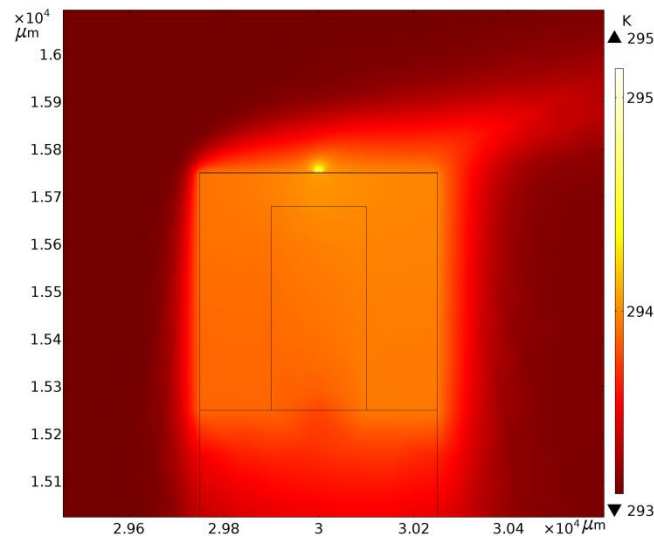


Figure 4-21: Temperature field around the membrane flow-rate sensor for a fluid velocity of 0.001 m/s.

We show in Figure 4-21 the temperature field around the membrane-based flow-rate sensor under low velocity. Due to the low velocity (0.001 m/s in this case), the temperature field is distorted far from the heater while it is almost not affected at the heater vicinity.

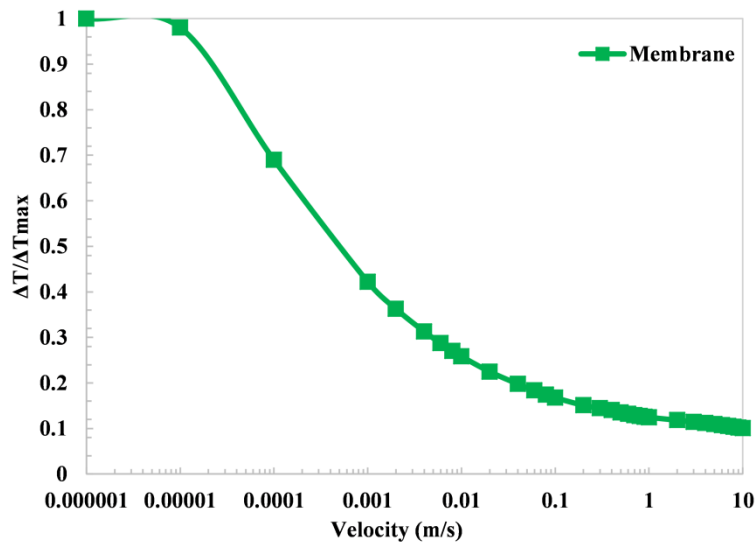


Figure 4-22: Membrane-based flow-rate sensor response with respect to the velocity

We show in in Figure 4-22 the non-dimensional temperature variation of the same device. . No significant difference is observed between bulk silicon and silicon membrane devices (this can be confirmed by plotting the two curves on the same graph, not shown here). Indeed, membrane device shows a large temperature variation between 0.00001 m/s and 0.1 m/s and is almost saturated for velocities larger than 0.1 m/s. Therefore, this device also will not be suitable for the velocity range between 0.1 and 10 m/s, which is the most relevant for our work.

4.3.4 Pillar structure flow-rate sensor

At this stage, a different strategy is adopted to enhance the heater thermal insulation. The heater resistor is deposited on the silicon substrate. Then, a cavity is etched around the resistor to reduce the resistor-substrate contact. The resulting device consists of a heating resistor on top of a silicon pillar. In addition, an insulation layer is used between the platinum heater and the silicon pillar. A schematic representation of this device is shown in Figure 4-23.

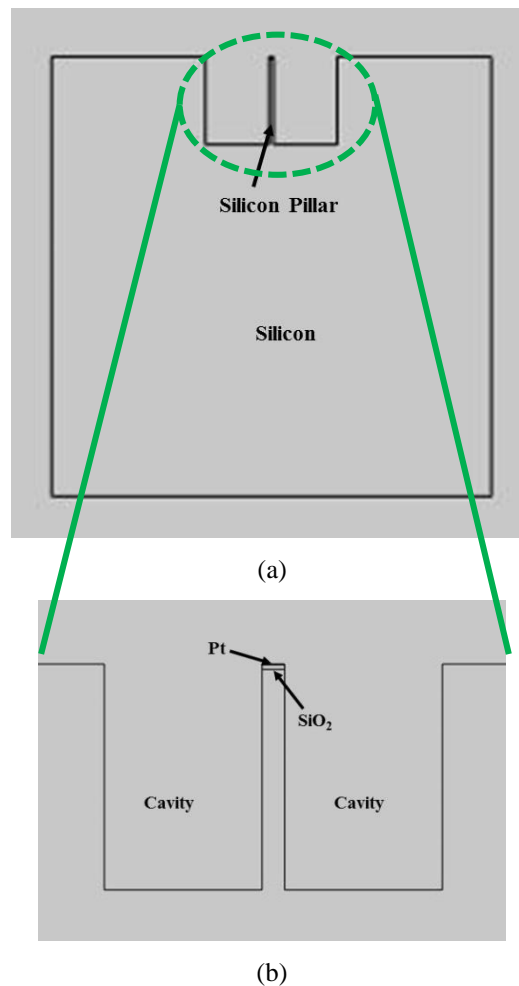


Figure 4-23: The pillar based flow-rate sensor geometric configuration.

Comparatively, this version of the flow-rate sensor exhibits a better sensitivity than bulk silicon and silicon-membrane devices. Its temperature variation with respect to velocity is close to that of glass-based device. Because of these promising results, further parametric studies are conducted to optimize the pillar-based device. Several parameters are investigated: the cavity depth and width, the pillar width and height, and the resistor width. The considered parameters and their variation range in this parametric study are provided below:

Cavity width: 100 μm , 150 μm , 300 μm , 500 μm , 1000 μm ,

Cavity depth = Pillar height: 50 μm , 100 μm , 300 μm ,

Pillar width = Heater resistor width: 1 μm , 2 μm , 5 μm , 10 μm .

All simulations are performed for a 2-D configuration.

Contrarily to the membrane-based device, the pillar device cavity is filled with water since it is in contact with the main flow. The temperature profile of the pillar-based flow-rate sensor at 0.04 m/s is shown in Figure 4-24.

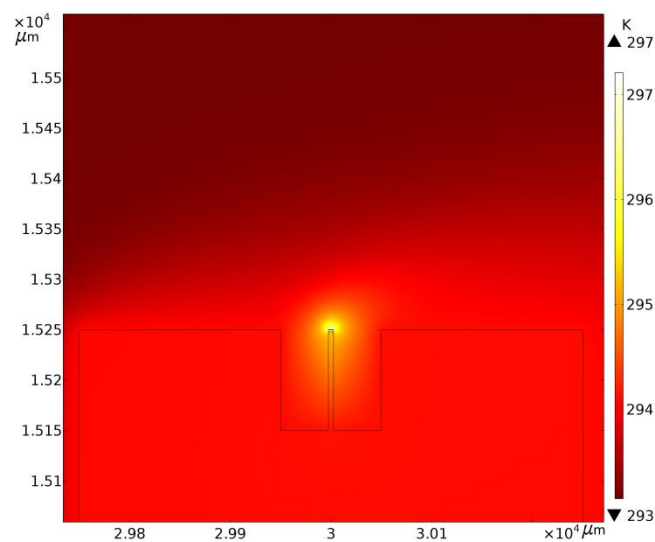


Figure 4-24: The temperature field of the pillar flow-rate sensor at 10 mW power supply at a velocity of 0.04 m/s. In this case, the cavity dimension is 150 x 100 μm and the resistor width is 5 μm .

The temperature variation of the silicon pillar heater is similar to the glass-based flow-rate device. In the low-velocity region, the normalized temperature of the pillar device slightly differs from the glass based sensor. On the other hand, it shows a significant sensitivity difference to water velocity in comparison with the silicon and membrane devices. The pillar device normalized temperature is plotted in Figure 4-25 as a function of velocity.

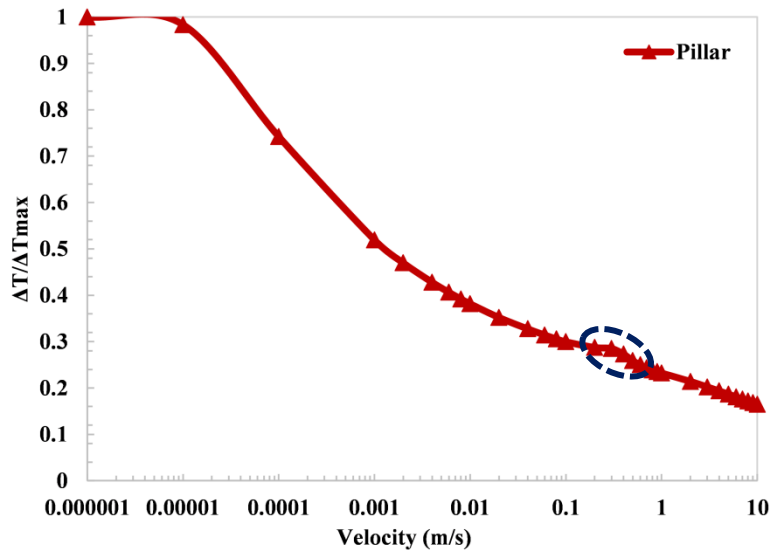


Figure 4-25: Pillar structure flow-rate sensor response with respect to the velocity

The relevant velocity range for water networks is from 0.1 m/s to 10 m/s. For the present device, we observe that \bar{T} variation is 0.2 in this range. It is 0.25 for the glass-based device. Consequently, this pillar device is a promising silicon-based alternative to the glass-based flow-rate sensor.

As mentioned previously, a parametric study is conducted to enhance further this device performance. First, the heating resistor width is varied while all other properties are unchanged. The cavity depth and width are fixed at 300 μm and 150 μm , respectively. Resistor widths from 1 to 10 μm are considered for all configurations (pillar, glass, silicon and silicon membrane devices). For all devices, a sensitivity increase is observed when the resistor width is decreased. In the following, for the sake of simplicity, the parametric study is reported for the most promising configuration only, namely for the pillar device. This parametric study is carried out for a 10 mW power supply and a velocity range from 10^{-6} m/s to 10 m/s. We show in Figure 4-26 the sensor response as a function of velocity for different resistor's widths.

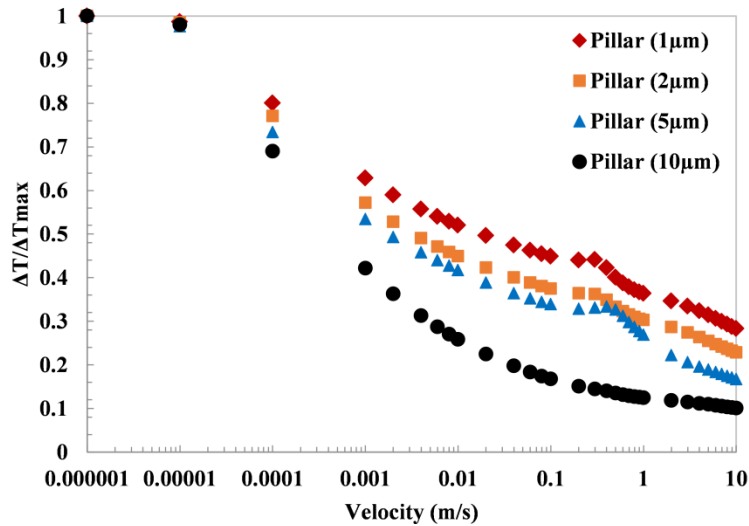


Figure 4-26: The pillar device sensitivity to the velocity at different resistor width

It can be observed that the smaller the resistor width the better the sensor response and turndown ratio. Temperature decreases as a function of velocity for all width values. In addition, the temperature drop for a given velocity is smaller for smaller sensor width. This means the small width sensors will be saturated only at larger velocities than 10 m/s, thus sensitive to the largest velocity ranges. Consequently, from a thermal point of view, the smaller the sensor width the better. However, the considered devices are subject to other constraints, such as mechanical and fabrication constraints as well as robustness requirements. Although 1 μm and 2 μm-wide resistors exhibit better thermal responses, their small size is less convenient for the considered fabrication process and this decreases their robustness for instance in case of waste water operation medium which can contain solid particles. Consequently, the 5-μm-wide resistor is preferred and will be considered in the following.

At this stage, the cavity width is varied between 150 and 1000 μm, while its depth and the heating resistor width are fixed at 300 μm and 5 μm, respectively. We plot in Figure 4-27 the sensor's response with respect to velocity for different cavity depths. No significant change in the thermal response is observed. At the low velocities, up to 0.001 m/s and velocities larger than 2 m/s, the different curves cannot be distinguished. A small but negligible difference is observed for intermediate velocities between, 0.001 and 2 m/s, mainly for the 150-μm wide cavity. Consequently, sensors prototypes with two different cavity widths, 200 μm and 600 μm, have been fabricated.

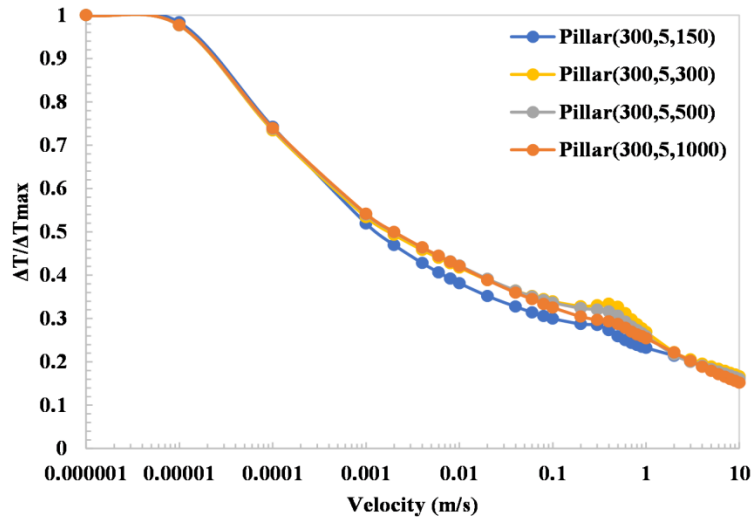


Figure 4-27: Pillar structure flow-rate sensor response as a function of fluid velocity for different cavity depths. Numbers between parentheses in the legend indicate the pillar height (equal to the cavity depth) and width then the cavity width, respectively.

Finally, the cavity depth is varied between 50 μm and 300 μm . The resistor (and pillar) width is still fixed at 5 μm and the cavity width is still 150 μm . The resulting responses are shown in Figure 4-28.

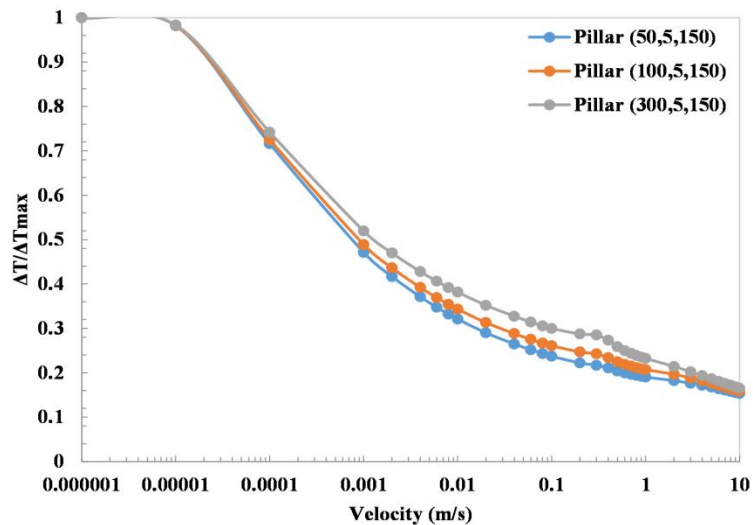


Figure 4-28: Pillar flow-rate sensor response as a function of velocity for different cavity depths.

We observe that, for a given velocity, a deeper cavity leads to a smaller temperature drop thus to a larger turndown ratio. For the fabricated prototypes, a 100- μm -deep cavity is considered.

4.3.5 Reverse Flow

We have already noted on Figure 4-25 a discrepancy of the sensor response, indicated by black dashed circle. The same type of discrepancy is observed in Figure 4-26, Figure 4-27 and Figure 4-28. Instead of a monotonic temperature decrease when the fluid velocity increases, we observe an increase of the sensor temperature for fluid velocities between 0.1 and 1 m/s. We revealed through additional numerical simulations that this apparent inconsistency happens due to “a reverse flow” observed locally at the heater vicinity in this velocity range. The main water flow is heated by the heating resistance after a first pass. For a specific velocity range, and due to the device geometry, hot water is carried back from the heater downstream and induces an increase of the sensor’s temperature. As a result, a velocity increase induces a heater temperature increase rather than the opposite. At 0.3 m/s and 0.4 m/s, the pillar and glass based flow-rate sensors show this inconsistent response. The heater temperature of the glass substrate flow-rate sensor is tabulated in Table 4-3 for a velocity range from 0.2 m/s to 0.5 m/s. It can be seen that when the velocity increases from 0.2 m/s to 0.3 m/s, the heater temperature value is increased rather than decreased. The heater temperature recovers the usual behavior, *i.e.* a decreasing temperature, when velocity exceeds 0.4 m/s. The reverse flow can be observed on the simulated velocity field around the device. We show in Figure 4-29 (a) and (b) both the normal flow velocity field and the reverse flow velocity field in the case of pillar structure flow-rate sensor. We also show in Figure 4-29(c) the temperature profile in the presence of a reverse flow. We clearly observe that the temperature profile is distorted in the opposite direction to the main flow. It is worth noting at this stage that the main stream direction is left to right. In the absence of a back flow, the temperature profile is distorted accordingly and the largest temperatures are observed downstream, *i.e.* on the right side of the heater. A similar reverse flow is observed for bulk silicon and membrane-based sensors. However, in these cases, reverse flow fluid is not hot enough to increase the heater temperature because of lower initial Joule self-heating and larger thermal leakage through the substrate.

Table 4-3: Glass-based flow-rate sensor heater temperature variation with respect to velocity

| Velocity (m/s) | T_{heater} (K) |
|-----------------------|-------------------------------|
| 0.2 | 300.49447 |
| 0.3 | 300.65392 |
| 0.4 | 300.53829 |
| 0.5 | 299.93127 |

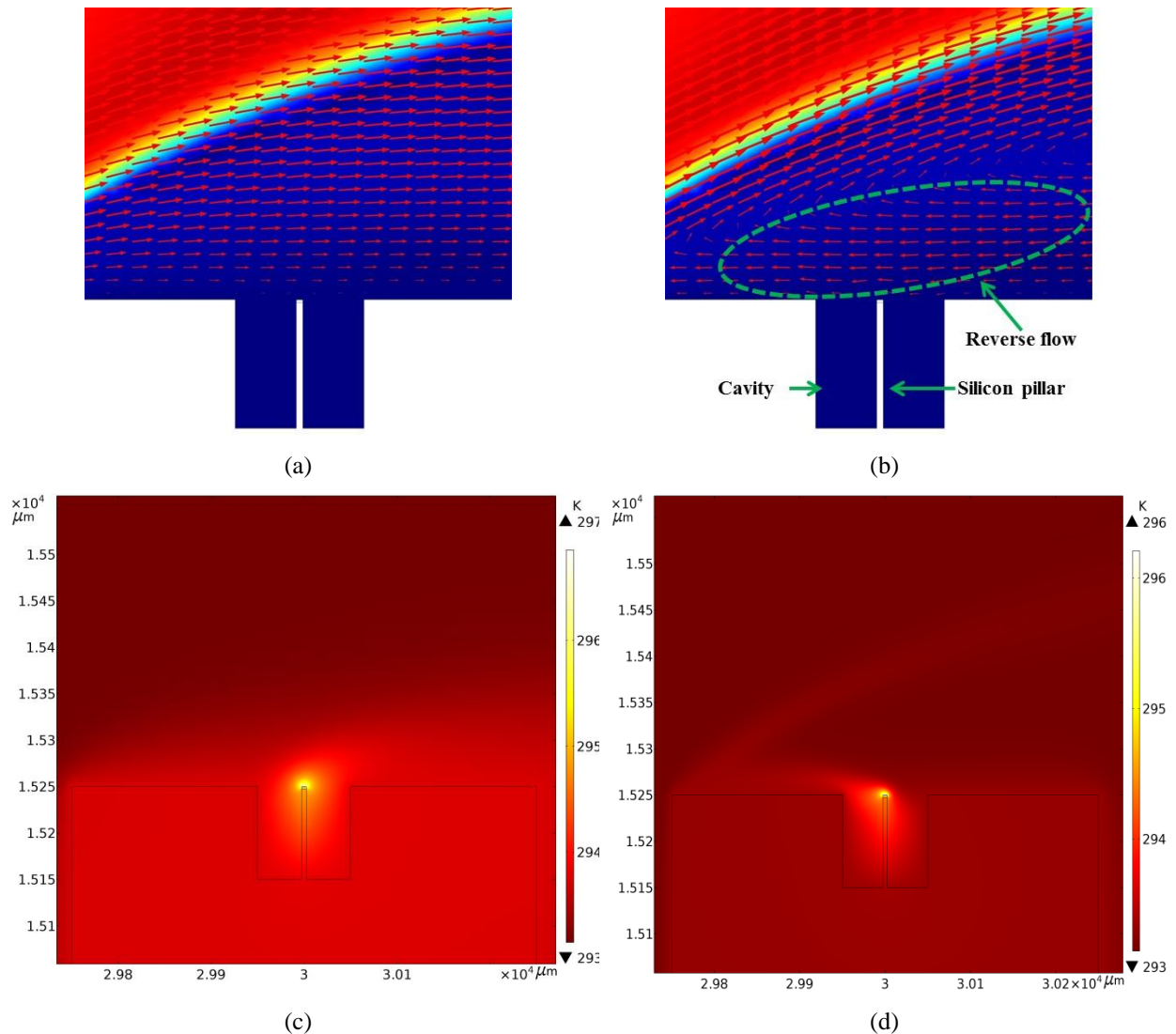


Figure 4-29: (a) Normal velocity profile for different fluid velocities, (b) reverse flow at the resistor vicinity causing the anomalous thermal behaviour within the velocity range highlighted by black circles in Figure 4-16 and Figure 4-25, (c) normal temperature profile and (d) the effect of reverse flow on the sensor temperature profile (flow direction is from left to right).

In order to have a consistent sensor response, the reverse flow has to be suppressed or, at least, reduced. This can be done through a geometric optimization of the sensor node. The height and the edge curvature of the sensor node are modified accordingly. Different CFD simulations are performed to find a satisfactory geometry. A representation of the schematic simulated sensor node and a real sensor node are shown in Figure 4-30(a) and Figure 4-30(b), respectively. The circle in Figure 4-30(a) indicates the location of the sensor chip with respect to the node head.



Figure 4-30: (a) The schematic diagram of the sensor node with dimensions and (b) photo of the real sensor node embedding the MPSC.

According to CFD simulations, it was found that the reverse flow can be minimized if the sensor node is inserted with an incidence angle between 10° and 15° with respect to the normal and sharp edges are avoided. Two chamfer shapes were considered for the sensor node edges in numerical simulations. A schematic of the sensor node position, the angle and the considered chamfer shapes are shown in Figure 4-31(a), (b) and (c).

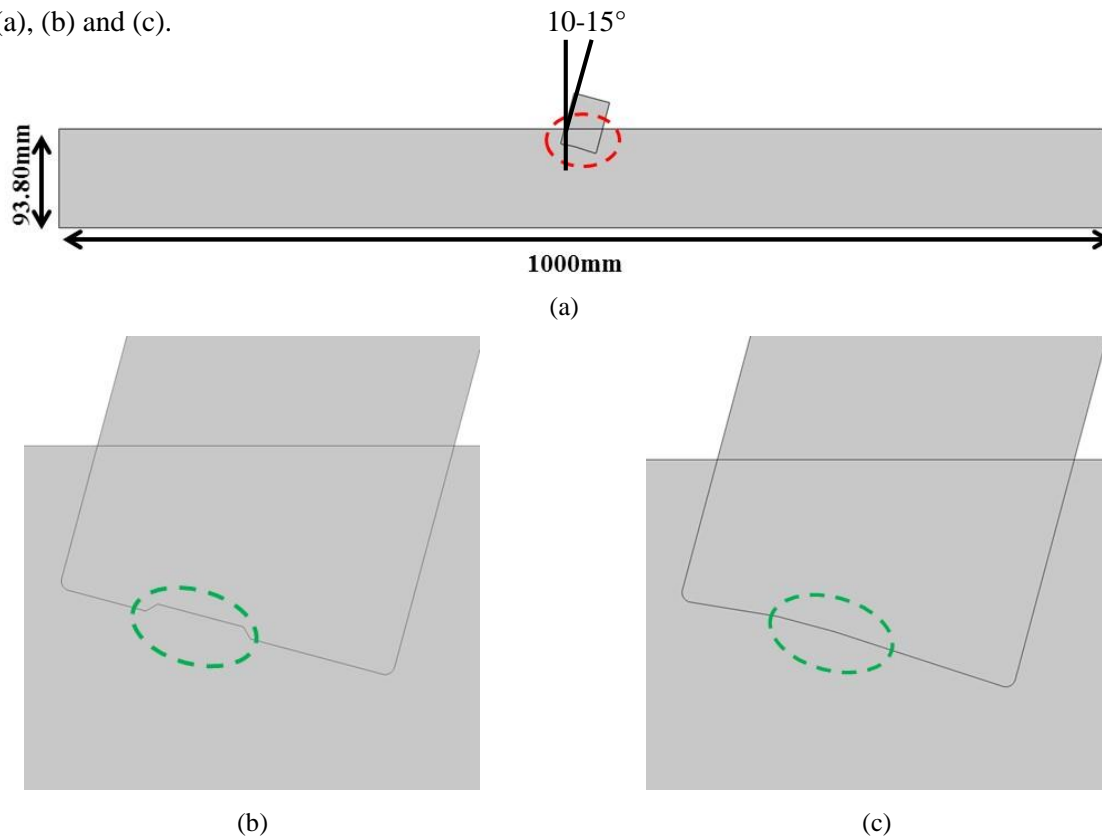


Figure 4-31: (a) The picture of the round-edged sensor node tilted at 15° with respect to the normal and inserted into a water pipe, (b) the sensor node head chamfered with a 0.5 mm radius and (c) 1 mm radius.

In order to study the velocity profile around the sensor chip, the velocity values were determined from the sensor node head's border until the 3 mm distance with a step of 0.5 mm in negative Y-axis direction (Figure 4-32).

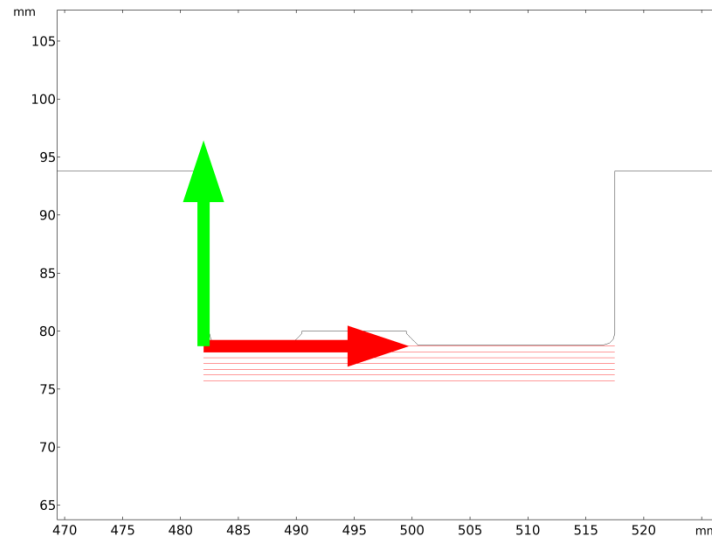
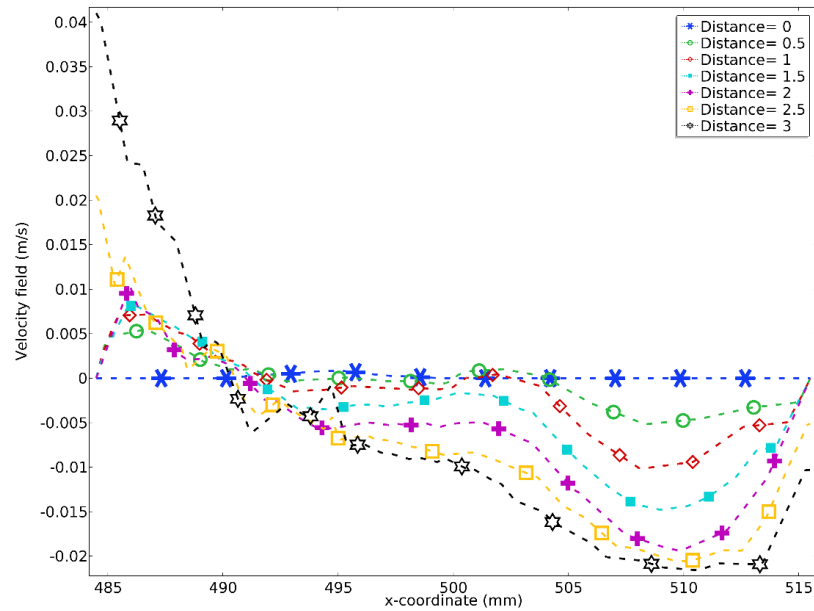
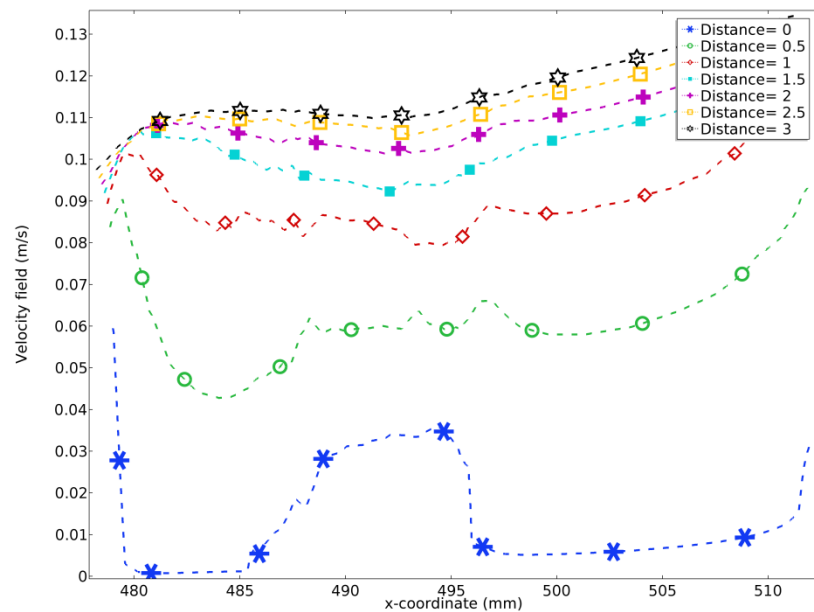


Figure 4-32: Illustration of the sensor node head and the region that was considered for extracting the velocity field in X-coordinate. Parallel red lines (2-D cut line) represent the extent of the region and they have uniform distance (0.5 mm) between them.

It has been observed from the simulation results that inserting angle and the edges shape have more impact on velocity field near to the sensor chip in comparison with chamfer radius. Reverse flow can be minimized significantly by inserting the node in tilted condition with round edges. Such arrangement gives almost similar velocity profile around the sensor node with 1 mm and 0.5 mm chamfer radius. Therefore, two cases are presented in Figure 4-33 under 0.1 m/s velocity to demonstrate relative depiction. Figure 4-33(a) shows the velocity field when the old node is used and in Figure 4-33(b) illustrates the velocity for the proposed modified structured node. It can be seen from Figure 4-33 (a) that all the considered distances experience negative velocity. Further, no velocity has been observed at the border of the node head (at 0 mm distance). On the other hand, the modified sensor node does not experience any negative flow at any distances when it has round curvature head along with chamfer notches in the allocated space of the chip (Figure 4-33(b)). Moreover, this structure eliminates the zero velocity problem at the sensor vicinity, which will improve the sensor's sensitivity at the low-velocity range. The presented velocity field in Figure 4-33(b) involves, in particular, a sensor node whose chamfer radius is 1 mm. Similar velocity field was observed when the chamfer radius reduced to 0.5 mm.



(a)



(b)

Figure 4-33: Velocity field distribution along X-axis direction (for an inlet velocity of 0.1 m/s) around the sensor node at different distances, (a) initial sensor node and (b) modified sensor node with round edged and the chamfered notch of the sensor chip location with 1 mm radius.

Therefore, the reverse flow effect can be fully eliminated, at least within the explored velocity range, by respecting the proposed geometry and tilted inserting position, of the sensor node in the water distribution pipeline.

For deeper analysis, the numerical study was conducted for different values of the inlet velocity- 0.0001, 0.001, 0.01, 0.1, 1 and 10 m/s and the comparison has been made for 0.1 m/s only; since this velocity is relevant to the practical application. It has been observed from the simulation that at inlet velocities lower than 0.1 m/s, the primary sensor node experiences less negative flow and at 0.0001 m/s, there is no observed reverse flow. As the inlet velocity exceeds 0.1 m/s, reverse flow within the considered region increases significantly. However, at maximum velocity 10 m/s, the negative flow has been observed for both sensor nodes. Since this is relatively high velocity in contrast with the real employment medium, therefore the potential issue at 10 m/s can be ignored in practice. In addition, the inclined position of the node reduces reverse flow notably. Hence, higher incidental angle magnitude will lead to a fallacious response from the flow-rate sensor. In order to obtain a reasonable measurement, the velocity should be parallel to the resistor width. The high incident angle of the sensor node with respect to the normal would result in a situation where the velocity cannot be considered anymore as tangential to the sensing element of the sensor. Therefore, the angle should not exceed a certain margin (15° or 20° as a maximum).

4.3.6 Numerical results comparison

At this stage, we undertake a comparison of the different versions of the flow-rate sensor. We plot on Figure 4-34 as a function of the main flow velocity, the numerically obtained temperature variation of the different versions of the flow-rate sensor. Here the pillar device response, with a $5\ \mu\text{m}$ -wide resistor is compared with the bulk silicon, membrane and glass devices.

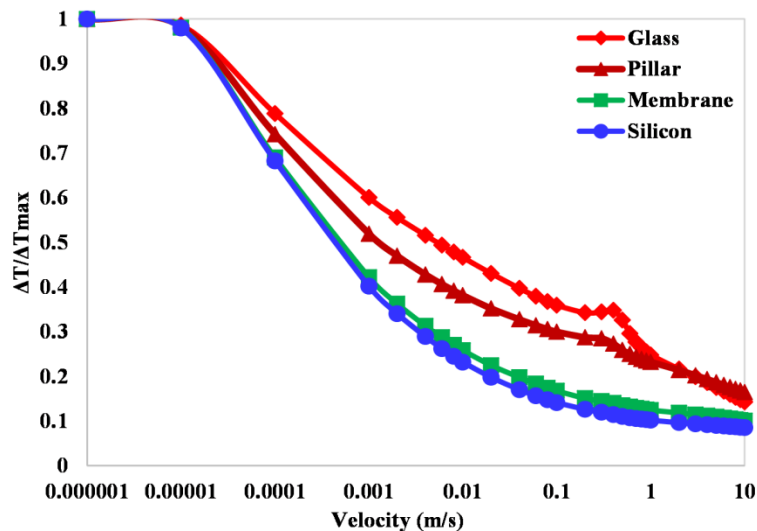


Figure 4-34: Simulation results of glass, pillar, membrane and bulk silicon flow-rate sensor response to the main flow velocity.

In Figure 4-34, the silicon and membrane-based devices exhibit almost similar temperature variations for the whole velocity range. Although the membrane based flow-rate sensor shows a slightly larger

temperature for a given velocity than the bulk silicon device within the velocity range from 0.001 m/s to 10 m/s, this difference is negligible compared to the pillar and glass devices. Among the three silicon-based devices (bulk, membrane and pillar), the pillar structure flow-rate sensor is the only configuration that competes with the glass-based sensor. It even surpasses the glass device response in the velocity range from 0.5 m/s to 10 m/s.

4.4 Experimental Results

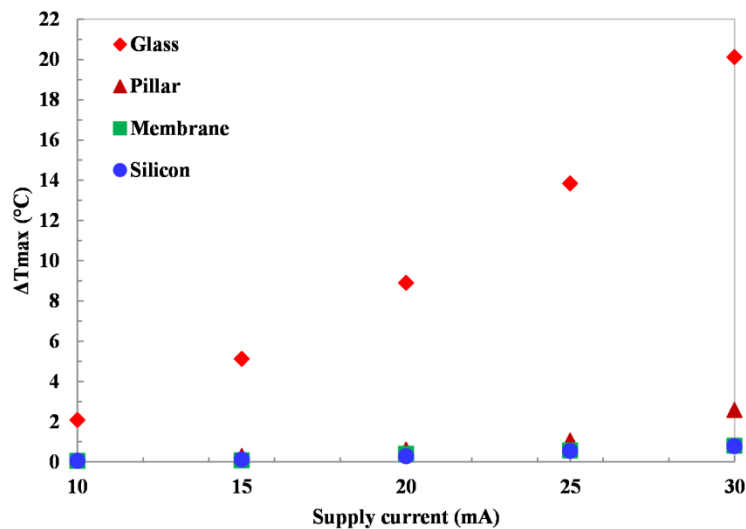
For a thermal flow-rate sensor, the resistor's Joule self-heating is an important parameter. The maximum temperature of the heater resistor under no-flow condition determines the turn-down ratio and the sensitivity of the sensor with respect to velocity. Moreover, the relation between the initial temperature and the power supply indicates the device power efficiency. A large temperature increase at low power consumption leads to a low power consuming thermal flow-rate sensor. Therefore, to determine the considered sensors' energy efficiency, both Joule self-heating and power consumption tests are realized under zero velocity. Results are presented in the following section.

4.4.1 Joule self-heating and Power consumption

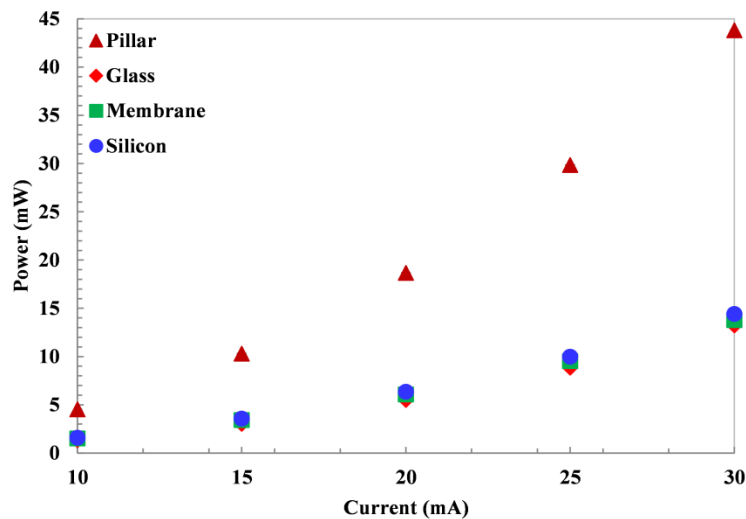
Information on Joule self-heating at the resistor level under no-flow condition helps estimating the sensor's response to a flow velocity and the minimal power supply needed. The sensor is submerged under non-flowing water and supply current is varied from 10 mA to 30 mA with a step of 5 mA. Results of Joule self-heating tests are presented in Figure 4-35(a). The glass sensor exhibits the largest temperature increase, that is, 20.12 °C at 30 mA current supply. Besides, among the silicon-based devices, only the pillar structure device exhibits a significant temperature increase, 2.57 °C at 30 mA supply current. On the other hand, bulk silicon and silicon membrane devices show small temperature increases. These two sensors temperature increase by less than 0.8 °C for 30 mA current supply. Although the three sensors are fabricated on the same substrate material, pillar configuration flow-rate sensor exhibits a significantly larger temperature increase than the silicon and membrane due to an optimized geometry.

Power consumption of the three devices is also calculated for the same current supply range. It is illustrated in Figure 4-35(b). The pillar device consumption is relatively high, up to 43.78 mW for 30 mA current supply. On the other hand, glass, silicon and silicon membrane sensors are three times less power consuming than the pillar configuration at the same current supply. Among these four sensors, glass devices are lowest power consuming within the whole supply current range. This is due to the low initial resistance value of glass device and the high initial resistance value of the pillar device, which are 12.92 Ω and 43.6 Ω , respectively. According to Ohm's law, dissipated power is proportional to the resistance for a given

electrical current (30 mA is considered here as a maximum value). Therefore, the larger the resistance value the larger the power consumption.



(a)



(b)

Figure 4-35: (a) Joule self-heating temperature of the heating resistors at different supply current in non-flowing fluid, and (b) power consumption of the four corresponding sensors.

However, the pillar device heater resistor's width is reduced only by two times (not three) compared to bulk silicon and membrane resistors, which causes a larger resistance value at room temperature and hence the increased power consumption for a given current. Consequently, pillar device is expected to have power consumption two times larger than the other device, since the resistor width has been reduced by factor of

two, not three. This is not what is observed in Figure 4-35(b). Indeed, at the same current supply, a larger resistance value leads to larger Joule heating, hence to a larger equilibrium temperature. Then, additional heating occurs. Joule heating is amplified by two phenomena: i) the temperature increase due to Joule heating induces an increase of the resistance value, hence, to an additional second-order Joule heating and temperature increase; ii) The pillar device resistor contact with the substrate due to the pillar structure reduces heat leakage through the substrate and increases the device equilibrium temperature. This double amplification of Joule self-heating for the pillar device induces a larger increase of the resistance value which strongly depends on temperature, hence leads to larger power consumption. This amplification can be deduced from the variation of the sensors' resistance values reported in Table 4-4. For a current supply between 0 and 30 mA, we observe a relative variation of the pillar device resistance of 11.5 % versus a variation of 1 % for the two other silicon devices. The relative resistance value variation, hence the Joule self-heating, is larger by one order of magnitude for the pillar device.

Table 4-4: Resistance variation with respect to the current supply

| Sensor | Resistance at room temperature (Ω) | Resistance variation range (Ω) |
|------------------|---|---|
| Pillar | 43.6 | 43.6 ~ 48.65 |
| Glass | 12.92 | 12.92 ~ 14.68 |
| Silicon membrane | 15.07 | 15.07 ~ 15.27 |
| Bulk silicon | 15.78 | 15.78 ~ 15.97 |

4.4.2 *Sensor's response to the velocity*

As previously mentioned, velocity can be estimated from the cooling magnitude of an anemometric flow-rate sensor. Therefore, we perform an experiment where we record the sensor's response within the velocity range from 0 m/s to 0.9 m/s (Figure 4-36). A constant current 30 mA is supplied to the sensor heater. Then, the temperature variation of the resistor due to the flowing fluid is measured. At each velocity value, thirty measurements are taken to reduce uncertainties. Results are shown for 30 mA supply current on Figure 4-36. We plot the sensor response to water velocity using the previously defined normalized temperature. We can see, as shown through numerical simulation, that the response of the pillar structure sensor is close to, and even better than, that of the glass sensor. Although the glass substrate flow-rate sensor exhibits highest Joule self-heating, the pillar flow-rate sensor shows a more linear response of the relative temperature variation as a function of velocity and it also covers a larger velocity range. In the case of the glass flow-rate sensors, the non-linear behavior can be ascribed to a back-flow phenomenon in the velocity range from 0.2 m/s to 0.4 m/s. On the other hand, bulk-silicon and membrane-based sensors show

inconsistent response in a significant part of to the considered velocity range. The recorded sensor responses to fluid velocity are consistent with Joule self-heating results. Here again, there could be an effect of back-flow in the case of the membrane-silicon device in the velocity range from 0.3 m/s to 1 m/s.

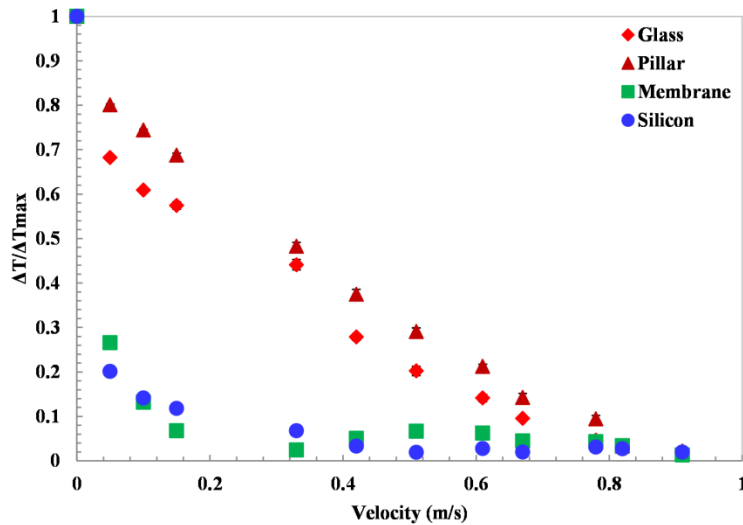


Figure 4-36: Glass, pillar, silicon membrane and bulk silicon flow-rate sensor measured response as a function of velocity at 30 mA current supply.

4.4.3 Comparison between numerical and experimental results

Both numerical (Figure 4-34) and experimental (Figure 4-36) sensors responses to fluid velocities show that bulk silicon and silicon membrane sensors' responses are similar and not satisfactory for a velocity range up to 1 m/s. On the other hand, an apparent inconsistency arises from the comparison of numerical and experimental results for glass and pillar devices. In the experimental plot (Figure 4-36), pillar flow-rate sensor shows better thermal response than glass. The opposite is observed on the numerical plot (Figure 4-34). However, a comparison in the same velocity range for both experimental and numerical results shows that the pillar device provides larger normalized temperature than glass device for large velocities. Indeed, we observe on Figure 4-37 that the pillar structure device generates larger normalized temperatures for velocities larger than 0.5 m/s. The remaining small difference between simulations and experimental results is very likely due to the approximated 2-D configuration used in the numerical study.

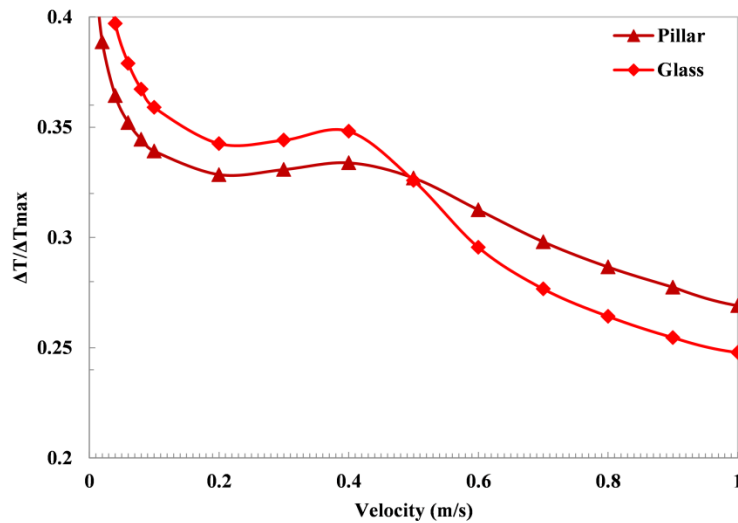


Figure 4-37: Numerically calculated response of the pillar and glass devices in the velocity range from 0 m/s to 1 m/s.

4.5 Conclusion

Several versions of a micro-machined thermal flow-rate sensor, as a part of a multi-parameter sensing chip (MPSC), have been presented and studied in this chapter. It is demonstrated that the thermal flow-rate sensor's performance largely depends on the thermal conductance of the substrate material, which has a great impact on the device sensitivity and power consumption. Low thermal conductance can be achieved even when using a high thermal conductivity material such as silicon, by a geometric design and optimization when the choice of the substrate material is constrained. In addition, the resistor dimensions are also a governing parameter of the sensor's response. We demonstrated the successful fabrication and optimization of a thermal flow-rate sensor on a silicon substrate, where silicon is absolutely required as the substrate material for the co-integration of other MEMS sensors. This was successfully achieved through micro-structuration of the silicon substrate using a pillar-like structure and reducing the substrate overall thermal conductance. Such micro-structuration leads to a silicon-based micro-machined thermal flow-rate sensor with performances comparable to state-of-the-art devices based on low conductivity materials such as glass.

5 Conclusion and Prospects

5.1 General conclusion

In this thesis, the process of design, fabrication, optimization and characterization of a miniature multi-parameter sensing module for monitoring water networks is reported. Different sensors which cover nine physical and chemical parameters relevant for water networks monitoring are integrated on a single chip. Successful co-integration enables the measurement of the desired parameters simultaneously. The final sensing module is fully autonomous and self-powered using an energy harvester for power supply. Data transmission electronics are also part of the module. The proposed device is not only designed for water quality monitoring but also for water flow rate measurement at different nodes of the network. This last parameter is of paramount importance for leakage detection and prevention and can also be used for resource demand monitoring.

Several versions of the device have been designed, fabricated and characterized before reaching the final operational prototype of the MPSC including all nine physical and chemical sensors. The different sensors of the MPSC have been separately tested in the lab and in the field. Obtained results validate target performances.

The electric conductivity sensor at ambient temperature was tested for different reference conductivity solutions. Since the sensor operates at AC current supply, appropriate supply intensity and frequency are required for an accurate response. The pressure sensor, made of piezoresistors under a polysilicon membrane, also shows a relevant response in the target measurement range, up to 6 bar. The output signal, hence the sensitivity of the device, can be tuned through the gain resistor variation which enables the device tuning for different measurement ranges. Among all physical sensors, the flow-rate sensor has been subject to the largest number of modifications before stabilization of the final prototype. Several versions have been developed: the first prototype targeted a separate operational flowrate sensor. It was made on a glass substrate. The second one addressed the constraint of co-integration with the pressure sensor which required the use of a silicon substrate. Such material increased power consumption and reduced the device sensitivity and turndown ratio. Consequently, several geometric and thermal optimization solutions have been implemented to ensure low power consumption, good sensitivity and turndown ratio while using silicon. Final optimization has been carried out by exploring transient mode operation of the device instead of commonly used steady state operation to reduce power consumption and measurement time. Finally, the temperature sensor was based on the same technology than the flowrate sensor. It required fewer

developments and optimization since no joule self-heating is required which loosens constraints on the substrate material choice and power consumption.

5.2 Perspectives of future developments of the MPSC

In the proposed MPSC, nine sensors have been co-integrated on a small foot-print. During test and validation phase, MEMS based physical sensors were run individually. This is a possible scenario in real operation conditions. However, simultaneous operation can also be targeted to increase sampling rate. In this case, cross-interactions between the different sensors cannot be excluded, especially when the sensor operation alters the observed medium properties. This is, for example, the case for the flowrate sensor which locally increases water temperature and can affect other parameters measurements.

For instance, it was shown in Chapter 3 how temperature affects water conductivity. As a consequence, the conductivity measurement should be executed under stable temperature. More generally, cross-interactions between the different sensors have not been investigated. Proper scenarios to investigate such possible interactions should be defined and systematically explored to ensure proper interpretation of measured signals in real operation conditions. The flowrate sensors generated heat can also affect temperature measurement. To avoid additional perturbations by the temperature sensor which is made of a platinum resistor, particular attention should be paid to this sensor power supply to avoid any additional Joule self-heating.

According to reported characterization tests, the stability of supply current is the main constraint that should be respected to guarantee a consistent response of the device. Since the device relies on an energy harvester for power supply, critical cases where harvested energy is not sufficient should be taken into account and addressed by implementing a secondary power source. In the present work, alternative operation schemes based on the device transient response have been briefly mentioned. Such alternative methods have a great potential for power consumption reduction and can be explored more in detail in future work.

Due to the target operation medium, water for instance, several electric precautions should be taken while performing experiments and measurements. Waterproofing is a critical constraint to prevent any damage to incorporated electronics. On the other hand, electrical connections between the sensor chip and the PCB is a second electric weak point that should be addressed carefully. The device mounting, packaging and waterproofing using protective glue should be performed meticulously. Long test campaigns should also be planned and executed to check waterproofing evolution with time. Long experimentation time can induce other problems such as biofouling. Indeed, in field test where water quality cannot be guaranteed, biological films deposition on the MPSC surface can occur. Such films would induce a shift in the device

response which is to be taken into account and corrected. Test scenarios to investigate the effect of such biofilms deposition should be considered in future works.

Finally, the presented multi-parameter sensing device has been initially developed as part of a sensors network to monitor water grids. However, the device can be used efficiently for a similar application in a more innovative way. Instead of fixing several MPSC at different nodes of the network, the MPSC can easily be turned into a portable device. Some typical features like compactness and wireless communication make such portability more realistic. Instead of large-scale rollout, the MPSC can be used as a mobile device to cover a wide area at lower cost. The device can be moved by an operator or embedded in a mobile robot (small boat, submarine, etc.) which carries the device through the medium of interest. Additional location data provided by an embedded GPS system would enable the mapping of a large area with a fine spatial mesh at very low cost. Such a solution can be very interesting for situations where high temporal sampling rate is not required.

1 Appendix for Chapter 2

1.1 Annex 1- Pressure sensor behavioral simulation

The behavior of the pressure sensors was evaluated beforehand through numerical simulations based on finite element modeling (FEM). These simulations include the first set of structural simulations so as to evaluate the strain field when the membrane is deflected by a uniform pressure. Then coupled simulations, including both structural and piezoresistive, led on one hand, to an appropriate choice for the membrane lateral dimensions and thickness and, on the other hand, to the optimum placing of the resistors and appropriate choice of their dimensions.

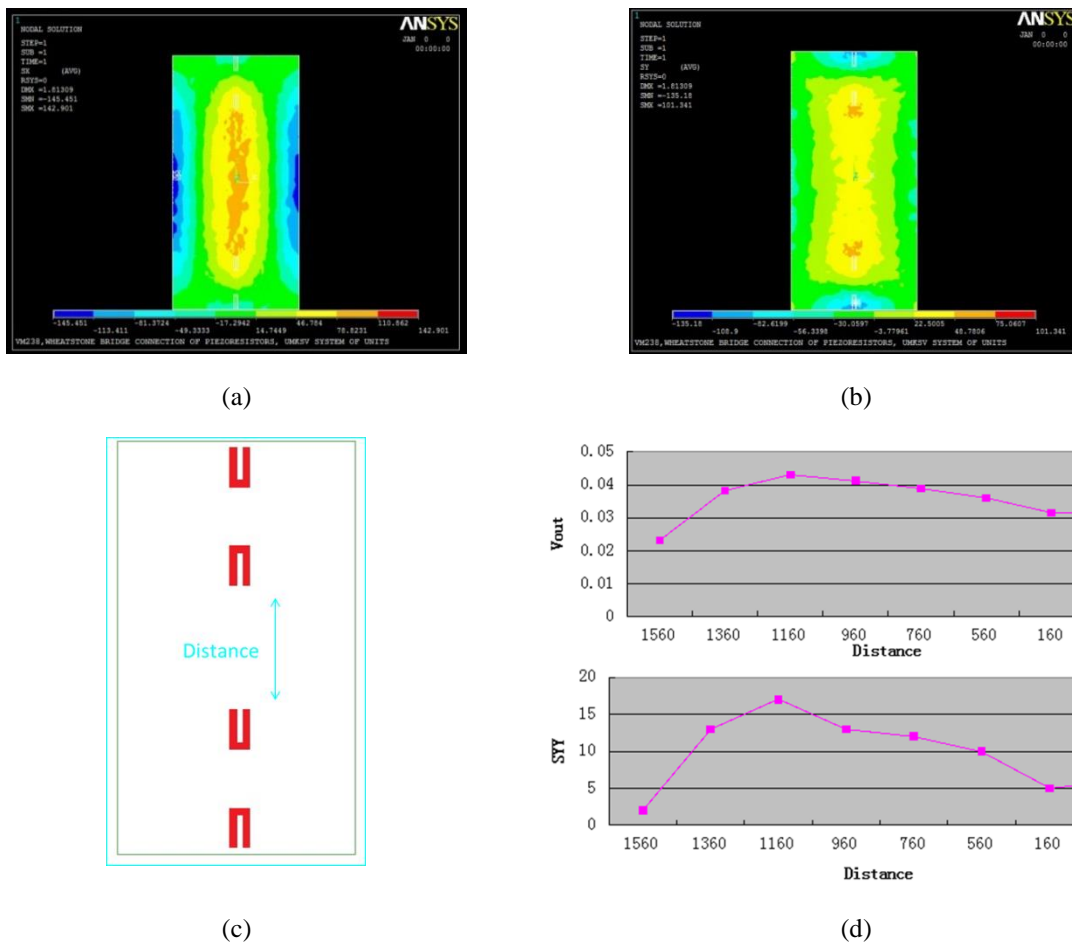


Figure Apn- 1: Example of FEM simulation results performed on the rectangular-shaped pressure sensor. The two upper contour plots show the distribution of the (a) S_{xx} and (b) S_{yy} stress components, (c) resistors distance on the membrane and (d) the lower right side curves show the effect of the position of the central resistances on the voltage at the output of the Wheatstone Bridge (dimensions are expressed herein micrometers).

Typical results of such simulations are shown in Figure Apn- 1. They relate to the rectangular-shaped pressure sensor. Those simulations show that the optimal position does not coincide with that of the maximum value of S_{yy} ; it is in this case slightly different, hence the interest of performing the above-mentioned coupled simulations.

1.2 Annex 2- Conductivity Sensor- Part A: Electrical Modelling

1.2.1 The electronic model of the sensor for numerical analysis

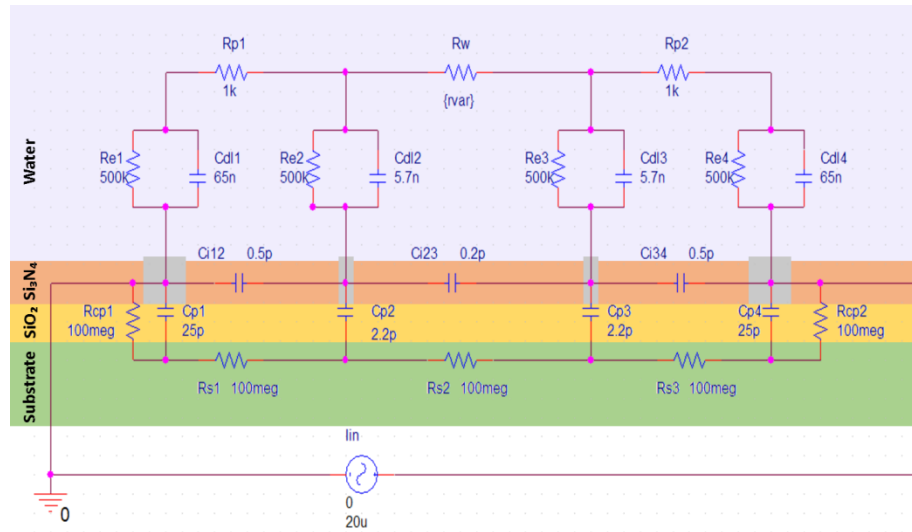


Figure Apn- 2: The electronic model of the water conductivity sensor. This model is a symbolic representation of electronic components that are formed by the substrate material, voltage and current electrodes and the surrounding water medium. The electronic model of the water conductivity sensor. This model is a symbolic representation of electronic components that are formed by the substrate material, voltage and current electrodes and the surrounding water medium.

Figure Apn- 2 represents the electronic model of the conductivity sensor. Here, R_w denotes the water resistance; R_{p1} and R_{p2} express the resistance of the small amount of water in between the voltage and current electrodes. The combined resistance and capacitance R_e and C_{dl} express the reaction resistance and electrochemical double layer capacitance of each electrode where the number 1, 2, 3 and 4 represent the electrodes number. The R_e resistance form due to the redox process which depends on the ion concentration in the solution. C_{i12} , C_{i23} and C_{i34} are the parasitic capacitance between the voltage and current electrodes. This parasitic capacitance formed between the water and isolation layer. Other parasitic capacitors are also formed in between the substrate and the electrodes, which are denoted by C_p and the numerical notation indicates the electrodes number. Therefore, their dielectric constant depends on the dielectric constant of the isolation material. The substrate resistances are denoted by R_{s1} , R_{s2} and R_{s3} respectively. This resistance value depends on the used substrate material. Besides the C_p and R_s , there are

two high-value resistances at the two ends of the model R_{cp1} and R_{cp2} . These two resistances are also parasitic resistance and they do not have any influence on the system. They are required for the simulation. The current source is not the part of this model; hence it is an external power source.

The numerical values of different parts of the model were determined by mathematical calculations and to some extent by assumption. The capacitors are calculated using the conventional formula stated below:

$$C = \epsilon \frac{A}{d} \quad \text{Eqn- 1}$$

Here, ϵ dielectric constant, A is the area and d is the distance between the electrodes. In order to calculate the mutual capacitance between the electrodes, the Eqn-2 is used, which is the formula of two parallel coplanar strip.

$$C_{CS} = \epsilon l \frac{K(\sqrt{1-x^2})}{K(x)} \quad \text{Eqn- 2}$$

Where, l is the length of the strips and $K(x)$ is the elliptical integral of x .

1.2.2 Frequency response

The frequency response analysis was performed in order to find out the effective operating frequency range, hence the linearity of the sensor. The same electronic model presented in Figure Apn- 2 was used for the analysis. In the simulation, the water resistance value R_w was varied from 500 Ω to 5 M Ω with a step of 1 k Ω . The result is presented here only for the sensor 3.

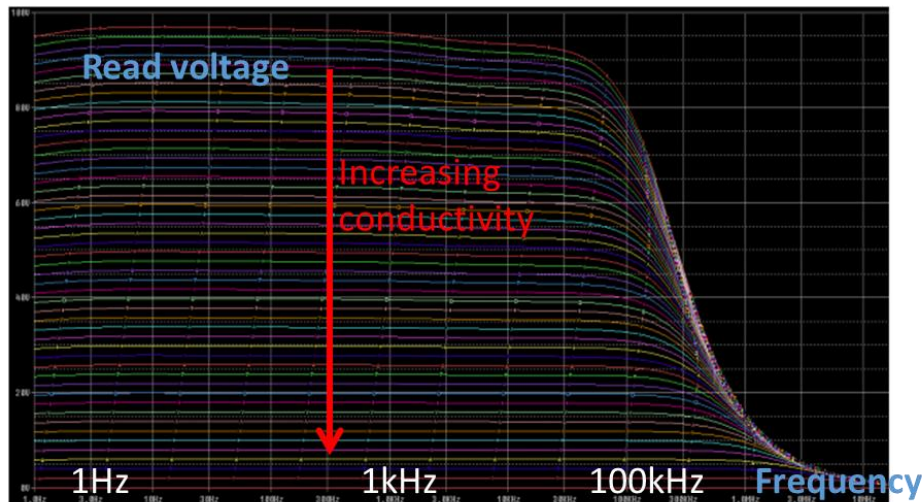


Figure Apn- 3: Frequency response of the sensor at different water resistance. Each plot trend represents a certain water resistance value.

The simulation was performed using PSpice. The flat region expresses the linear frequency range of the sensor, where it has to be operated.

1.3 Annex 3- Conductivity sensor- Part B: details of the experimental setup

1.3.1 Data acquisition

The data acquisition was performed using the NI USB-6259 DAQ board and LabView software interface. The used DAQ board can generate continuous power to the circuit and read the data from the desired point of the circuit. The different parameter of the supplied power can be controlled by LabView programme.

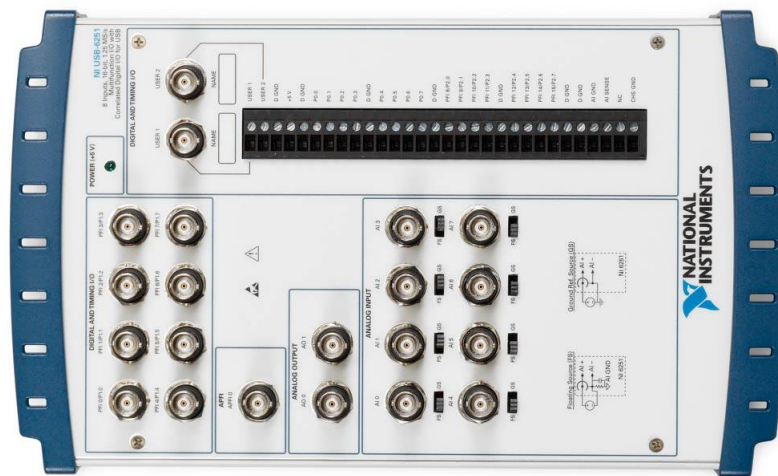


Figure Apn- 4: National Instruments multi-functional data acquisition board.

There are two kinds of the port on the DAQ board, where the one type is dedicated to input and the other for output. The input ports are for reading the data from the electronic circuit or from the sensor's reading port which is considered as an input to the DAQ board. On the other hand, the output ports are assigned to carry out the output or power from the DAQ board to the desired load. Both the output and input ports are programme controlled. LabView programme is used to visualize the input/output from the DAQ board. The programme that was used to characterize the conductivity sensor is provided below.

It can be observed from Figure Apn- 5 that, the programme window contains different graph plots with some controlling switches. Each part has its own functionality. The region marked with 'A' is the input-regulating part of the programme. In this part, the intensity of the input current can be regulated along with frequency and sampling rate of the current source. The unit under 'B' is to display the output of the sensor. The first graph plot displays the output before filtering and the middle one display after filtering. In the programme, there is a numerical filter in order to filter out the parasitic noise. The last plot under 'B' shows

the FFT peak. Indeed, the raw signals from the sensor pass through a spectral measurement process before filtering. The region 'C' is the linear regression unit, where the sensor's responses were measured with respect to the different conductivity level.

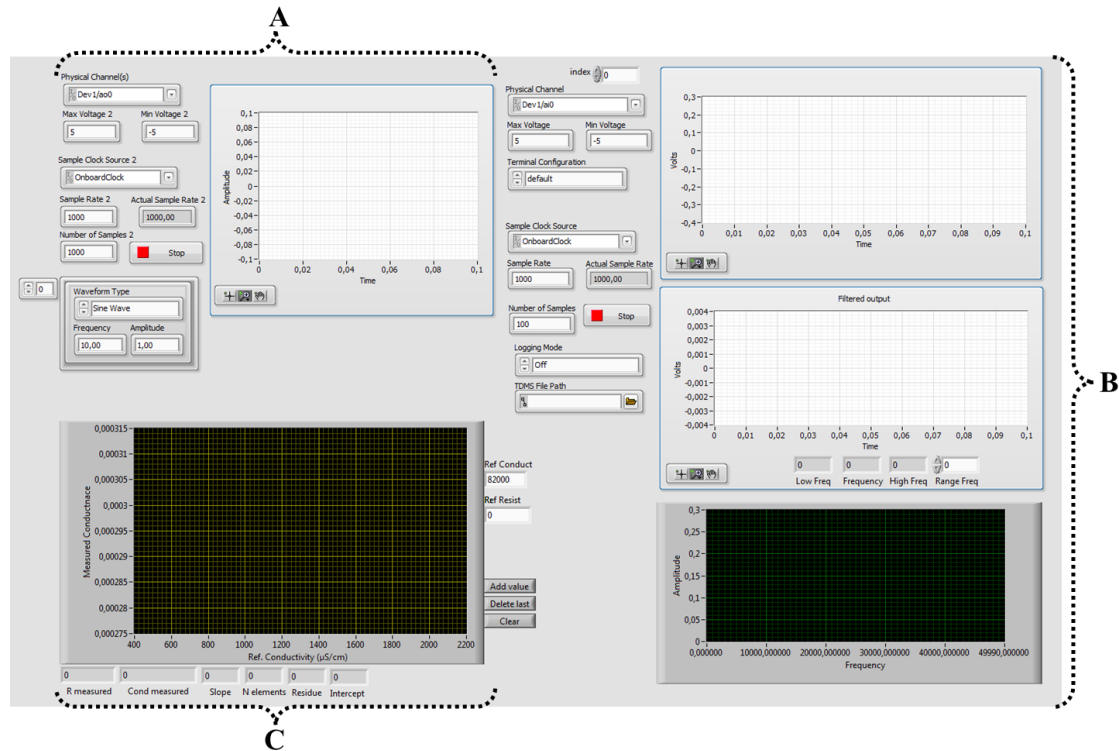


Figure Apn- 5: The LabView programme window for characterizing the conductivity sensor. The English alphabet A, B and C indicate input, output and linear regression part of the programme.

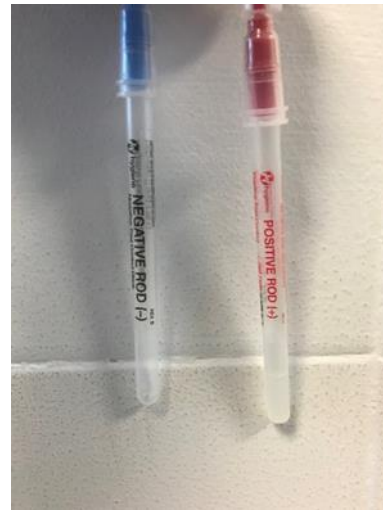
1.3.2 Tools used for Anti-fouling test:

Different tools were used in order to conduct the measurement of the biofilm growth on the surface of the considered sensor chips. The detail of those devices are provided below:

| | |
|-------------------------|--|
| Equipment: | Luminometer EnSURE from hygiena model V.2 Serial n° 068462 |
| Quality control: | Calibration Control Kit from hygiena Part No: PCD4000 Lot: 1214-30 |
| ATP swab: | UltraSnap ATP Surface Test from hygiena Cat. No: US2020 Lot: 01917 Expiration: 25may2018 |



(a)



(b)



(c)



(d)

Figure Apn- 6: Devices that have been used for conducting the measurement of the biofouling growth- (a) Luminometer EnSure, (b) calibration probes, (c) UltraSnap ATP Surface Test package and (d) ATP swab.

References

1. Brookes, P. C. The use of microbial parameters in monitoring soil pollution by heavy metals. *Biol. Fertil. Soils* **19**, 269–279 (1995).
2. Razo, I., Carrizales, L., Castro, J., Díaz-Barriga, F. & Monroy, M. Arsenic and Heavy Metal Pollution of Soil, Water and Sediments in a Semi-Arid Climate Mining Area in Mexico. *Water. Air. Soil Pollut.* **152**, 129–152 (2004).
3. Abraham, S. & Li, X. A Cost-effective Wireless Sensor Network System for Indoor Air Quality Monitoring Applications. *Procedia Comput. Sci.* **34**, 165–171 (2014).
4. Hromadka, J. *et al.* Multi-parameter measurements using optical fibre long period gratings for indoor air quality monitoring. *Sens. Actuators B Chem.* **244**, 217–225 (2017).
5. Kim, J.-J., Sung Kwon Jung & Jeong Tai Kim. Wireless Monitoring of Indoor Air Quality by a Sensor Network. *Indoor Built Environ.* **19**, 145–150 (2010).
6. O’Flynn, B. *et al.* SmartCoast: A Wireless Sensor Network for Water Quality Monitoring. in *32nd IEEE Conference on Local Computer Networks (LCN 2007)* 815–816 (2007). doi:10.1109/LCN.2007.34
7. Air pollution by ozone in Europe in summer 2001. *European Environment Agency* Available at: https://www.eea.europa.eu/publications/topic_report_2001_13/page001.html. (Accessed: 1st November 2017)
8. Davidson, C. Marine Notice : Carbon Dioxide : Health Hazard. *Aust. Marit. Saf. Auth.* (2003).
9. Rudge, J. & Gilchrist, R. Excess winter morbidity among older people at risk of cold homes: a population-based study in a London borough. *J. Public Health* **27**, 353–358 (2005).
10. Heatwave Plan for England 2013 Making the Case: the impact of heat on health – now and in the future - Heatwave_plan_2013_-_Making_the_case_Accessible_updated.pdf. Available at: https://www.gov.uk/government/uploads/system/uploads/attachment_data/file/201150/Heatwave_plan_2013_-_Making_the_case_Accessible_updated.pdf. (Accessed: 2nd November 2017)
11. Arundel, A. V., Sterling, E. M., Biggin, J. H. & Sterling, T. D. Indirect health effects of relative humidity in indoor environments. *Environ. Health Perspect.* **65**, 351–361 (1986).
12. Husman, T. Health effects of indoor-air microorganisms. *Scand. J. Work. Environ. Health* **22**, 5–13 (1996).

13. Yu, C. & Crump, D. A review of the emission of VOCs from polymeric materials used in buildings. *Build. Environ.* **33**, 357–374 (1998).
14. Liu, J.-H. *et al.* Developed urban air quality monitoring system based on wireless sensor networks. in *2011 Fifth International Conference on Sensing Technology* 549–554 (2011). doi:10.1109/ICSensT.2011.6137040
15. Postolache, O. A., Pereira, J. M. D. & Girao, P. M. B. S. Smart Sensors Network for Air Quality Monitoring Applications. *IEEE Trans. Instrum. Meas.* **58**, 3253–3262 (2009).
16. Kwon, J., Ahn, G., Kim, G., Kim, J. C. & Kim, H. A study on NDIR-based CO₂ sensor to apply remote air quality monitoring system. in *2009 ICCAS-SICE* 1683–1687 (2009).
17. Völgyesi, P., Nádas, A., Koutsoukos, X. & Lédeczi, Á. Air Quality Monitoring with SensorMap. in *2008 International Conference on Information Processing in Sensor Networks (ipsn 2008)* 529–530 (2008). doi:10.1109/IPSIN.2008.50
18. Ivanov, B., Zhelondz, O., Borodulkin, L. & Ruser, H. Distributed smart sensor system for indoor climate monitoring. 10–11 (2017).
19. Jiang, P., Xia, H., He, Z. & Wang, Z. Design of a Water Environment Monitoring System Based on Wireless Sensor Networks. *Sensors* **9**, 6411–6434 (2009).
20. Grayman, W. M., Deininger, R. A. & Males, R. M. *Design of Early Warning and Predictive Source-water Monitoring Systems*. (American Water Works Association, 2001).
21. Shaun, F. *et al.* Robust multi-parameter sensing probe for water monitoring based on ALD-coated metallic micro-patterns. in *2016 IEEE 11th Annual International Conference on Nano/Micro Engineered and Molecular Systems (NEMS)* 342–345 (2016). doi:10.1109/NEMS.2016.7758263
22. Storey, M. V., van der Gaag, B. & Burns, B. P. Advances in on-line drinking water quality monitoring and early warning systems. *Water Res.* **45**, 741–747 (2011).
23. Spectrometer Probes. Available at: <https://www.s-can.at/fr/produits/sondes-spectrales>. (Accessed: 24th July 2018)
24. OndaVia, Inc. | Definitive Results. Decisive Actions. Available at: <https://www.ondavia.com/>. (Accessed: 24th July 2018)
25. KAPTA™ 2000-AC2 In-line chlorine sensor | Veolia Water Technologies. Available at: http://technomaps.veoliawatertechnologies.com/kapta_2000/home/. (Accessed: 24th July 2018)
26. About. Available at: <http://www.censar.com/html/about.html>. (Accessed: 24th July 2018)

-
27. BioSentry™ MONITORING SYSTEM FOR WATERBORNE MICROORGANISMS. (2018).
 28. fluidion fluidic intelligence. Available at: <http://fluidion.com/en>. (Accessed: 24th July 2018)
 29. Water Optics Technology. Available at: <http://wot.com.sg/>. (Accessed: 24th July 2018)
 30. Winncy, Y. D. & Yelich, S. W. Resistive and Capacitive Based Sensing Technologies. *Int. Freq. Sens. Assoc. Publ.* **90**, 100–116 (2008).
 31. Kim, J., Kim, J., Shin, Y. & Yoon, Y. A study on the fabrication of an RTD (resistance temperature detector) by using Pt thin film. *Korean J. Chem. Eng.* **18**, 61–66 (2001).
 32. Mosser, V., Suski, J., Goss, J. & Obermeier, E. Piezoresistive pressure sensors based on polycrystalline silicon. *Sens. Actuators Phys.* **28**, 113–132 (1991).
 33. Eaton, W. P. & Smith, J. H. Micromachined pressure sensors: review and recent developments. *Smart Mater. Struct.* **6**, 530 (1997).
 34. Pramanik, C., Saha, H. & Gangopadhyay, U. Design optimization of a high performance silicon MEMS piezoresistive pressure sensor for biomedical applications. *J. Micromechanics Microengineering* **16**, 2060 (2006).
 35. Kingdom, B. What is non-revenue water? How can we reduce it for better water service? *The Water Blog* (2016). Available at: <http://blogs.worldbank.org/water/what-non-revenue-water-how-can-we-reduce-it-better-water-service>. (Accessed: 5th April 2018)
 36. Grundfoss, I. from. The advantages of water pressure management. *EE Publishers* (2015).
 37. Landeros, E., Pe´rez, R., Peralta, A. & Cembrano, G. Detection using pressure sensors and mathematical models Water Loss. (2009).
 38. Sanchez, J. C. Semiconductor strain gauge. (1963).
 39. Nave, R. Resistance and Resistivity. (1998). Available at: <http://hyperphysics.phy-astr.gsu.edu/hbase/electric/resis.html#c1>. (Accessed: 26th March 2018)
 40. YSI Model 3200 Conductance, Resistance, Salinity, Total Dissolved Solids and Temperature Instrument. (1999).
 41. Monitoring and Assessing Water Quality - Volunteer Monitoring | Monitoring & Assessment | US EPA. Available at: <https://archive.epa.gov/water/archive/web/html/index-18.html>. (Accessed: 18th March 2018)

42. Miller, R. L., Bradford, W. L. & Peters, N. E. *Specific conductance; theoretical considerations and application to analytical quality control*. (U.S. G.P.O., 1988).
43. Electrical Conductivity, USGS Water Science School. Available at: <https://water.usgs.gov/edu/electrical-conductivity.html>. (Accessed: 26th March 2018)
44. Light, T. S., Licht, S., Bevilacqua, A. C. & Morash, K. R. The Fundamental Conductivity and Resistivity of Water. *Electrochem. Solid-State Lett.* **8**, E16–E19 (2005).
45. Wetzel, R. G. *Limnology: Lake and River Ecosystems*. (Gulf Professional Publishing, 2001).
46. Properties of seawater. Available at: http://sam.ucsd.edu/sio210/lect_2/lecture_2.html. (Accessed: 26th March 2018)
47. Eaton, A. D. *et al.* *Standard methods for the examination of water and wastewater*. (American Public Health Association, 1998).
48. SWRCB. (2002). Electrical Conductivity/Salinity Fact Sheet . In The Clean Water Team Guidance Compendium for Watershed Monitoring and Assessment State Water Resources Control Board. Retrieved from http://www.swrcb.ca.gov/water_issues/programs/swamp/docs/cwt/guidance/3130en.pdf. (2002).
49. Water quality indicators. Available at: <https://www.lcra.org/water/quality/colorado-river-watch-network/Pages/water-quality-indicators.aspx>. (Accessed: 26th March 2018)
50. Pumera, M. Contactless conductivity detection for microfluidics: Designs and applications. *Talanta* **74**, 358–364 (2007).
51. Huck, C. *et al.* Capacitively coupled electrolyte-conductivity sensor based on high-k material of barium strontium titanate. *Sens. Actuators B Chem.* **198**, 102–109 (2014).
52. Martinez, I. Thermometry. (1995).
53. Solar Radiation at Earth - Windows to the Universe. Available at: https://www.windows2universe.org/earth/climate/sun_radiation_at_earth.html. (Accessed: 18th March 2018)
54. US Department of Commerce, N. O. and A. A. How far does light travel in the ocean? Available at: https://oceanservice.noaa.gov/facts/light_travel.html. (Accessed: 18th March 2018)
55. Temperature - Water Properties, USGS Water Science School. Available at: <https://water.usgs.gov/edu/temperature.html>. (Accessed: 18th March 2018)

-
56. Thermal pollution - The Encyclopedia of Earth. Available at: https://editors.eol.org/eoearth/wiki/Thermal_pollution. (Accessed: 18th March 2018)
57. Definition of VISCOSITY. Available at: <https://www.merriam-webster.com/dictionary/viscosity>. (Accessed: 19th March 2018)
58. Hayashi, M. Temperature-electrical conductivity relation of water for environmental monitoring and geophysical data inversion. *Environ. Monit. Assess.* **96**, 119–128 (2004).
59. Temperature Effects on Solubility. Available at: <http://galileo.phys.virginia.edu/education/outreach/8thgradesol/TempSolubility.htm>. (Accessed: 19th March 2018)
60. Poonam Bhadja and Ashokkumar Vaghela. Effect of temperature on the toxicity of some metals to *Labeo bata* (Hamilton, 1822). *Int. J. Adv. Life Sci.* **Volume-6**, 252–254 (2013).
61. Ammonia Toxicity and pH Changes. Available at: <http://www2.ca.uky.edu/wkrec/pH-Ammonia.htm>. (Accessed: 19th March 2018)
62. Final Aquatic Life Ambient Water Quality Criteria For Ammonia-Freshwater 2013. *Federal Register* (2013). Available at: <https://www.federalregister.gov/documents/2013/08/22/2013-20307/final-aquatic-life-ambient-water-quality-criteria-for-ammonia-freshwater-2013>. (Accessed: 19th March 2018)
63. Measuring ORP on YSI 6-Series Sondes: Tips, Cautions and Limitations. (2005).
64. Water Density (water properties), USGS Water Science School. Available at: <https://water.usgs.gov/edu/density.html>. (Accessed: 19th March 2018)
65. LabBench Activity Key Concepts II: Temperature and Metabolic Activity. *Pearson* Available at: http://www.phschool.com/science/biology_place/labbench/lab10/concepts2.html.
66. Di Santo, V. & Bennett, W. A. Effect of rapid temperature change on resting routine metabolic rates of two benthic elasmobranchs. *Fish Physiol. Biochem.* **37**, 929–934 (2011).
67. Rusby, R. *The Beginner's Guide to Temperature Measurement*. (National Physical Laboratory, 2012).
68. Kelvin. *Wikipedia* (2018).
69. Fahrenheit. *Wikipedia* (2018).
70. Quinn, T. J. & Compton, J. P. The foundations of thermometry. *IOPscience* **38**, 151–239 (1975).

-
71. Greek Medicine: THE FOUR BASIC QUALITIES - Yin and Yang, Greek Style. Available at: http://www.greekmedicine.net/b_p/Four_basic_qualities.html. (Accessed: 24th August 2018)
72. Galen. *Wikipedia* (2018).
73. Thermometer. *Wikipedia* (2018).
74. Childs, P. R. N., Greenwood, J. R. & Long, C. A. Review of temperature measurement. *Rev. Sci. Instrum.* **71**, 2959–2978 (2000).
75. Kaanta, B. C. *et al.* High Sensitivity Micro-Thermal Conductivity Detector for Gas Chromatography. in *2009 IEEE 22nd International Conference on Micro Electro Mechanical Systems* 264–267 (2009). doi:10.1109/MEMSYS.2009.4805369
76. Hsiai, T. K. *et al.* Micro Sensors: Linking Real-Time Oscillatory Shear Stress with Vascular Inflammatory Responses. *Ann. Biomed. Eng.* **32**, 189–201 (2004).
77. Maily, F. *et al.* Anemometer with hot platinum thin film. *Sens. Actuators Phys.* **94**, 32–38 (2001).
78. Nguyen, N. T. Micromachined flow sensors—a review. *Flow Meas. Instrum.* **8**, 7–16 (1997).
79. Honschoten, J. van *et al.* Application of a microflow as a low-cost level sensor. *J. Micromechanics Microengineering* **10**, 250 (2000).
80. Dittmann, D., Ahrens, R., Rummler, Z., Schlote-Holubek, K. & Schomburg, W. K. Low-Cost Flow Transducer Fabricated with the Amanda-Process. in *Transducers '01 Eurosensors XV* 1444–1447 (Springer, Berlin, Heidelberg, 2001). doi:10.1007/978-3-642-59497-7_341
81. Kreider, K. G. & DiMeo, F. Platinum/palladium thin-film thermocouples for temperature measurements on silicon wafers. *Sens. Actuators Phys.* **69**, 46–52 (1998).
82. Kuo, J. T. W., Yu, L. & Meng, E. Micromachined Thermal Flow Sensors—A Review. *Micromachines* **3**, 550–573 (2012).
83. Meng, E. F.-C. MEMS technology and devices for a micro fluid dosing system. (California Institute of Technology, 2003).
84. PEETERS, F., PEETERMANS, M. & INDESTEEGE, L. Temperature Sensors. in *Modern Sensor Handbook* 347–391 (ISTE Ltd, 2007).
85. J. Stephenson, R. *et al.* Mechanical Variables Measurement - Thermal. in *Measurement, Instrumentation and Handbook* (CRC Press LLC).
86. White, D. R. *et al.* The status of Johnson noise thermometry. *Metrologia* **33**, 325 (1996).

87. Johnson, J. B. Thermal Agitation of Electricity in Conductors. *Phys. Rev.* **32**, 97–109 (1928).
88. Nyquist, H. Thermal Agitation of Electric Charge in Conductors. *Phys. Rev.* **32**, 110–113 (1928).
89. Qian, Y. *et al.* Application of RTD Sensor in the Real Time Measurement and Wireless Transmission. in *2014 Fourth International Conference on Instrumentation and Measurement, Computer, Communication and Control* 658–662 (2014). doi:10.1109/IMCCC.2014.140
90. Bhatta, R. P. *et al.* High temperature thermal conductivity of platinum microwire by 3ω method. *Rev. Sci. Instrum.* **81**, 114904 (2010).
91. Thermal conductivity detector (TCD). *HiQ* Available at: http://hiq.linde-gas.com/en/analytical_methods/gas_chromatography/thermal_conductivity_detector.html. (Accessed: 7th March 2018)
92. Lussac, E., Barattin, R., Cardinael, P. & Agasse, V. Review on Micro-Gas Analyzer Systems: Feasibility, Separations and Applications. *Crit. Rev. Anal. Chem.* **46**, 455–468 (2016).
93. Chen, K. & Wu, Y.-E. Thermal analysis and simulation of the microchannel flow in miniature thermal conductivity detectors. *Sens. Actuators Phys.* **79**, 211–218 (2000).
94. Alfino, N., Amidei, M. & Alomairah, A. Types of Flowmeters.
95. A Brief History of Flow Measurement and Prospect-Chongqing Risen Science and Technology development Co., Ltd. Available at: <http://www.zydc.com/en/showkfzx.asp?lm=469&ID=28>. (Accessed: 26th December 2017)
96. Cottrell, M. Fluid Flow Instrumentation. (2007).
97. Michael Faraday, In Our Time - BBC Radio 4. *BBC* Available at: <https://www.bbc.co.uk/programmes/b06s9rz9>. (Accessed: 21st June 2018)
98. Fujita, H. A decade of MEMS and its future. in , *Tenth Annual International Workshop on Micro Electro Mechanical Systems, 1997. MEMS '97, Proceedings, IEEE* 1–7 (1997). doi:10.1109/MEMSYS.1997.581729
99. Kuo, J. T. W., Chang, L.-Y., Li, P.-Y., Hoang, T. & Meng, E. A microfluidic platform with integrated flow sensing for focal chemical stimulation of cells and tissue. *Sens. Actuators B Chem.* **152**, 267–276 (2011).
100. Billat, S. *et al.* Monolithic integration of micro-channel on disposable flow sensors for medical applications. *Sens. Actuators Phys.* **145**, 66–74 (2008).

101. Silvestri, S. & Schena, E. Micromachined Flow Sensors in Biomedical Applications. *Micromachines* **3**, 225–243 (2012).
102. Soundararajan, G. *et al.* MEMS shear stress sensors for microcirculation. *Sens. Actuators Phys.* **118**, 25–32 (2005).
103. Kaanta, B. C., Chen, H. & Zhang, X. Novel device for calibration-free flow rate measurements in micro gas chromatographic systems. *J. Micromechanics Microengineering* **20**, 095034 (2010).
104. Zampolli, S. *et al.* Selectivity enhancement of metal oxide gas sensors using a micromachined gas chromatographic column. *Sens. Actuators B Chem.* **105**, 400–406 (2005).
105. Bartlett, K. H., Martinez, M. & Bert, J. Modeling of Occupant-Generated CO₂ Dynamics in Naturally Ventilated Classrooms. *J. Occup. Environ. Hyg.* **1**, 139–148 (2004).
106. Zhu, Y., Chen, B., Qin, M. & Huang, Q. A. 2-D Micromachined Thermal Wind Sensors #x2014;A Review. *IEEE Internet Things J.* **1**, 216–232 (2014).
107. Shen, G.-P., Qin, M., Huang, Q.-A., Zhang, H. & Wu, J. A FCOB packaged thermal wind sensor with compensation. *Microsyst. Technol.* **16**, 511–518 (2010).
108. Bruschi, P. & Piotta, M. Design Issues for Low Power Integrated Thermal Flow Sensors with Ultra-Wide Dynamic Range and Low Insertion Loss. *Micromachines* **3**, 295–314 (2012).
109. Dijkstra, M. *et al.* Miniaturized thermal flow sensor with planar-integrated sensor structures on semicircular surface channels. *Sens. Actuators Phys.* **143**, 1–6 (2008).
110. Wu, S., Lin, Q., Yuen, Y. & Tai, Y.-C. MEMS flow sensors for nano-fluidic applications. *Sens. Actuators Phys.* **89**, 152–158 (2001).
111. Chen Jack, Fan Zhifang, Zou Jun, Engel Jonathan & Liu Chang. Two-Dimensional Micromachined Flow Sensor Array for Fluid Mechanics Studies. *J. Aerosp. Eng.* **16**, 85–97 (2003).
112. Nguyen, N. T. & Dötzel, W. Asymmetrical locations of heaters and sensors relative to each other using heater arrays: a novel method for designing multi-range electrocaloric mass-flow sensors. *Sens. Actuators Phys.* **62**, 506–512 (1997).
113. Li, C., Wu, P.-M., Han, J. & Ahn, C. H. A flexible polymer tube lab-chip integrated with microsensors for smart microcatheter. *Biomed. Microdevices* **10**, 671–679 (2008).
114. Ernst, H., Jachimowicz, A. & Urban, G. A. High resolution flow characterization in Bio-MEMS. *Sens. Actuators Phys.* **100**, 54–62 (2002).

-
115. Cubukcu, A. S., Zernickel, E., Buerklin, U. & Urban, G. A. A 2D thermal flow sensor with sub-mW power consumption. *Sens. Actuators Phys.* **163**, 449–456 (2010).
116. Kohl, F. *et al.* A micromachined flow sensor for liquid and gaseous fluids. *Sens. Actuators Phys.* **41**, 293–299 (1994).
117. Nguyen, N.-T., Meng, A. H., Black, J. & White, R. M. Integrated flow sensor for in situ measurement and control of acoustic streaming in flexural plate wave micropumps. *Sens. Actuators Phys.* **79**, 115–121 (2000).
118. Talic, A. *et al.* MEMS Flow Sensors Based on Self-Heated aGe-Thermistors in a Wheatstone Bridge. *Sensors* **15**, 10004–10025 (2015).
119. Berthet, H., Jundt, J., Durivault, J., Mercier, B. & Angelescu, D. Time-of-flight thermal flowrate sensor for lab-on-chip applications. *Lab. Chip* **11**, 215–223 (2011).
120. Tan, Z. *et al.* Characteristics of on-wall in-tube flexible thermal flow sensor under radially asymmetric flow condition. *Sens. Actuators Phys.* **138**, 87–96 (2007).
121. Tan, Z. *et al.* Experimental and theoretical study of an on-wall in-tube flexible thermal sensor. *J. Micromechanics Microengineering* **17**, 679 (2007).
122. Shin, W. C. & Besser, R. S. A micromachined thin-film gas flow sensor for microchemical reactors. *J. Micromechanics Microengineering* **16**, 731 (2006).
123. Alfadhel, A., Li, B., Zaher, A., Yassine, O. & Kosel, J. A magnetic nanocomposite for biomimetic flow sensing. *Lab. Chip* **14**, 4362–4369 (2014).
124. Chang, L.-Y., Li, P.-Y., Zhao, L., Hoang, T. & Meng, E. Integrated flow sensing for focal biochemical stimulation. in *2008 3rd IEEE International Conference on Nano/Micro Engineered and Molecular Systems* 921–926 (2008). doi:10.1109/NEMS.2008.4484473
125. Lee, C. Y. *et al.* A Smart Flow Sensor for Flow Direction Measurement. *Adv. Mater. Res.* **47–50**, 189–192 (2008).
126. King, L. V. On the convection of heat from small cylinders in a stream of fluid: Determination of the convection constants of small platinum wires, with applications to hot-wire anemometry. *Proc R Soc Lond A* **90**, 563–570 (1914).
127. Chiu, N.-F., Hsiao, T.-C. & Lin, C.-W. Low power consumption design of micro-machined thermal sensor for portable spirometer. *Tamkang J. Sci. Eng.* **8**, 225–230 (2005).

128. Buchner, R., Sosna, C., Maiwald, M., Benecke, W. & Lang, W. A high-temperature thermopile fabrication process for thermal flow sensors. *Sens. Actuators Phys.* **130–131**, 262–266 (2006).
129. Cho, S., Joshi, Y., Sundaram, V., Sato, Y. & Tummala, R. Comparison of thermal performance between glass and silicon interposers. in *2013 IEEE 63rd Electronic Components and Technology Conference* 1480–1487 (2013). doi:10.1109/ECTC.2013.6575767
130. Shaun, F. J., Nefzaoui, E., Marty, F., Cesar, W. & Bourouina, T. Micro-fabricated thermal flow-rate sensors: the substrate material impact on the device performance and power consumption. *J. Microsyst. Technol.*

List of publications

Conferences:

1. **Shaun F** et al. T 2016 “Robust Multi-Parameter Sensing Probe for Water Monitoring Based on ALD-Coated Metallic Micro-patterns” Nano/Micro Engineered and Molecular Systems (NEMS), 2016 IEEE 11th Annual International Conference
2. **Shaun F** et al. 2017 “On the Co-Integration of a Thermo-resistive Flow Rate Sensor in a Multi-Parameter Sensing Chip for Water Network Monitoring” Solid-State Sensors, Actuators and Microsystems (TRANSDUCERS), 2017 19th International Conference
3. **Shaun F** et al. 2017 “Design of micro-fabricated thermal 26 flow-rate sensor for water network monitoring” 2017 Symposium on Design, Test, Integration and Packaging of 27 MEMS/MOEMS (DTIP) 2017 Symposium on Design, Test, Integration and Packaging of MEMS/MOEMS 28 (DTIP) pp 1–4
4. **Shaun F** et al. 2018 “Energy efficient micro-machined thermal flow-rate sensor based on transient operation mode” 2018 Symposium on Design, Test, Integration and Packaging of MEMS/MOEMS (DTIP), 2018 Symposium

Journals:

1. **Shaun F**, Nefzaoui F, Marty F, Cesar W and Bourouina T “Micro-fabricated thermal flow-rate sensors for water networks monitoring: the impact of the substrate material on the device performance and power consumption,” J. of Microsys. Technol. (2018) <https://doi.org/10.1007/s00542-018-4098-5>
2. **Shaun F**, Sarkar S, Marty F, Poulichet P, Cesar W, Nefzaoui E and Bourouina T “Sensitivity optimization of micro-machined thermo-resistive flow-rate sensors on silicon substrates,” J. Micromechanics Microengineering, vol. 28, no. 7, p. 074002, 2018.
3. **Shaun F** et al. “Carbon Nanotubes Meet MEMS: Co-integration Enables 9 Physical and Chemical Sensors on a Single Chip’s IoT Node for Water Network Monitoring” in preparation, to be submitted to *Microsystem & Nanoengineering*

Abstract

Water is a vital element for every living being on the earth. Like many other dwindling natural resources, clean water faces a strong pressure because of human activity and the rapid growth of global population. The situation is so critical that clean water has been identified as one of the seventeenth sustainable development goals of the United Nations. Under these conditions, a sustainable management of water resources is necessary. For this purpose, a smart solution for water networks monitoring can be very helpful. However, commercially available solutions lack compactness, self-powering capabilities cost competitiveness, necessary to enable the large rollout over water networks.

The present thesis takes place in the framework of a European research project, PROTEUS, which addresses these different problems by designing and fabricating a multi-parameter sensor chip (MPSC) for water resources monitoring. The MPSC enables the measurement of 9 physical and chemical parameters, is reconfigurable and self-powered. The present thesis addresses more precisely physical sensors, their design, optimization and co-integration on the MPSC. The developed device exhibits state of the art or larger performances with regard to its redundancy, turn-down ratio and power consumption.

The present manuscript is split into two main parts: Part-I and Part-II. Part-I deals with non-thermal aspects of the MPSC, the pressure and conductivity sensor for instance, as well as the fabrication process of the whole device (Chapter 1 and 2). The background of environmental monitoring is presented in Chapter 1 along with the State of Art review. Chapter 2 describes fabrication methods of the MPSC. Preliminary characterization results of non-thermal sensors are also reported in this chapter. Chapter 3 and 4, included in Part-II, deal with thermal sensors (temperature and flow-rate). Chapter 3 describes the many possible uses of electric resistances for sensing applications. Finally, in chapter four, we focus on flowrate sensors before concluding and making a few suggestions for future works.

Résumé

L'eau est une ressource vitale, indispensable à la vie sur terre. A l'instar de nombreuses autres ressources naturelles, l'eau propre à la consommation est soumise à une forte pression à cause de l'impact de l'activité humaine d'une part et de l'augmentation continue de la population mondiale d'autre part. Une pression tellement forte que l'eau propre représente l'un des 17 objectifs de développement durable des Nations Unies. Dans ce contexte, une gestion rationnelle et durable de la ressource s'avère indispensable. Dans ce but, un système intelligent de supervision des réseaux d'eau potable peut s'avérer très utile. Les systèmes existants sont toutefois peu intégrés et compacts, nécessitent souvent une alimentation externe, et restent relativement chers pour un déploiement massif sur les réseaux.

La présente thèse s'inscrit dans le cadre d'un projet de recherche européen, PROTEUS, visant à pallier ces différents problèmes en mettant au point un système de mesure pour la supervision de la ressource en eau permettant la mesure de 9 paramètres physico-chimiques, reconfigurable, et énergétiquement autonome. La contribution de la présente thèse à ce projet porte sur la conception et l'optimisation des différents capteurs physiques (conductivité électrique, pression, température et débit) ainsi qu'à leur co-intégration sur une même puce. Le système proposé montre des performances au moins égales à celle de l'état de l'art en ce qui concerne la robustesse, assurée par la redondance de nombreux éléments sensibles, le domaine de sensibilité et la consommation énergétique.

Le présent manuscrit est par conséquent construit comme suit : le premier chapitre est une introduction générale à la supervision de grandeurs environnementales et à la puce multi-capteurs. Le second chapitre décrit la structure de la puce multi-capteurs ainsi que les méthodes de fabrication utilisées, avec une attention particulière accordée aux capteurs de pression et de conductivité électrique. Le troisième chapitre porte sur l'utilisation de résistances électriques pour la mesure de diverses grandeurs physiques, notamment la température. Le dernier chapitre s'attarde plus particulièrement sur l'utilisation de ce type de résistances pour la mesure de débit avant de conclure et de proposer des perspectives pour des travaux futurs.